

**COMPUTATIONAL FLUID DYNAMICS (CFD) MODELING
OF INTERFACIAL MOMENTUM TRANSFER IN BUBBLY
TWO-PHASE FLOW**

**BALONCUKLU İKİ FAZLI AKIŞLARDA, FAZLAR ARASI
MOMENTUM TRANSFERİNİN HESAPLAMALI
AKIŞKANLAR DİNAMİĞİ (HAD) İLE MODELLENMESİ**

İZZET ÖZGÜN GÜLER

PROF. DR. CEMİL KOCAR

Supervisor

Submitted to

Graduate School of Science and Engineering of Hacettepe University

as a Partial Fulfillment to the Requirements

for the Award of the Degree of Doctor of Philosophy (PhD)

in Nuclear Engineering

July 2024

ETHICS

In this thesis study, prepared in accordance with the spelling rules of Institute of Graduate Studies in Science of Hacettepe University,

I declare that

- all the information and documents have been obtained in the base of the academic rules.
- all audio-visual and written information and results have been presented according to the rules of scientific ethics
- in case of using others works, related studies have been cited in accordance with the scientific standards
- all cited studies have been fully referenced
- I did not do any distortion in the data set
- and any part of this thesis has not been presented as another thesis study at this or any other university.

19 / 07 / 2024

İzzet Özgün Güler

YAYINLAMA FİKRİ MÜLKİYET HAKLARI BEYANI

Enstitü tarafından onaylanan lisansüstü tezimin tamamını veya herhangi bir kısmını, basılı (kağıt) ve elektronik formatta arşivleme ve aşağıda verilen koşullarla kullanıma açma iznini Hacettepe üniversitesine verdiğimi bildiririm. Bu izinle Üniversiteye verilen kullanım hakları dışındaki tüm fikri mülkiyet haklarım bende kalacak, tezimin tamamının ya da bir bölümünün gelecekteki çalışmalarda (makale, kitap, lisans ve patent vb.) kullanım hakları bana ait olacaktır.

Tezin kendi orijinal çalışmam olduğunu, başkalarının haklarını ihlal etmediğimi ve tezimin tek yetkili sahibi olduğumu beyan ve taahhüt ederim. Tezimde yer alan telif hakkı bulunan ve sahiplerinden yazılı izin alınarak kullanması zorunlu metinlerin yazılı izin alarak kullandığımı ve istenildiğinde suretlerini Üniversiteye teslim etmeyi taahhüt ederim.

Yükseköğretim Kurulu tarafından yayınlanan **“Lisansüstü Tezlerin Elektronik Ortamda Toplanması, Düzenlenmesi ve Erişime Açılmasına İlişkin Yönerge”** kapsamında tezim aşağıda belirtilen koşullar haricince YÖK Ulusal Tez Merkezi / H. Ü. Kütüphaneleri Açık Erişim Sisteminde erişime açılır.

- Enstitü yönetim kurulu kararı ile tezimin erişime açılması mezuniyet tarihimden itibaren 2 yıl ertelenmiştir.
- Enstitü yönetim kurulu gerekçeli kararı ile tezimin erişime açılması mezuniyet tarihimden itibaren ay ertelenmiştir.
- Tezim ile ilgili gizlilik kararı verilmiştir.

19 / 07 / 2024

İzzet Özgün Güler

ABSTRACT

COMPUTATIONAL FLUID DYNAMICS (CFD) MODELING OF INTERFACIAL MOMENTUM TRANSFER IN BUBBLY TWO-PHASE FLOW

İzzet Özgün Güler

Doctor of Philosophy (PhD) , Nuclear Engineering

Supervisor: Prof. Dr. Cemil Kocar

July 2024, 138 pages

This dissertation addresses critical gaps in Computational Fluid Dynamics (CFD) modeling of momentum transfer in two-phase flow systems. Available models, based on empirical relations from the behavior of single bubbles in the Stokes regime, fail to capture the complex dynamics of bubbly flows involving multiple interacting bubbles. This research develops more accurate models by considering factors such as void fraction, shear, wake effects, and turbulence.

The study begins with a literature review that highlights discrepancies between standard modeling practices and the complexities of two-phase dynamics. It continues with CFD simulations employing preferred closure models for drag, lift, and other forces, benchmarked against experimental data to evaluate their accuracy and limitations. Insights from these comparisons inform a design exploration procedure that defines functional forms for drag and lift coefficient models with undetermined constants. An automated optimization process minimizes discrepancies between CFD analysis and experimental observations across

various cases.

The dissertation concludes by comparing available models with the newly developed ones, demonstrating the latter's performance in predicting two-phase flow dynamics. This research contributes a methodologically robust and theoretically sound framework for advancing CFD modeling, impacting both academic research and industrial applications.

Keywords: multiphase flow, two-phase flow, bubbly flow, CFD modeling, interphase momentum exchange, momentum closure relations

ÖZET

BALONCUKLU İKİ FAZLI AKIŞLARDA, FAZLAR ARASI MOMENTUM TRANSFERİNİN HESAPLAMALI AKIŞKANLAR DİNAMİĞİ (HAD) İLE MODELLENMESİ

İzzet Özgün Güler

Doktora, Nükleer Enerji Mühendisliği

Danışman: Prof. Dr. Cemil Kocar

Temmuz 2024, 138 sayfa

Bu tez, Hesaplamalı Akışkanlar Dinamiği (HAD) modellemesindeki kritik boşlukları ele almakta ve özellikle iki fazlı akış sistemlerinde momentum transferi mekanizmalarına odaklanmaktadır. Mevcut modeller, genellikle Stokes rejimindeki tekil baloncukların davranışına dayanan ampirik ilişkilerden türetilmiş arayüz kapatma modellerine dayanır. Ancak, birden fazla etkileşen baloncuğu içeren baloncuklu akışların karmaşık dinamiklerini bu modeller yetersiz bir şekilde temsil eder. Bu araştırma, hacim oranı, kayma, iz etkileri ve türbülans gibi kritik faktörleri dikkate alarak daha doğru modeller geliştirmeyi amaçlamaktadır.

Çalışma, CFD simülasyonları için kapatma modeli seçimindeki trendleri ve dikey borularda baloncuklu akış üzerine yapılan deneysel araştırmaları inceleyerek başlar. Standart modelleme yaklaşımları ile iki fazlı akış dinamikleri arasında uyumsuzluk olduğu tespit edilmiştir. Ardından, sürüklenme, kaldırma ve diğer kuvvetler için tercih edilen kapatma modelleri kullanılarak gerçekleştirilen CFD simülasyonları, kapsamlı deneysel verilerle

karşılaştırılarak değerlendirilir. Bu karşılaştırmalar, sürüklenme ve kaldırma katsayılarının modelleri için fonksiyonel bir form ve belirsiz sabitler tanımlayan bir tasarım keşif prosedürü geliştirilmesine rehberlik eder.

Araştırma, geliştirilen yeni modellerin mevcut modellerle karşılaştırmasını içerir ve bu modellerin iki fazlı akış dinamiklerini tahmin etmedeki performansını gösterir. Bu tez, akademik araştırma ve endüstriyel uygulamalara katkı sağlayacak metodolojik ve teorik olarak sağlam bir çerçeve sunmaktadır.

Anahtar Kelimeler: çok fazlı akış, iki fazlı akış, baloncuklu akış, HAD modelleme, fazlar arası momentum transferi, momentum kapatma ilişkileri

CONTENTS

	<u>Page</u>
ABSTRACT	i
ÖZET	iii
CONTENTS	v
TABLES	viii
FIGURES	ix
1. INTRODUCTION	7
1.1. Research Background	7
1.2. Research Objectives	8
1.3. Significance of the Research	8
1.4. Research Methodology	9
1.5. Thesis Structure	9
2. THEORETICAL BACKGROUND	11
2.1. Two-Fluid Model	15
2.2. Turbulence	19
2.2.1. Single-Phase Turbulence	20
2.2.2. Two-Phase Turbulence	25
3. LITERATURE REVIEW	31
3.1. Momentum Closure Models	31
3.1.1. Drag	32
3.1.2. Lift	37
3.1.3. Virtual Mass	41
3.1.4. Turbulent Dispersion	42
3.1.5. Wall Lubrication	44
3.2. Single-Phase Turbulence Closure Models	47
3.2.1. Algebraic Models	47
3.2.2. One-Equation Models	49
3.2.3. Two-Equation Models	50

3.2.4. Reynolds Stress Model (RSM)	52
3.3. Two-Phase Turbulence Closure Models	54
3.3.1. Algebraic Models	54
3.3.2. One-Equation Models.....	56
3.3.3. Two-Equation Models	56
3.3.4. Reynolds Stress Model (RSM)	61
3.4. Review of Experiments.....	65
3.5. Review of Simulations	69
4. METHODOLOGY.....	71
4.1. Design Space Exploration.....	72
4.2. Simulation	74
4.3. Automated Process Workflow.....	76
4.4. Test Case	77
5. DATA AND ANALYSIS	80
5.1. Experiment Groups	85
5.2. Single Phase	86
5.3. Default Parameters	88
5.3.1. Wall Peak.....	88
5.3.2. Core Peak.....	93
5.4. Parameter Tuning	94
5.4.1. Wall Peak.....	94
5.4.2. Core Peak.....	104
6. MODEL DEVELOPMENT AND VALIDATION	107
6.1. Model Description.....	107
6.2. Wall Peak	109
6.2.1. S1 new model set	109
6.2.2. S1-S2-S3 new model set	111
6.2.3. S1-S2-S3 new model set (F_{TD} and BIT)	114
6.2.4. H3-H4 new model set	118
6.3. Core Peak	120

6.3.1. H2 new model set	120
6.4. All Peak	122
6.4.1. H1-H2-H3-H4 new model vs. tuned set	122
7. DISCUSSION	126
8. CONCLUSION	128

TABLES

	<u>Page</u>
Table 3.1 Launder and Spalding $k-\varepsilon$ Model Coefficients.....	50
Table 3.2 Wilcox $k-\omega$ Model Coefficients.....	51
Table 3.3 Menter $k-\omega$ Model Coefficients.....	52
Table 3.4 “Filtered list of two-phase flows experiments from Hibiki et al. [1]” ...	67
Table 3.5 “Adapted List of closure model sets used in recent CFD studies from Irfan Khan et al. [2]”	69
Table 4.1 Closure model set and tuning parameter ranges	78
Table 4.2 Tuning parameters for the baseline and tuned models.....	78
Table 5.1 Limits and resolution for the variables	83
Table 5.2 List of reference experiments	86
Table 5.3 Limits and resolution for the variables	96
Table 5.4 Baseline vs. tuned model parameters for L1-L2-L3	96
Table 5.5 Baseline vs. tuned model parameters for H1-H2	104
Table 6.1 Limits for the new model coefficients	109
Table 6.2 Model coefficients for S1	110
Table 6.3 Model coefficients for S1-S2-S3	113
Table 6.4 Model coefficients for S1-S2-S3 (F_{TD} & BIT)	114
Table 6.5 BIT coefficients for S1-S2-S3	114
Table 6.6 Model coefficients for H3-H4 (F_{TD} & BIT)	119
Table 6.7 BIT coefficients for H3-H4	119
Table 6.8 Model coefficients for H2 with (F_{TD} & BIT)	120
Table 6.9 BIT coefficients for H2 (F_{TD} & BIT)	120
Table 6.10 Model coefficients for H1-H2-H3-H4 with (F_{TD} & BIT)	122
Table 6.11 BIT coefficients for H1-H2-H3-H4 with (F_{TD} & BIT)	122

FIGURES

	<u>Page</u>
Figure 3.1 Standard k- ε with Troshko-Hassan model	60
Figure 3.2 Standard k- ω with Troshko-Hassan model.....	61
Figure 3.3 SST k- ω with Troshko-Hassan model.....	62
Figure 3.4 Algebraic RSM with Sato viscosity model	63
Figure 3.5 Differential RSM model ($C_i = 0.25$)	65
Figure 3.6 Differential RSM model ($C_i = 0.02$)	66
Figure 4.1 Performance history plot.....	73
Figure 4.2 Baseline vs. tuned model comparison plot.....	79
Figure 5.1 H3 Void fraction (closure model sets)	83
Figure 5.2 H3 Turbulence kinetic energy (closure model sets)	84
Figure 5.3 H3 Relative velocity (closure model sets)	84
Figure 5.4 S0 results	87
Figure 5.5 L01-L02 results	88
Figure 5.6 H01-H02 results	89
Figure 5.7 S1 results 1 (default sets)	90
Figure 5.8 S1 results 2 (default sets)	91
Figure 5.9 S2 results (default sets)	92
Figure 5.10 S3 results (default sets)	93
Figure 5.11 L1 results (default sets)	94
Figure 5.12 L2 results (default sets)	95
Figure 5.13 L3 results (default sets)	96
Figure 5.14 H3 results (default sets)	97
Figure 5.15 H4 results (default sets)	98
Figure 5.16 H1 results (default sets)	99
Figure 5.17 H2 results (default sets).....	100
Figure 5.18 L1 results (tuned vs. default sets)	101

Figure 5.19	L2 results (tuned vs. default sets)	102
Figure 5.20	L3 results (tuned vs. default sets)	103
Figure 5.21	H1 tuned coefficient results (H1-H2)	105
Figure 5.22	H2 tuned coefficient results (H1-H2)	106
Figure 6.1	S1 (new model sets)	110
Figure 6.2	S1 model coefficient results (S1-S2-S3)	111
Figure 6.3	S2 model coefficient results (S1-S2-S3)	112
Figure 6.4	S3 model coefficient results (S1-S2-S3)	113
Figure 6.5	S1 model coefficient results (S1-S2-S3) (F_{TD} & BIT)	115
Figure 6.6	S2 model coefficient results (S1-S2-S3) (F_{TD} & BIT)	116
Figure 6.7	S3 model coefficient results (S1-S2-S3) (F_{TD} & BIT)	117
Figure 6.8	H3 model coefficients (F_{TD} & BIT)	118
Figure 6.9	H4 model coefficients (F_{TD} & BIT)	119
Figure 6.10	H2 model coefficient results (F_{TD} & BIT)	121
Figure 6.11	H1-H2-H3-H4 new coefficients vs. tuned set (F_{TD} & BIT)	123
Figure 6.12	H1-H2-H3-H4 new coefficients vs. tuned set (F_{TD} & BIT)	124
Figure 6.13	H1-H2-H3-H4 new coefficients vs. tuned set (F_{TD} & BIT)	125

Nomenclature

Roman Symbols

g	Body force	P_{ij}	Production term
n	Unit vector	t	Time
q	Heat flux vector	u_i	Velocity component in the i -direction
u	Velocity vector	u'_i	Fluctuating velocity component in the i -direction
x	Spatial position vector	u_m	Mixing velocity
\mathbb{I}	Unit vector	h	Enthalpy
\mathcal{J}	Efflux vector	m	Mass
\mathbb{T}	Surface stress tensor	e_y	Unit vector
$\overline{u'_i u'_j}$	Reynolds stress tensor	F_d^B	Basset force
D_{ij}	Turbulent diffusion term	F_d^D	Drag force
j	Superficial velocity	F_d^L	Lift force
k	Turbulence kinetic energy	F_d^V	Virtual mass force
l_m	Mixing length	F_d^{TD}	Turbulent dispersion force
p	Pressure	F_d^{WL}	Wall lift force
		F_D	Drag force

$F_{L\infty}$	Lift force	B_d	Volume of the particle
F_{TD}	Turbulent dispersion force	C_D	Drag coefficient
F_{VM}	Virtual mass force	C_j	Constraint violation for the j^{th} constraint
F_{WL}	Wall lubrication force	C_L	Tomiyama lift coefficient
g	Gravitational acceleration	$C_{\gamma 1}$	Power law function constant 1
M_d^B	Basset force per unit volume	$C_{\gamma 2}$	Power law function constant 2
M_d^D	Drag force per unit volume	$C_{D,\text{cap}}$	Drag coefficient for a cap
M_d^L	Lift force per unit volume	$C_{D,\text{ellipse}}$	Drag coefficient for an ellipse
M_d^V	Virtual mass force per unit volume	$C_{D,\text{sphere}}$	Drag coefficient for a sphere
M_d^{TD}	Turbulent dispersion force per unit volume	C_{Dm}	Modified drag coefficient according to Tomiyama's theoretical model
M_d^{WL}	Wall lift force per unit volume	C_{L0}	Nominal lift coefficient
M_{id}	Generalized drag force per unit volume	$C_{L\infty}$	Lift coefficient
n	Unit normal vector	C_{TD}	Turbulent dispersion coefficient
v_d	Velocity of the particle	C_{VM}	Virtual mass coefficient
v_g	Velocity of the gas phase	C_{W1}	Wall lubrication constant 1
v_l	Velocity of the liquid	C_{W2}	Wall lubrication constant 2
v_r	Relative velocity	C_{W3}	Wall lubrication constant 3
$\overline{E}_{\text{rel}}$	Mean relative error	C_{WC}	Wall lubrication cut-off coefficient
A_d	Cross-sectional area of the sphere	C_{WD}	Wall lubrication damping coefficient

C_{WL}	Wall lubrication coefficient	N	Number of measurement stations
D	Pipe diameter	$N_{con,j}$	Normalization value for the j^{th} constraint
d	Characteristic length scale, diameter	N_{con}	Number of constraints
D_b	Diameter of the bubble	$N_{obj,i}$	Normalization value for the i^{th} objective
E	Aspect ratio of the bubble	N_{obj}	Number of objectives
E_0	Aspect ratio of a bubble in infinite stagnant liquid	O_i	Response value for the i^{th} objective
F	Function dependent on aspect ratio E	P	Performance function
f	Void fraction dependency function	r_p	Radius of the particle
f_γ	Power law function	S_i	Sign for the i^{th} objective
f_α	α correction function	V_d	Volume of the spherical particle
f_d	d correction function	V_{exp}	Experiment result
f_{Eo_d}	Eo_d correction function	V_{sim}	Simulation result
f_{Eo}	Eo correction function	$W_{lin,i}$	Linear weight for the i^{th} objective
f_k	k correction function	$W_{lin,j}$	Linear weight for the j^{th} constraint
f_{Re_ω}	Re_ω correction function	$W_{quad,i}$	Quadratic weight for the i^{th} objective
f_{Re}	Re correction function	$W_{quad,j}$	Quadratic weight for the j^{th} constraint
f_{We}	We correction function	E_{rel}	Relative error
k_f	Turbulent kinetic energy of the liquid phase	y	Distance from the wall
m_d	Mass of the particle		

A^+	Empirical constant for wall damping factor
B_d	Volume of the particle
C_μ	Model constant for turbulent viscosity
$C_{\varepsilon 1}$	Model constant for k - ε model
$C_{\varepsilon 2}$	Model constant for k - ε model
C_{la1}	Empirical constant for bubble-induced turbulence near walls
C_{la}	Empirical constant for bubble-induced turbulence
C_{vm}	Virtual mass coefficient
u_η	Kolmogorov velocity scale
A	Area
C	Constant
D	Diameter
F	Force
k	Turbulent kinetic energy
L	Characteristic length
P	Pressure
Q	Flow rate
q	Volumetric heat source
u	Internal energy

V Volume

Abbreviations

BIT	Bubble Induced Turbulence
CFD	Computational Fluid Dynamics
DNS	Direct Numerical Simulation
FAD	Favre-Averaged Drag
HPC	High-Performance Computing
LES	Large Eddy Simulation
MDO	MultiDisciplinary Optimization
N-S	Navier-Stokes
RANS	Reynolds-Averaged Navier-Stokes
RSM	Reynolds Stress Model
RST	Reynolds Stress Transport

Dimensionless Numbers

E_o	Eötvös number
E_{od}	Modified Eötvös number
M	Morton number
Re	Two-phase Reynolds number
Re_d	Particle Reynolds number
Re_∞	Single-bubble Reynolds number
Re_ω	Rotational Reynolds number
Ta	Tadaki number

Fr	Froude number	μ_m	Mixture viscosity in the two-phase system
Pr	Prandtl number		
Re	Reynolds number	ν_f	Kinematic viscosity of the fluid
Sc	Schmidt number	ω_V	Vorticity
We	Weber number	ρ_d	Density of the particle
Greek Symbols		ρ_f	Density of the fluid
λ	Bulk viscosity	ρ_g	Density of the gas phase
μ	Dynamic viscosity	ρ_l	Density of the liquid phase
ν	Kinematic viscosity	σ	Surface tension
ω	Specific dissipation rate	ξ	Bubble deformation modification factor
ϕ	Source term	α	Model constant for k - ω model
Φ_{ij}	Pressure-strain correlation term	β	Model constant for k - ω model
Π_{ij}	Velocity-pressure gradient correlation term	β	Thermal expansion coefficient
ψ	Any physical quantity	β^*	Model constant for k - ω model
ρ	Density	δ	Boundary layer thickness
ε	Turbulence kinetic energy dissipation	η	Kolmogorov length scale
ε_{ij}	Dissipation term	κ	von Kármán constant
α	Void fraction	ω	Specific dissipation rate
μ	Dynamic viscosity	ϕ	Potential function
μ_l	Viscosity of the liquid	ρ	Density

σ_ω	Model constant for $k-\omega$ model	m	mixture
σ_ε	Model constant for $k-\varepsilon$ model	p	particle
σ_ε	Model constant for dissipation rate	S	source
σ_k	Model constant for $k-\varepsilon$ and $k-\omega$ models	a	area
σ_k	Model constant for shear-induced turbulence	g	gas phase
τ	Shear stress	i	Index
τ_η	Kolmogorov time scale	j	Index
		k	Index
		l	liquid phase

Oversymbols

$\overline{u_i}$	Mean velocity
\tilde{u}_i	Favre-averaged velocity

s	surface
t	turbulent
w	wall

Subscripts

b	bubble
d	dispersed
f	fluid
g	gas
i	i^{th} phase
k	k^{th} phase
l	liquid

Superscripts

e	eddy
mol	molecular
T	transpose
t	turbulent
$*$	dimensionless variable
$+$	non-dimensional wall units
$'$	fluctuating component

1. INTRODUCTION

This dissertation presents an in-depth investigation into multiphase flow, a pivotal area in nuclear engineering and across various engineering disciplines. The detailed understanding and accurate modeling of multiphase flow is essential for the enhancement of performance and the assurance of safety for variety of applications. This work aims to refine the connection between theoretical models and experimental observations, improve the accuracy of computational fluid dynamics (CFD) simulations, and contribute to the safe and efficient design of systems across numerous industries, including but not limited to, energy, aerospace and defense.

Multiphase flow dynamics is inherently complex, involving the interaction of multiple phases with distinct physical properties. These interactions lead to unique flow behaviors and patterns, challenging researchers and engineers to develop accurate predictive models. The complexity of these models is augmented by the varied scales and conditions under which multiphase flows occur.

1.1. Research Background

Multiphase, specifically bubbly two-phase flow dynamics is important in numerous industrial processes, with specific importance in nuclear energy. Accurate CFD modeling is important for understanding the performance of these processes, but it faces challenges due to narrow coverage of the current models, or so called momentum closure relations. The study on bubbly two-phase flows, has been a long lasting research, evolving from initial analytical and theoretical explorations to more complex numerical analyses. The focus was primarily on understanding the behavior and dynamics of single bubbles. Early research contributed significantly to foundational knowledge but was often limited in practical applications. Current research focuses on bubble dynamics, which represent applications of interest involving considerable volume fractions of bubble clusters. Although there is effort towards

improvements, this gap underlines the need for more generally applicable models, which forms the core motivation for this research.

1.2. Research Objectives

Proposal of a new, generally applicable drag and lift coefficient models for momentum closure required in CFD simulations of bubbly two-phase flow is the primary focus of this study. This involves not only the development of new coefficient models but also a new approach for evaluating these models against experimental data. The existing models often lack the ability to predict flow behaviors under varied conditions, necessitating the development of more applicable models.

Demonstration of the design exploration method use in multiphase flow research is the specific objective of this research. This method, utilizing the use of automated processes and efficient search algorithms, represents a novel approach in this field. Although there has been a growing interest and some initial efforts by researchers including but not limited to Bao et al. [3],[4], and Lucas et al. [5], to develop similar frameworks, the utilization of design exploration methods remains relatively unexplored and underutilized in multiphase flow studies. By the power of automation and advanced search algorithms, this research aims to improve the process of model development.

1.3. Significance of the Research

This research aims to contribute significantly to the field of CFD modeling by introducing a new approach to new model evaluation and development while addressing the gaps in current methodologies. Given the growing accessibility to compute clusters, high-performance computing (HPC) resources, the methodologies and findings of this study have the potential to be applied broadly in similar research areas, while contributing to the accuracy of two-phase flow CFD modeling.

1.4. Research Methodology

The method involves determining widely preferred existing closure model sets of fellow researchers for simulations of bubbly two-phase upward flow in cylindrical channels. An initial performance evaluation of the selected sets of using simulations against the available experimental databases is conducted. Following this, tunable model parameters of the selected closure model set are evaluated through design space exploration using a sophisticated search algorithm with the objective to minimize the simulation result deviation against experimental data on void fraction, relative velocity, and turbulent kinetic energy at measurement stations. Finally new models as functional forms for drag and lift coefficients with unknown constants is proposed. The unknown constants in these functions is determined with the same approach.

1.5. Thesis Structure

This structure is designed to cover the research process, from theory and literature review through to the final discussion and conclusions to provide insight into the development process of the new drag coefficient and lift coefficient models for bubbly two-phase flow CFD modeling and validating against relevant experiments.

Introduction: The Introduction briefly explains the research, outlining the motivation, objectives, and significance of the study. It provides the context and frames the study.

Theoretical Background: This chapter covers the fundamentals and principles of two fluid modeling, the basis of the solver used for CFD modeling. Single phase and two-phase turbulence modeling for CFD is detailed. Governing equations that the research methodology and model development rely on are introduced.

Literature Review: Examination of existing literature is presented. This review assesses previous studies, identifies gaps and positions the current research within context.

Methodology: This section describes in detail the method employed in this research, including the computational and design exploration tools used. Simulation set-up and automated processes for parameter optimization, and model evaluation is detailed and a test case is demonstrated.

Data and Analysis: Simulations with reference to the selected experiments are conducted with default parameters of the most preferred closure models set. Parameter tuning is demonstrated and comparison of default and tuned cases are detailed.

Model Development and Validation: This section details the development of new closure models and their subsequent validation. It discusses the refinement of the models based on the findings from the data analysis.

Discussion: Discussion section covers development and evaluation of the proposed models, key findings, challenges and limitations and recommendations for model improvement.

Conclusion: The Conclusion briefly explains the key findings and shows alignment with objectives. It highlights the contributions of the study to the CFD modeling research and outlines recommendations for further research.

2. THEORETICAL BACKGROUND

Two-phase flow is a complex fluid dynamics phenomenon with a common flow domain for different single phases. These phases are separated into distinct regions by dynamic interphases. The conventional differential balance equations are applicable to each of these phases. Particular considerations are required for the interfaces and the boundary conditions. The derivations and notations used throughout this subsection are adapted from Ishii's treatment of two-fluid modeling [6]. Ishii proposes that two-phase flow cases can be analyzed through spatial and instantaneous variables. The proposed approach, known as the local instant formulation, enables thorough assessment regarding overall flow characteristics.

The local instant formulation defines general flow properties such as phase velocities, common pressure, temperature, and phase distribution in space and instance without averaging. Averaged properties are smoothed over certain volumes and time frames. Through appropriate averaging methods the local instant formulation forms the basis for macroscopic models. These two-phase models require both phases to be addressed as continuum for the common flow domain.

This approach leads to a complex multi-boundary problem, where the interface locations are undetermined due to the interdependence of the fields. It can be applied directly to separated or sharp inter-phase flows and the dynamics of interfaces can be investigated. This formulation is applicable for the assessment of the behavior and dynamics of single bubbles and droplets, taking breakup and coalescence into account. Icing and melting can be analyzed as both are surface related phenomena and require interface tracking.

A simplified two-phase model is the mixture model which takes the relative motion between phases into account and is applicable to systems where one of the phases is dispersed with relatively low volume fraction. Mixture model is derived using the average velocity of the mixture. Slip velocity describes the relative motion of the phases. It is alternatively known as the drift-flux model.

Balance Equations

In fluid dynamics, both the theoretical and computational models are derived from the general conservation laws. As cited in Ishii's [6] work, these equations can be derived for any physical quantity ψ_k by considering the density ρ_k , the efflux vector \mathbf{J}_k , and the source term ϕ_k .

The fundamental balance equation is shown below;

$$\frac{\partial(\rho_k\psi_k)}{\partial t} + \nabla \cdot (\mathbf{u}_k\rho_k\psi_k) = -\nabla \cdot \mathbf{J}_k + \rho_k\phi_k \quad (1)$$

where k denotes the phase of interest. The first term, time derivative of the quantity of interest is followed by the convective term indicating the transfer due to fluid motion. The remaining terms denote the surface flux representing the transfer of the quantity of interest across the boundaries of the system and the volumetric source term describing the generation or consumption of the physical quantity within the system's volume. This equation represents a general form that applies to various conservation laws.

For the continuity equation, the respective terms are set as;

$$\psi_k = 1, \quad \phi_k = 0, \quad \mathbf{J}_k = 0 \quad (2)$$

results in Eq (3) shown below as,

$$\frac{\partial\rho_k}{\partial t} + \nabla \cdot (\rho_k\mathbf{u}_k) = 0 \quad (3)$$

Time derivative term denotes the change of mass of k^{th} -phase over time. Divergence term represents the net flow of mass of k^{th} -phase through the control volume. The divergence of mass flux accounts for spatial changes. The equation states, any change in mass of k^{th} -phase over time must be balanced by the mass of k^{th} -phase flowing through the volume. This is the mass conservation for cases without phase change.

For the momentum equation, relevant quantity is defined in terms of surface stress tensor, \mathbf{T}_k and body force \mathbf{g}_k ;

$$\psi_k = \mathbf{u}_k, \quad \phi_k = \mathbf{g}_k, \quad \mathbf{J}_k = -\mathbf{T}_k = p_k \mathbf{I} - \boldsymbol{\tau}_k \quad (4)$$

where \mathbf{T}_k is decomposed into the pressure term and viscous stress $\boldsymbol{\tau}_k$, with \mathbf{I} denoting the unit tensor.

$$\frac{\partial \rho_k \mathbf{u}_k}{\partial t} + \nabla \cdot (\rho_k \mathbf{u}_k \mathbf{u}_k) = -\nabla p_k + \nabla \cdot \boldsymbol{\tau}_k + \rho_k \mathbf{g}_k \quad (5)$$

Decomposing the stress tensor, the linear constitutive equation is obtained as;

$$\boldsymbol{\tau}_k = \mu_k \left[\nabla \mathbf{u}_k + (\nabla \mathbf{u}_k)^T \right] - \left(\frac{2}{3} \mu_k - \lambda_k \right) \nabla \cdot \mathbf{u}_k \mathbf{I} \quad (6)$$

where μ_k denote the dynamic and λ_k denote the bulk viscosity for the k^{th} -phase.

Without any body torque, conservation of angular momentum is;

$$\mathbf{T}_k = \mathbf{T}_k^T \quad (7)$$

where \mathbf{T}_k^T is the transposed tensor. This condition, applicable to non-polar fluids, implies that the torques due to the stress tensor do not contribute to the angular momentum. In the case of polar fluids, additional terms representing intrinsic angular momentum are required [7].

Energy conservation is described by taking internal, u_k and kinetic energy into account as;

$$\psi_k = u_k + \frac{v_k^2}{2}, \quad \phi_k = \mathbf{g}_k \cdot \mathbf{u}_k + \frac{\dot{q}_k}{\rho_k}, \quad \mathbf{J}_k = \mathbf{q}_k - \mathbf{T}_k \cdot \mathbf{u}_k \quad (8)$$

Here, \mathbf{q}_k and \dot{q}_k denote the heat flux and volumetric source.

$$\frac{\partial \rho_k \left(u_k + \frac{v_k^2}{2} \right)}{\partial t} + \nabla \cdot \left[\rho_k \left(u_k + \frac{\mathbf{u}_k^2}{2} \right) \mathbf{u}_k \right] = -\nabla \cdot \mathbf{q}_k + \nabla \cdot (\mathbf{T}_k \cdot \mathbf{u}_k) + \rho_k (\mathbf{g}_k \cdot \mathbf{u}_k) + \dot{q}_k \quad (9)$$

The equations (3), (4), (7), and (9) encapsulate the fundamental conservation equations. Accurate specification of fluxes, body sources, and the state equations are essential for the solution of these equations, ensuring a comprehensive and accurate representation of the physical phenomena in multi-phase flow systems.

Interfacial Balance (Jump Conditions)

Differential balance equations are typically confined to individual phases but do not cover phase interfaces. There is sharp variations and discontinuities at the interfaces and requires a specialized representation for the balance equations and is defined as the jump conditions.

Setting the surface quantity of interest and representing the source per interfacial area is given below as;

$$\psi_a = \rho_a \psi_s, \quad \phi_a = \phi_s \psi_a \quad (10)$$

The differential balance equation for the interface is expressed as:

$$\begin{aligned} \frac{d_s}{dt}(\psi_a) + \psi_a \nabla_s \cdot \mathbf{u}_i = & \sum_{k=1}^2 \{ \rho_k \psi_k \mathbf{n}_k \cdot (\mathbf{u}_k - \mathbf{u}_i) + \mathbf{n}_k \cdot \mathbf{J}_k \} \\ & - A^{\alpha\beta} g_{ln} (t_\alpha^n \mathbb{J}_a^l)_{,\beta} + \phi_a \end{aligned} \quad (11)$$

Here, $A^{\alpha\beta}$ and g_{ln} represent the surface and space metric tensors, respectively. t_α^n denotes the hybrid tensor and $()_{,\beta}$ is the surface covariant derivative. The subscripts s and a denote the quantity of interest per unit interface mass and interfacial area. [7]. \mathbf{u}_i denotes the surface velocity and \mathbf{n}_k unit vector.

Interfacial mass balance is,

$$\sum_{k=1}^2 \rho_k \mathbf{n}_k \cdot (\mathbf{u}_k - \mathbf{u}_i) = 0 \quad (12)$$

Interfacial mass efflux of the k^{th} phase can be presented as given below in Eq 13

$$\dot{m} \equiv \rho_k \mathbf{n}_k \cdot (\mathbf{u}_k - \mathbf{u}_i) \quad (13)$$

which leads to;

$$\sum_{k=1}^2 \dot{m} = 0 \quad (14)$$

This implies that the interface does not accumulate mass.

The interfacial momentum balance is represented by:

$$\sum_{k=1}^2 \left\{ \rho_k \mathbf{n}_k \cdot (\mathbf{u}_k - \mathbf{u}_i) \mathbf{u}_k + \mathbf{n}_k \cdot \boldsymbol{\tau}_k \right\} + (t_\alpha^n A^{\alpha\beta} \sigma)_{,\beta} = 0 \quad (15)$$

where the balance of momentum fluxes against the interfacial tension forces is considered.

Setting interfacial energy u_a per unit surface area for ψ , interface balance is represented as;

$$\begin{aligned} \frac{d_s u_a}{dt} + u_a \nabla_s \cdot \mathbf{u}_i = & \sum_{k=1}^2 \left\{ \rho_k \mathbf{n}_k \cdot (\mathbf{u}_k - \mathbf{u}_i) \left(u_k + \frac{\mathbf{u}_k^2}{2} \right) + \mathbf{n}_k \cdot (-\mathbf{T}_k \cdot \mathbf{u}_k + \mathbf{q}_k) \right\} \\ & + (t_\alpha^n A^{\alpha\beta} \sigma \cdot \mathbf{u}_i)_{,\beta} \end{aligned} \quad (16)$$

Left-hand terms denote the rate of change of surface energy and the remaining terms denote energy transfer of phases through the interphase and the work arising from surface tension.

2.1. Two-Fluid Model

This model is introduced by Ishii [8] as a framework for multiphase analysis and refined by Ishii and Mishima [9] for practical applications. The two-fluid model (TFM) approach takes

phases into account individually. This model utilities separate conservation equations for respective the phase. The most critical part of this model is the interaction between phases, that is, the averaged fields of each phase affect the other. This results in exchange terms in the balance equations, represented by Γ_k for mass, M_k for momentum and kE for energy of the k^{th} phase through the interfaces. All these interactions are constrained by balance laws defined for the interfaces, resulting in the formulation of interfacial transfer based on local discontinuities, referred to as the jump conditions. As a result, the macroscopic flow dynamics are governed by differential field equations, three per phase and three respective interfacial transfer equations, regarding the jump conditions.

The general balance equation of the k^{th} -phase, which address any quantity ψ_k with density ρ_k , efflux \mathbf{J}_k , and source term ϕ_k , is expressed as;

$$\frac{\partial \alpha_k \bar{\rho}_k \hat{\psi}_k}{\partial t} + \nabla \cdot (\alpha_k \hat{\mathbf{u}}_k \bar{\rho}_k \hat{\psi}_k) = -\nabla \cdot [\alpha_k (\bar{\mathbf{J}}_k + \mathbf{J}_k^T)] + \alpha_k \bar{\rho}_k \hat{\phi}_k + \mathbf{I}_k \quad (17)$$

with;

$$\sum_{k=1}^2 \mathbf{I}_k - \mathbf{I}_k = 0 \quad (18)$$

For mass conservation:

$$\frac{\partial (\alpha_k \bar{\rho}_k)}{\partial t} + \nabla \cdot (\alpha_k \bar{\rho}_k \hat{\mathbf{u}}_k) = \Gamma_k \quad (19)$$

Interfacial mass transfer condition:

$$\sum_{k=1}^2 \Gamma_k = 0 \quad (20)$$

For momentum conservation:

$$\frac{\partial (\alpha_k \bar{\rho}_k \hat{\mathbf{u}}_k)}{\partial t} + \nabla \cdot (\alpha_k \bar{\rho}_k \hat{\mathbf{u}}_k \hat{\mathbf{u}}_k) = -\nabla (\alpha_k \bar{p}_k) + \nabla \cdot [\alpha_k (\bar{\boldsymbol{\tau}}_k + \boldsymbol{\tau}_k^T)] + \alpha_k \bar{\rho}_k \mathbf{g}_k + M_k \quad (21)$$

The two-fluid model, has been adapted for three-dimensional analysis through temporal or statistical averaging. This model has two conservation equations, i.e. one per each phase. Additionally the interaction terms are set as source terms regarding the interdependency of the averaged fields per phase. For practical applications, Ishii and Mishima [9] have proposed simplified forms of the model as;

Continuity equation,

$$\frac{\partial(\alpha_k \rho_k)}{\partial t} + \nabla \cdot (\alpha_k \rho_k \mathbf{u}_k) = \Gamma_k \quad (22)$$

where Γ_k represent the mass generation,

Momentum equation,

$$\begin{aligned} \frac{\partial(\alpha_k \rho_k \mathbf{u}_k)}{\partial t} + \nabla \cdot (\alpha_k \rho_k \mathbf{u}_k \mathbf{u}_k) = & -\alpha_k \nabla p_k + \nabla \cdot [\alpha_k (\boldsymbol{\tau}_k^\mu + \boldsymbol{\tau}_k^T)] \\ & + \alpha_k \rho_k \mathbf{g} + \Gamma_k \mathbf{u}_{ki} + M_{ki} - \nabla \alpha_k \boldsymbol{\tau}_{ki} + (p_{ki} - p) \nabla \alpha_k \end{aligned} \quad (23)$$

where M_{ki} represent generalized interfacial drag, and $\boldsymbol{\tau}_{ki}$ represent interfacial shear stress,

Energy equation,

$$\begin{aligned} \frac{\partial(\alpha_k \rho_k h_k)}{\partial t} + \nabla \cdot (\alpha_k \rho_k h_k \mathbf{u}_k) = & -\nabla \cdot [\alpha_k (\mathbf{q}_k^C + \mathbf{q}_k^T)] \\ & + \alpha_k \frac{D_k p_k}{Dt} + (p_k - p_{ki}) \frac{D_k \alpha_k}{Dt} + \Gamma_k h_{ki} + a_i q_{ki}'' + \phi_k \end{aligned} \quad (24)$$

where q_{ki}'' , and ϕ_k represent interface heat flux and dissipation.

Through notation manipulation, simplifications for these equations are achieved by dropping the averaging symbols of, $\bar{\boldsymbol{\tau}}_k$, $\bar{\boldsymbol{\tau}}_{ki}$, and $\bar{\mathbf{q}}_k^C$ as $\boldsymbol{\tau}_k^\mu$, $\boldsymbol{\tau}_{ki}$, and \mathbf{q}_k^C , respectively.

Eq.s (22) to (24) include the interface transfer terms where the jump conditions are given below in Eq.s (25) and (26) as;

$$\sum_k \Gamma_k = 0 \quad (25)$$

and,

$$\sum_k (\Gamma_k, M_{ki}, a_i q_{ki}'' + \Gamma_k h_{ki}) = 0 \quad (26)$$

The generalized drag, M_{id} is the term needed for the closure and it is a linear superposition of several respective forces that can be presented as;

$$\begin{aligned} M_{id} &= \frac{\alpha_d}{B_d} (\mathbf{F}_d^D + \mathbf{F}_d^V + \mathbf{F}_d^B + \mathbf{F}_d^L + \mathbf{F}_d^{WL} + \mathbf{F}_d^T) \\ &= M_d^D + M_d^V + M_d^B + M_d^L + M_d^{WL} + M_d^T \end{aligned} \quad (27)$$

where the superscripts, D, V, B, L, WL, T denote the drag, virtual mass, Basset, lift, wall lubrication and turbulent dispersion respectively.

The details of the force models with their respective model coefficients are discussed in the Literature Review.

A representative example to derive the drag force on a particle in a carrier fluid is presented below. The particle is considered spherical with no shape deformation and the carrier fluid is assumed to be stagnant.

Equation of Motion of a Spherical Particle in Steady Fluid

As per Newton's second law, the equation of motion for the particle is derived considering the gravitational, buoyancy and drag force. For the steady-state condition, the equation is given by;

$$0 = m_d \cdot \mathbf{g} - V_d \cdot (\rho_l - \rho_d) \cdot \mathbf{g} - \frac{1}{2} \cdot C_D \cdot \rho_l \cdot A_d \cdot (\mathbf{v}_d - \mathbf{v}_l)^2 \quad (28)$$

Where the terms are, m_d , mass of the particle, V_d , volume of the particle, ρ_l , liquid density, ρ_d , particle's density, C_D , drag coefficient, A_d , particle's cross-sectional area, \mathbf{v}_d , velocity of the particle, \mathbf{v}_l , velocity of the liquid respectively.

This equation assumes the force balance and is used to specify particle's motion in the fluid.

This resistance force on the particle against the direction of movement has the general form shown in Eq. (29) below,

$$\mathbf{F}_D = \frac{1}{2} C_D \rho_f |\mathbf{v}_r| \mathbf{v}_r A_d \quad (29)$$

Where C_D , ρ_f , \mathbf{v}_r and A_d are the drag coefficient, carrier fluid density, relative velocity and the particle's cross-sectional area respectively.

2.2. Turbulence

Turbulence is a chaotic fluid flow phenomenon; however, turbulent flow also exhibits coherent structures and patterns. It is very complex in its nature due to rapid temporal and spatial changes of velocity and pressure. Turbulence drives mixing. Turbulent flow involves vortices and eddies in length scales. These length scales can be categorized as; integral length scale (L), being the largest scale, Taylor micro scale (λ), being the intermediate and the Kolmogorov length scale (η) being the smallest scale, with the order shown in Eq. (30).

$$L \gg \lambda \gg \eta \quad (30)$$

where the the integral length scale groups largest eddies. This group has the maximum contribution on the total turbulent kinetic energy. Kolmogorov length scale groups the intermediate sized eddies. This group holds both energy-containing and dissipative eddies.

Kolmogorov length scale groups the smallest, dissipative eddies. Molecular diffusion is dominant in this scale. Kolmogorov [10–12] describes the smallest scales for length (η), time (τ_η), and velocity (u_η) as shown in Eq. (31). Vortex stretching is the energy transfer mechanism from larger to smaller scales. Turbulence is dissipative, as energy is transferred to the smallest scales, it is dissipated.

$$\eta = \left(\frac{\nu^3}{\varepsilon}\right)^{1/4}, \quad \tau_\eta = \left(\frac{\nu}{\varepsilon}\right)^{1/2}, \quad u_\eta = (\nu\varepsilon)^{1/4} \quad (31)$$

As shown in Eq.(32), ε is the rate of kinetic energy dissipation for isotropic turbulence.

$$\varepsilon = -\frac{dk}{dt} \quad (32)$$

2.2.1. Single-Phase Turbulence

The Navier-Stokes (N-S) equations, derived from conservation equations, shown in Eqs. (33, 37) are the fundamental equations for the laminar and turbulent fluid motion. The derivations and notations used throughout this subsection are adapted from Wilcox's treatment of turbulence modeling [13].

$$\frac{\partial u_i}{\partial x_i} = 0 \quad (33)$$

is the mass conservation and,

$$\rho \left(\frac{\partial u_i}{\partial t} + u_j \frac{\partial u_i}{\partial x_j} \right) = -\frac{\partial p}{\partial x_i} + \frac{\partial \tau_{ji}}{\partial x_j} \quad (34)$$

is the momentum conservation, where p denotes the pressure and τ_{ij} is the stress tensor. In the case of a Newtonian fluid, by Newton's viscosity law presented earlier in Eq. (6) with μ , the molecular viscosity, leads to the stress-strain relation;

$$\tau_{ij} = 2\mu s_{ij} \quad (35)$$

where the strain rate tensor s_{ij} is show below in Eq.(36),

$$s_{ij} = \frac{1}{2} \left(\frac{\partial u_i}{\partial x_j} + \frac{\partial u_j}{\partial x_i} \right) \quad (36)$$

$$\rho \left(\frac{\partial u_i}{\partial t} + \frac{\partial}{\partial x_j} (u_j u_i) \right) = -\frac{\partial p}{\partial x_i} + \frac{\partial}{\partial x_j} (2\mu s_{ji}) \quad (37)$$

The continuity and momentum equations are coupled through the pressure term. To ensure the incompressibility condition a Poisson equation for the pressure field can be derived from the momentum and continuity equations, as shown below in Eq. 38

$$\frac{\partial^2 p}{\partial x_i^2} = -\rho \frac{\partial}{\partial x_i} \left(\frac{\partial u_j}{\partial t} + u_k \frac{\partial u_j}{\partial x_k} \right) \quad (38)$$

This equation shows how the pressure field is calculated by the velocity field while the divergence remains zero.

Turbulence Closure

Turbulence can either be solved or modeled. For the solution of turbulence, the Direct Numerical Simulations (DNS) method can be applied to the N-S equations [14]. DNS resolves all scales of turbulence, from largest eddies to Kolmogorov scale. However, DNS is computationally infeasible for most practical engineering cases due to the range of scales and respective resolution.

The grid size for DNS simulations should be equivalent to the Kolmogoro scale, offering high accuracy but incurring huge computational costs.

Modeling, on the other hand, requires fewer computational resources with a compromise in accuracy. Modeling can be classified as statistical and scale-resolving. Statistical models are derived from Reynolds averaging of N-S equations and are used to model all scales.

Rapid changes in turbulent flows are turbulent fluctuations that can be defined mathematically with appropriate averaging techniques. Reynolds averaging decomposes and separates the instantaneous velocity and pressure forming the time-averaged and fluctuating components.

$$u_i(x, t) = U_i(x) + u'_i(x, t) \quad (39)$$

$$p(x, t) = P(x) + p'(x, t) \quad (40)$$

where u_i and p denote the instantaneous velocity and pressure. U_i and P are the mean velocity and pressure. u'_i and p' are the fluctuating velocity and pressure. By using Reynolds averaging, the chaotic structure of turbulence can be defined theoretically. After decomposing and appropriate manipulation, the Reynolds-Averaged N-S (RANS) equations are presented in Eqs. (41, 42).

$$\frac{\partial U_i}{\partial x_i} = 0 \quad (41)$$

$$\rho \left(\frac{\partial U_i}{\partial t} + U_j \frac{\partial U_i}{\partial x_j} \right) = -\frac{\partial P}{\partial x_i} + \frac{\partial}{\partial x_j} (2\mu S_{ij} - \rho \overline{u'_i u'_j}) \quad (42)$$

here the additional term $\rho \overline{u'_i u'_j}$ denotes the Reynolds stress tensor, (\mathbf{R}_{ij}) which represents the momentum transport driven by the turbulent fluctuations and is given in Eq. (43).

$$\mathbf{R}_{ij} = -\rho \overline{u'_i u'_j} \quad (43)$$

Average kinetic energy is expressed as in Eq. (44);

$$\frac{1}{2}U'_i U'_i + \frac{1}{2}\overline{u'_i u'_i} \quad (44)$$

where the sum of the normal Reynolds stresses is related to the turbulence kinetic energy k as shown below in Eq. (45)

$$k = \frac{1}{2}\overline{u'_i u'_i} \quad (45)$$

Reynolds stress transport (RST) equation is shown below;

$$\frac{\partial \mathbf{R}_{ij}}{\partial t} + U_k \frac{\partial \mathbf{R}_{ij}}{\partial x_k} = -\mathbf{R}_{ik} \frac{\partial U_j}{\partial x_k} - \mathbf{R}_{jk} \frac{\partial U_i}{\partial x_k} + \varepsilon_{ij} - \Pi_{ij} + \frac{\partial}{\partial x_k} \left(\nu \frac{\partial \mathbf{R}_{ij}}{\partial x_k} + C_{ijk} \right) \quad (46)$$

where the pressure-strain correlation;

$$\Pi_{ij} = \frac{p'}{\rho} \overline{\left(\frac{\partial u'_i}{\partial x_j} + \frac{\partial u'_j}{\partial x_i} \right)} \quad (47)$$

dissipation tensor;

$$\varepsilon_{ij} = 2\nu \overline{\frac{\partial u'_i}{\partial x_k} \frac{\partial u'_j}{\partial x_k}} \quad (48)$$

and the triple velocity correlation;

$$\rho C_{ijk} = \overline{u'_i u'_j u'_k} + \overline{p' u'_i} \delta_{jk} + \overline{p' u'_j} \delta_{ik} \quad (49)$$

The relation between the kinematic eddy viscosity, turbulent length scale l and turbulence kinetic energy k is given below in Eq. (50) as;

$$\nu_t \approx k^{1/2} l \quad (50)$$

and the trace of the \mathbf{R}_{ii} is;

$$\mathbf{R}_{ii} = -\overline{u'_i u'_i} = -2k \quad (51)$$

and the trace of the RST equation gives the turbulence kinetic energy k equation presented in Eq. (52)

$$\frac{\partial k}{\partial t} + U_j \frac{\partial k}{\partial x_j} = \tau_{ij} \frac{\partial U_i}{\partial x_j} - \varepsilon + \frac{\partial}{\partial x_j} \left[(\nu + \nu_t / \sigma_k) \frac{\partial k}{\partial x_j} \right] \quad (52)$$

This rises a closure problem requiring additional equations or models for the solution of Reynolds stresses. One option is solving the transport equation for all Reynolds stresses. Since this tensor is symmetric, a total of six transport equations will be added. Addition of one more equation for the dissipation results in 7 equations and this model is the Reynolds Stress Transport Model (RSM). RSM preserves the anisotropic behavior of turbulence.

RANS equations focus on predicting the mean flow behavior rather than resolving the detailed turbulent fluctuations. RANS simulations are generally less computationally expensive than DNS or large eddy simulations (LES), which resolve a wider range of turbulent scales.

The Boussinesq hypothesis [15] is often employed in turbulence modeling to link Reynolds stresses with mean velocity gradients. It postulates that Reynolds stresses are proportional to the mean strain rate through turbulent viscosity (ν_t). Eddy viscosity (also called turbulent viscosity) does not represent a fluid property like molecular viscosity (μ). Instead, it's a flow-dependent parameter that quantifies the turbulent mixing and momentum transport due to eddies. Different turbulence models use different approaches for eddy viscosity calculation via mean flow properties.

here; the Reynolds stress tensor shown in Eq. (53) is presented by Boussinesq eddy viscosity approximation relation;

$$\mathbf{R}_{ij} = 2\nu_t S_{ij} - \frac{2}{3}k\delta_{ij} \quad (53)$$

Law of the Wall

The single-phase law of the wall describes the velocity profile of turbulent flow in the proximity of wall boundaries. This empirical relationship divides the boundary layer into three regions, namely, the viscous sub-layer, the buffer layer, and the logarithmic layer [16].

Flow is considered laminar in the viscous sub-layer. In the logarithmic layer, turbulence dominates the flow. The velocity profiles follows the viscous sub-layer and the logarithmic laws given in Eq.s (54, 55) respectively while no law is applicable to the buffer layer.

$$u^+ = y^+ \quad (54)$$

$$u^+ = \frac{1}{\kappa} \ln(y^+) + B \quad (55)$$

where u^+ and y^+ are the dimensionless velocity and wall distance. κ is the von Kármán constant (approximately 0.41), and B is an empirical constant.

The law of the wall is crucial for modeling turbulent boundary layers. More complex two-phase wall laws are derived from these laws.

2.2.2. Two-Phase Turbulence

Research in single-phase turbulence is relatively developed and there are variety of turbulence models. These models are categorized as, algebraic, one-equation, two-equation and stress models. While same categorization can be considered for multiphase turbulence, modeling remains relatively underdeveloped.

Two-phase turbulence can be modeled in either of the two approaches, mixture turbulence and per phase turbulence approaches. In mixture turbulence approach, a single turbulence model is used whereas in per-phase approach, both phases are taken into account individually. While applicable to alternatives, a representative example is presented for the k - ε model.

Mixture Turbulence

In this approach, one set of turbulence equations are solved using mixture properties and mixture velocities.

Since turbulence kinetic energy is the energy per mass of the velocity fluctuations, and dissipation is rated by density, k_m and ε_m are defined as;

$$k_m = k_i, \quad \varepsilon_m = \varepsilon_i \quad (56)$$

and defining mixture properties as;

$$\rho_m = \sum_i^n \alpha_i \rho_i, \quad \mu_m = \sum_i^n \alpha_i \mu_i \quad (57)$$

with the definition of average mixture velocity,

$$\bar{\mathbf{u}}_m = \frac{\sum_i^n \alpha_i \rho_i \mathbf{u}_i}{\sum_i^n \alpha_i \rho_i} \quad (58)$$

mixture turbulent eddy viscosity and the phase turbulent viscosity with the assumption of equal kinematic viscosities of the phases are,

$$\nu_m^t = \nu_i^t, \quad \mu_m^t = \frac{\rho_m \mu_i^t}{\rho_i}, \quad \mu_i^t = \frac{\rho_i \mu_m^t}{\rho_m} \quad (59)$$

and the mixture k - ε turbulence model is defined as;

$$\begin{aligned} & \frac{\partial}{\partial t}(\rho_m k_m) + \nabla \cdot (\rho_m \bar{\mathbf{u}}_m k_m) \\ &= \nabla \cdot \left[\left(\mu_m + \frac{\mu_m}{\sigma_k} \right) \nabla k_m \right] + P_m^k - \rho_m (\varepsilon_m - \varepsilon_0) + S_m^k \end{aligned} \quad (60)$$

$$\begin{aligned} & \frac{\partial}{\partial t}(\rho_m \varepsilon_m) + \nabla \cdot (\rho_m \bar{\mathbf{u}}_m \varepsilon_m) \\ &= \nabla \cdot \left[\left(\mu_m + \frac{\mu_m^t}{\sigma_\varepsilon} \right) \nabla \varepsilon_m \right] + \left[\frac{1}{t_m^e} C_{\varepsilon 1} P_m^\varepsilon - C_{\varepsilon 1} f_2 \rho_m \left(\frac{\varepsilon_m}{t_m^e} - \frac{\varepsilon_0}{t_m^0} \right) + S_m^\varepsilon \right] \end{aligned} \quad (61)$$

where $t_m^e = k_m/\varepsilon_m$, $C_{\varepsilon 1}$, $C_{\varepsilon 2}$ and f_2 are, mixture large eddy time scale, model coefficients and a damping function respectively.

Per-phase Turbulence

This approach takes each phase into account individually. Interface mechanisms such as the drag, and other forces affect shear production effecting turbulence of the continuous phase either by amplifying or damping. In per-phase approach, turbulence is modeled for the continuous phase. For the dispersed phase, turbulence can either be modeled or coupled with the continuous phase via turbulence response models.

Continuous Phase Turbulence

A single phase turbulence transport equation set can be modified by operating with the phase void fractions and introducing additional source terms to model the phase interactions.

As an illustration, two-phase k - ε turbulence model is presented as;

$$\begin{aligned} & \frac{\partial}{\partial t}(\alpha_l \rho_l k_l) + \nabla \cdot (\alpha_l \mathbf{u}_l k_l) \\ &= \nabla \cdot \left(\alpha_l \left[\left(\mu_l^{mol} + \frac{\mu_l^t}{\sigma_k} \right) \nabla k_l \right] \right) + \alpha_l (T_l^{Re} : \nabla \mathbf{u}_l - \rho_l \varepsilon_l) + S_l^k \end{aligned} \quad (62)$$

$$\begin{aligned}
& \frac{\partial}{\partial t}(\alpha_l \rho_l \varepsilon_l) + \nabla \cdot (\alpha_l \mathbf{u}_l \varepsilon_l) \\
& = \nabla \cdot \left(\alpha_l \left[\left(\mu_l^{mol} + \frac{\mu_l^t}{\sigma_\varepsilon} \right) \nabla \varepsilon_l \right] \right) + \alpha_l \frac{\varepsilon_l}{k_l} (C_{\varepsilon 1} T_l^{Re} : \nabla \mathbf{u}_l - C_{\varepsilon 2} \rho_l \varepsilon_l) + S_l^\varepsilon \quad (63)
\end{aligned}$$

As the form of the equations remain the same, all terms are operated by the continuous phase void fractions. Additional source terms S_l^k and S_l^ε are included to take phase interactions into account.

Dispersed Phase Turbulence

Turbulence for the dispersed phase can either be modeled directly or can be modeled via a response model approach. Any available turbulence model can be used for the dispersed phase. Similarly, additional source terms to represent phase interactions are introduced to the corresponding turbulence transport equations.

Particle Induced Turbulence

The presence of a dispersed phase can either augment or dampen the turbulence in the continuous phase. This can be considered in two ways, by an additional source term to the turbulence equation or by the modification of the effective viscosity. Both require semi-empirical models. The correlations are derived by a response function that is defined as the ratio of the dispersed versus continuous phase velocity fluctuation.

As a representative example, the following relations are given where the turbulent stress is presented by the eddy-viscosity approach;

$$\mu^t = \rho C_\mu \frac{k^2}{\varepsilon} \quad (64)$$

where, C_μ is a k - ε model constant. The response function C_t is shown below;

$$C_t = \frac{|\mathbf{u}'_d|}{|\mathbf{u}'_l|} \quad (65)$$

where \mathbf{u}'_d and \mathbf{u}'_l are the fluctuating velocities of the dispersed and continuous phases respectively.

If k - ε model is used for the continuous phase, then the dispersed-phase turbulent kinetic energy is;

$$k_d = C_t^2 k_l \quad (66)$$

and the turbulent eddy viscosity is;

$$\mu_d^t = \frac{\rho_d}{\rho_l} C_t^2 \mu_c^t \quad (67)$$

Two-Phase Law of the Wall

To accurately model the behavior of two-phase turbulent boundary layers, it is essential to modify the single-phase laws to incorporate the effects of dispersed phases. A modified logarithmic law that includes a term to consider the bubble-induced component is necessary. The form of the wall law function for monodispersed and polydispersed cases can be in the form presented in Eq.s (68),((69)

$$u^+ = \frac{1}{\kappa} \ln(y^+) + B - u_{BI}^+ \quad (68)$$

$$u^+ = \frac{1}{\kappa} \ln(y^+) + B - \sum_{i=1}^N u_{BI}^+ \quad (69)$$

where u_{BI}^+ denotes the dispersed phase contribution and N the total number of particle size groups regarding the poly-dispersed case.

Several researches have proposed two-phase wall laws and they are reviewed in the Literature Review section.

3. LITERATURE REVIEW

This section provides review of research on two-phase flow emphasizing momentum and two-phase turbulence closure models. To provide more comprehensive understanding of the reviewed two-phase turbulence closure models, single-phase models are reviewed in advance regarding the connections between single and two-phase turbulence phenomena with the required modifications towards accurately modeling two-phase flows.

Additionally, conducted reference experiments of bubbly upward flow are examined. The review of experiments provides a clearer understanding of the range of various parameters of the conducted experiments such as pipe dimensions, velocities, void fractions while enabling the selection of appropriate benchmark cases for testing the method and models proposed in this thesis.

Lastly, related CFD studies are reviewed to show the methods used for two-phase flows simulations. This includes an assessment of different closure models employed in previous research which allows the identification of best practices and improvement opportunities.

This literature review highlights the current state flow and identifies on future directions of research in two-phase flow.

3.1. Momentum Closure Models

Momentum closure models have great importance in CFD studies. These closure models provide the necessary correlations. The precision and reliability of CFD simulations in predicting two-phase flow dynamics and behaviors is significantly dependent and on these models.

Closure models can be categorized according to the method of development. Analytical models are based on theoretical principles, offer insights into momentum transfer in two-phase flows. They are foundational but often too simplified for complex applications. Numerical Models blend theoretical and empirical models, increasingly recognized for their

adaptability across various flow regimes. Experimental Models arising from experimental data, offer practical insights but may lack universality across different conditions.

3.1.1. Drag

The drag force, (F_D) arises when a particle moves relative to the carrier fluid. This force is effective in the opposite direction of the particle's relative motion. In this context, single bubbles, liquid droplets, or solid particles moving through a continuous phase experience the drag force which effects the motion for both phases in a coupled fashion.

The magnitude of this force is a function of various parameters. The particles may have spherical or non-spherical shapes. The shape and size of the particle directly effects drag. The magnitude of particle's velocity relative is another parameter where drag force has linear dependency. Additionally, fluid properties, including density and viscosity, also affect the drag force magnitude.

In a mixture of liquid and bubbles, the drag force determines how quickly the bubbles rise, affecting the overall flow pattern. This interaction is particularly important for understanding the motion of bubbles.

When a system includes multiple particles, swarm effect phenomena emerges. This rises modification requirement to the drag force. The significant variable for this modification is the void fraction. Higher void fractions indicate denser swarms, altering the drag force experienced by each particle. To accurately model these effects, it's essential to incorporate model coefficients that adjust for variables like void fraction. These coefficients are derived from empirical data or simulations.

Various drag coefficient, (C_D) models have been proposed by different researchers is reviewed in the following part of this section. It is noted that, flow conditions and particle shape deformations affect the drag force and researchers account for these factors using different approaches.

Analytical Drag Coefficient Model

Analytically, C_D can be derived by Stokes' Law. It is noted that the model is for spherical, relatively small particles in a viscous fluid and is expressed as shown in Eq.(70)

$$C_D = \frac{24}{Re_d} \quad \text{for } 0 \leq Re_d \leq 0.2 \quad (70)$$

This model estimates the C_D for spherical particles in steady flow where the particle Reynolds number is very low. There is only Re_d dependency for the model.

Schiller-Neumann Drag Coefficient Model

Schiller and Neumann [17] expresses their drag coefficient, C_D model in Eq. (71) as a conditional function. Schiller and Neumann drag coefficient model is a composite function and depends on particle Reynolds number (Re_d). The model converges a constant value of 0.44 for the condition of $Re_d > 1000$.

$$C_D = \begin{cases} \frac{24}{Re_d} (1 + 0.15Re_d^{0.687}) & \text{if } Re_d \leq 1000, \\ 0.44 & \text{if } Re_d > 1000. \end{cases} \quad (71)$$

This model estimates the drag coefficient for rigid, small, spherical particles in fluid flow, useful for predicting the resistance experienced by the particles.

Ishii and Zuber Drag Coefficient Model

While solid particles can be assumed rigid, droplets and bubbles may experience shape deformations in certain conditions. Ishii and Zuber [18] introduces the shape deformation through a dimensionless parameter Eötvös Number (Eo) shown in Eq. (72).

$$Eo = \frac{g(\rho_l - \rho_g)d^2}{\sigma} \quad (72)$$

Eo quantifies the influence of gravity, (g) versus surface tension, (σ) at the fluid interfaces.

Ishii and Zuber's [18] C_D model is given in Eq. (73) in a composite form.

$$C_D = \max \left(C_{D,\text{sphere}}, \min \left(C_{D,\text{ellipse}}, C_{D,\text{cap}} \right) \right) \quad (73)$$

where the model in the case of a spherical particle is presented as;

$$C_{D,\text{sphere}} = \frac{24}{Re_\infty} (1 + 0.1 Re_\infty^{0.75}) \quad (74)$$

and for the ellipse shaped particle, it is defined as;

$$C_{D,\text{ellipse}} = \frac{2}{3} \sqrt{Eo} \quad (75)$$

and for the cap shaped particle is defined with a constant value as;

$$C_{D,\text{cap}} = \frac{8}{3} \quad (76)$$

The relation for the single particle Reynolds number, Re_∞ is;

$$Re_\infty = \frac{\rho_l |\mathbf{v}_r| D_b}{\mu_l} \quad (77)$$

The Ishii-Zuber model is particularly useful in multiphase flows, to calculate the drag force on spherical, elliptical, and cap shaped particles.

Ishii and Zuber Multiparticle Drag Coefficient Model

Alongside their single particle model, Ishii and Zuber [18], introduced their modified coefficient model to account for multi-particle systems. They added void fraction dependency $f(\alpha)$ to their model given in Eq.s (80) and (81).

$$\text{Stokes regime: } C_D = \frac{24}{Re} \quad (78)$$

$$\text{Undistorted bubble regime: } C_D = \frac{24}{Re} (1 + 0.1Re^{0.75}) \quad (79)$$

$$\text{Distorted bubble regime: } C_D = \frac{2}{3} D_b \sqrt{\frac{g\Delta\rho}{\sigma}} \left\{ \frac{1 + 17.67f(\alpha)^{6/7}}{18.67f(\alpha)} \right\}^2 \quad (80)$$

$$\text{Cap bubble regime: } C_D = \frac{8}{3} (1 - \alpha)^2 \quad (81)$$

where D_b , $\Delta\rho$, are the bubble diameter, density difference, respectively.

Two-phase Reynolds number, Re is modified as a function of mixture viscosity and is presented in Eq. (82) as;

$$Re = \frac{\rho_l |\mathbf{v}_r| D_b}{\mu_m} \quad (82)$$

where the two-phase mixture viscosity with void fraction, α dependency is;

$$\frac{\mu_m}{\mu_l} = (1 - \alpha)^{-1} \quad (83)$$

Tomiyama Drag Coefficient Model

In their study, Tomiyama et al. [19], proposed C_D model for bubbles, taking into account the bubble shape and the level of liquid contamination. This model differentiates between clean Eq. (84), slight Eq. (85) and heavy Eq. (86) contamination of the liquid shown as;

$$C_D = \max \left[\min \left[\frac{16}{Re_\infty} (1 + 0.15Re_\infty^{0.687}), \frac{48}{Re_\infty} \right], \frac{8}{3} \frac{Eo}{Eo + 4} \right], \quad (84)$$

$$C_D = \max \left[\min \left[\frac{24}{Re_\infty} (1 + 0.15Re_\infty^{0.687}), \frac{72}{Re_\infty} \right], \frac{8}{3} \frac{Eo}{Eo + 4} \right], \quad (85)$$

$$C_D = \max \left[\frac{24}{Re_\infty} (1 + 0.15 Re_\infty^{0.687}), \frac{8}{3} \frac{Eo}{Eo + 4} \right] \quad (86)$$

here Re_∞ denotes the single-bubble Reynolds number as presented in Eq. (87).

$$Re_\infty = \frac{\rho_l |\mathbf{v}_{r\infty}| D_b}{\mu_l} \quad (87)$$

where $v_{r\infty}$ is the relative velocity of a single bubble.

Tomiyama Theoretical Drag Coefficient Model

Tomiyama et al. [20] modified and introduced their theoretical drag coefficient C_{Dm} model in Eq. (88) to include the bubble aspect ratio, E , presented below in Eq. (89).

$$C_{Dm} = \frac{8}{3} \frac{Eo}{E^{2/3}(1 - E^2)^{-1}Eo + 16} E^{4/3} F^{-2} \quad (88)$$

$$F = \frac{\sin^{-1}(\sqrt{1 - E^2}) - E\sqrt{1 - E^2}}{1 - E^2} \quad (89)$$

Vakrushev and Efremov [21] provided the following correlation to evaluate E_0 :

$$E_0 = \begin{cases} 1, & Ta < 1 \\ \{0.81 + 0.206 \tanh[2(0.8 - \log_{10} Ta)]\}^3, & 1 < Ta < 39.8 \\ 0.24, & 39.8 \leq Ta \end{cases} \quad (90)$$

The Tadaki number Ta and the Morton number M is defined as:

$$Ta = Re \cdot M^{0.23} \quad (91)$$

$$M = \left(\frac{\mu^4(\rho_l - \rho_g)\mathbf{g}}{\rho_l^2\sigma^3} \right) \quad (92)$$

Using their pipe flow experimental data, they correlated the the expression shown in Eq.(93) which approaches to the constant value of 0.65 towards the center of the circular pipe.

$$\frac{E}{E_0} = \max \left(1.0 - 0.35\frac{y}{d}, 0.65 \right) \quad (93)$$

where y/d denotes the dimensionless wall distance.

This modification to include the aspect ratio E suggests an improvement in the model to handle the force balance for non-spherical particles including elongated bubbles. This is particularly relevant in conditions where spherical shape is no longer sustained.

3.1.2. Lift

Lift force (F_L) is the force acting on a particle in the lateral direction relative to its movement. F_L is affected by the liquid shear and particle size. Shear gradients causes uneven pressure distribution on the particle-fluid interface, resulting in lateral force imbalance. The wake of a particle creates vortices and turbulent eddies. Other particles entering these wake regions experience pressure and velocity changes causing lateral force imbalance. A solid boundary also affects the flow field in proximity to the particle. The rotation of a particle affects the flow field causing difference in pressure on the it's surface. When modeling lift, all these mechanisms should be taken into consideration.

Various lift force F_L and lift coefficient (C_L) models were introduced by different researchers. These are reviewed in the following part of this section. It is noted that, flow conditions and particle shape deformations affect the lift force and these have been incorporated by the researchers.

Saffman Lift Force Model

Saffman [22] proposed the analytical lift force model in Eq. (94). This model is for a single rigid spherical particle.

$$\mathbf{F}_{L\infty} = 6.46\rho_f\nu_f^{1/2}\mathbf{v}_{r\infty}r_p^2\omega^{1/2} \quad (94)$$

where ω denotes the velocity gradient magnitude.

Žun Lift Force Model and Coefficient

Žun [23] proposed the single particle lift force model in Eq. (95). The lift coefficient $C_{L\infty}$ of Žun is a constant value of 0.3.

$$\mathbf{F}_{L\infty} = C_{L\infty}\frac{4}{3}\pi\rho_fr_p^3\mathbf{v}_{r\infty} \times (\nabla \times \mathbf{v}_f) \quad (95)$$

Auton Lift Force Model and Coefficient

Auton [24] proposed a constant $C_{L\infty}$ value, 0.5 for the same force model proposed by Žun [23].

$$\mathbf{F}_{L\infty} = C_{L\infty}\frac{4}{3}\pi\rho_fr_p^3\mathbf{v}_{r\infty} \times (\nabla \times \mathbf{v}_f) \quad (96)$$

Drew and Lahey Lift Force Model and Coefficient

Drew and Lahey [25] presented the single spherical particle lift force model in Eq.(97)with the virtual mass coefficient C_{VM} dependency.

$$\mathbf{F}_L = \alpha_d C_{VM} \rho_c (\mathbf{v}_d - \mathbf{v}_c) \cdot [\nabla \mathbf{v}_c + (\nabla \mathbf{v}_c)^T] \quad (97)$$

where \mathbf{v}_d and \mathbf{v}_c denote the dispersed and continuous phase velocities.

Their model is valid for incompressible and inviscid flow conditions.

Wang Lift Coefficient

Wang et al. [26] proposed the lift force model in Eq. (98) Their lift coefficient model, given in Eq. (99) is based on the empirical correlation driven from the experimental study.

$$\mathbf{M}_d^L = C_L \rho_f \alpha_d \mathbf{v}_r \frac{\partial \mathbf{v}_f}{\partial r} \quad (98)$$

$$C_L = 0.01 + \frac{0.49}{\pi} \cot^{-1} \left(\frac{\log \zeta + 9.3168}{0.1963} \right) \quad (99)$$

$$\zeta = e^{-\alpha_g} \frac{d_b}{\mathbf{v}_r} \frac{d\mathbf{v}_f}{dr} \left(\frac{d_b \mu_f}{D \mu_m} \frac{1}{N_{Re}} \frac{\mathbf{v}_g}{1.18(\sigma g / \rho_f)^{1/4}} \right) \quad (100)$$

Legendre and Magnaudet

Legendre and Magnaudet [27] proposed the model in Eq. (101)

$$\mathbf{F}_{L\infty} \mathbf{e}_y = \rho_f B_d C_{L\infty} \mathbf{v}_{r\infty} \times \omega_V \quad (101)$$

where \mathbf{e}_y is the unit vector. B_d is the particle volume and ω_V denotes the vorticity.

Legendre and Magnaudet's model for lift coefficient $C_{L\infty}$ is given below in Eq. (102);

$$C_{L\infty} = \sqrt{\{C_{L\infty}^{low N_{Re\infty}}(N_{Re\infty}, G_{S\infty})\}^2 + \{C_{L\infty}^{high N_{Re\infty}}(N_{Re\infty})\}^2} \quad (102)$$

where;

$$C_{L\infty}^{low N_{Re\infty}}(N_{Re\infty}, G_{S\infty}) = \frac{6}{\pi^2 (2N_{Re\infty}, G_{S\infty})^{1/2}} \frac{2.255}{(1 + 0.2\epsilon_{\infty}^{-2})^{3/2}} \quad (103)$$

and,

$$C_{L\infty}^{highNRe\infty}(N_{Re\infty}) = \frac{1}{2} \frac{1 + 16N_{Re\infty}^{-1}}{1 + 29N_{Re\infty}^{-1}} \quad (104)$$

Tomiyama Lift Coefficient

Tomiyama [28] introduced the Modified Eötvös Number (Eo_d) shown in Eq. (105), to adjust the standard Eötvös number to include the aspect ratio (E) according to their drag coefficient model.

$$Eo_d = Eo \times E^{-2/3} \quad (105)$$

and introduced the piecewise lift coefficient model shown in Eq. (106) as a function of Eo_d .

$$C_L = \begin{cases} \min[0.288 \tanh(0.121Re), f_T(Eo_d)] & \text{if } Eo_d < 4, \\ f_T(Eo_d) & \text{if } 4 \leq Eo_d \leq 10.7, \\ -0.27 & \text{if } Eo_d > 10. \end{cases} \quad (106)$$

where

$$f_T(Eo_d) = 0.00105Eo_d^3 - 0.0159Eo_d^2 - 0.0204Eo_d + 0.474. \quad (107)$$

Ishii Lift Coefficient

Hibiki and Ishii [29] modified the Legendre and Magnaudet [27] lift force model with a modification coefficient, ξ to handle shape deformation of particles,

$$C_{L\infty} = \xi \sqrt{(C_{L\infty}^{lowRe})^2 + (C_{L\infty}^{highRe})^2} \quad (108)$$

where the modification coefficient ξ is expressed as;

$$\xi = 2 - \exp(0.136Eo^{1.11}) \quad (109)$$

Shaver and Podowski Wall Damping Lift Coefficient Model

Shaver and Podowski [30] suggested a modification to the lift force, through their lift coefficient model, particularly close to the wall boundaries. This model involves damping the lift force towards the boundaries, and sets it to zero at the proximity of particle radius.

$$C_L = \begin{cases} 0 & y/D_b < 0.5 \\ C_{L0} \left(3 \left(\frac{2y}{D_b} - 1 \right)^2 - 2 \left(\frac{2y}{D_b} - 1 \right)^3 \right) & 0.5 < y/D_b < 1 \\ C_{L0} & 1 < y/D_b \end{cases} \quad (110)$$

where C_{L0} is the nominal lift coefficient. This model is particularly relevant for predicting lift forces where the proximity to a wall boundary considerably alters the fluid dynamics around a bubble or particle.

3.1.3. Virtual Mass

When a particle moves through the fluid, it accelerates some of the surrounding fluid. The inertia of the accelerated fluid adds to the inertia of the particle. This creates an additional force termed the virtual mass force (F_{VM}).

Zuber Virtual Mass Force and Coefficient

Zuber [31] defined their virtual mass coefficient model C_{VM} as in Eq. (111)

$$C_{VM} = \frac{1}{2}(1 + 3.32\alpha) \quad (111)$$

Ishii Virtual Mass Coefficient

Ishii et al. [32] defined the Virtual mass force F_{VM} as in Eq. (112)

$$\mathbf{F}_{VM} = -C_{VM}\rho_f \left(\frac{D_g \mathbf{v}_r}{Dt} - \mathbf{v}_r \cdot \nabla \mathbf{v}_f \right) \quad (112)$$

and introduced the virtual mass coefficient C_{VM} model shown Eq.(113) with void fraction dependency for bubbly flow and additionally particle size for slug flow;

$$C_{VM} = \begin{cases} \frac{\alpha}{2} \frac{1+2\alpha}{1-\alpha} & \text{for bubbly flow} \\ 5\alpha[0.66 + 0.34(\frac{1-D_b/L_b}{1-D_b/3L_b})] & \text{for slug flow} \end{cases} \quad (113)$$

3.1.4. Turbulent Dispersion

Primary phase velocity fluctuations due to turbulence acts on the particles as the turbulent dispersion force (\mathbf{F}_{TD}). \mathbf{F}_{TD} is a non-drag force with considerable effect on the radial void fraction distribution by smoothing out local peaks. In the case of wall peaking trend, \mathbf{F}_{TD} directs the dispersed phase away from boundaries.

Lopez de Bertodano's Turbulent Dispersion Force Model

In their study, Lopez de Bertodano [33] introduced their model as shown in Eq. (114) assuming that particle dispersion in a continuous phase is analogous to molecular diffusion.

$$\mathbf{F}_{TD} = -C_{TD}\rho_f k_f \nabla \alpha \quad (114)$$

where $\nabla \alpha$ denotes the volume fraction gradient and their recommended value for the model coefficient C_{TD} , is between 0.1 and 0.5.

$$\mathbf{F}_{TD} \approx -\alpha \quad (115)$$

Lahey Turbulent Dispersion Force Model

Lahey et al. [34] studied the turbulent dispersion experimentally. Starting with the same force

model shown in Eq.(116) proposed by Lopez de Bertodano, [33] they proposed a constant $C_{TD} = 0.1$.

$$\mathbf{F}_{TD} = -C_{TD}\rho_f k_f \nabla \alpha \quad (116)$$

Drew Turbulent Dispersion Force Model

Drew [35] proposed the \mathbf{F}_{TD} model shown in Eq.(117). Their model has turbulence time scale dependencies.

$$\mathbf{F}_{TD} = -C_{TD} \frac{\tau_f}{\tau_g} k_f \nabla \alpha \quad (117)$$

where;

$$\frac{\tau_f}{\tau_g} = \frac{18\nu_f k_f}{d_b^2 \varepsilon_f} \quad (118)$$

Lucas Turbulent Dispersion Force Model and Coefficient Lucas et al. [36] introduced their turbulent dispersion force model shown in Eq.(119). Their model has bubble shape dependencies and is a function of E_o .

$$\mathbf{F}_{(tot)}^{TD} = \mathbf{F}^{TD} + \mathbf{F}_{E_o}^{TD} \quad (119)$$

$$\mathbf{F}_{E_o}^{TD} = -C_{TD}\rho_f(E_o - 1)\nabla \alpha \quad (120)$$

$$\mathbf{F}^{TD} = -0.1\rho_f k_f \nabla \alpha \quad (121)$$

They proposed the turbulent dispersion coefficient C_{TD} as in Eq.(122).

$$C_{TD} = \begin{cases} 0.0015 & E_o > 1 \\ 0 & E_o < 1 \end{cases} \quad (122)$$

Burns' Turbulent Dispersion Force Model (FAD)

Burns et al. [37] introduced the Favre-Averaged Drag (FAD) \mathbf{F}_{TD} model given in Eq. (123). Their model is correlated to the drag force.

$$\mathbf{F}_{TD} = -\frac{3 C_D}{4 D_b} \alpha |\mathbf{v}_G - \mathbf{v}_L| \frac{\mu_L^{turb}}{\sigma_{TD}} \left(\frac{1}{\alpha} + \frac{1}{1 - \alpha} \right) \nabla \alpha \quad (123)$$

3.1.5. Wall Lubrication

Depending on the flow conditions, particles may have the tendency for accumulation in wall proximity. The non-drag type wall lubrication force \mathbf{F}_{WL} typically defined in conditional functional form of the wall distance prevents accumulation of particles.

Antal Wall Lubrication Force Model and Coefficient

The dispersed phase radial distribution and near-wall localization are significantly influenced by wall lubrication forces. These forces modeled by the potential flow theory can be described as follows [38],

$$\mathbf{M}_d^{WL} = \frac{\alpha \rho_f |\mathbf{v}_r \cdot \mathbf{n}_z|^2}{r_d} \left[C_{W1} + C_{W2} \left(\frac{r_d}{y_w} \right) \right] \mathbf{n}_w \quad (124)$$

Antal et al. [38], defined their model coefficients C_{W1} and C_{W2} as;

$$C_{W1} = 0.06 |\mathbf{v}_g - \mathbf{v}_l| + 0.14 \quad (125)$$

$$C_{W2} = 0.147 \quad (126)$$

Tomiyama Wall Lubrication Force Model and Coefficient

Tomiyama et al. [39] modified the Antal et al. [38] model. Their model shown in Eq.(127) takes the bubble shape into account via the Eötvös(EO) number.

$$\mathbf{M}_{\infty}^{WL} = -C_W \frac{D_b}{2} \rho_f |\mathbf{v}_r \cdot \mathbf{n}_z|^2 \left[\frac{1}{y_W^2} - \frac{1}{(D - y_W)^2} \right] \mathbf{n}_w \quad (127)$$

They studied the wall lubrication coefficient empirically for a single bubble and proposed the values shown in Eq.(128)

$$C_W = \begin{cases} e^{0.933EO+0.179} & \text{for } 1 \leq EO \leq 5 \\ 0.007EO + 0.04 & \text{for } 5 \leq EO \leq 33 \end{cases} \quad (128)$$

Their validation conditions cover EO range 1 to 33 for the case of $M = 10^{-2.8}$.

Hosokawa Wall Lubrication Coefficient

Hosokawa et al. [40] proposed the model coefficient in Eq.(129). $10^{-2.5} < M < 10^{-6}$ and $10^{-1} < Re < 10^2$

$$C_W = \max\left(\frac{7}{Re_{\infty}^{1.9}}, 0.0217EO\right) \quad (129)$$

Their validation conditions cover $10^{-2} < EO < 10^1$ through their conducted experiment.

Krepper Wall Lubrication Coefficient

Krepper [41] proposed the model coefficient Eq.(130).

$$C_{WL} = \max\left(-C_{W1} + C_{W2} \frac{D_b}{2y}, 0\right) \quad (130)$$

where the constants C_{W1} and C_{W2} are given by:

$$C_{W1} = -0.0064 \quad (131)$$

$$C_{W2} = 0.016 \quad (132)$$

Frank Wall Lubrication Coefficient

Frank et al. [42], [43] proposed the coefficient model shown in Eq.(133) which is based on Tomiyama et al. [39] proposed model with the improvement to drop geometry dependency.

$$C_W = C_{W3}(Eo) \times \max \left[0, \frac{1}{C_{WD}} \frac{1 - y_W/C_{WC}D_b}{y_W(y_W/C_{WC}D_b)^{P-1}} \right] \quad (133)$$

where they used C_{WC} and C_{WD} as cut-off and damping coefficients respectively.

Rzehak Wall Lubrication Coefficient

Rzehak et al. [44] numerically studied the wall lubrication coefficient. They extrapolated the results of Hosokawa et al. [40], starting with Tomiyama et al. [39] coefficient model as given in Eq.(134)

$$C_{WL} = C_{W3} \left(\frac{D_b}{2y} \right)^2 \quad (134)$$

they proposed C_{W3} as;

$$C_{W3} = 0.0217Eo \quad (135)$$

Lubchenko Wall Lubrication Force Model and Coefficient

Lubchenko et al. [45] proposed a wall force model where they claim if Shaver and Podowski's [30] lift force model is used, F_{TD} is the only force remaining perpendicular to the wall thus a correction related to the bubble shape near the wall is required and has the form shown in Eq.(136);

$$\mathbf{F}_{WITD} + \mathbf{F}_{TD} = 0 \quad (136)$$

where \mathbf{F}_{WLTD} has the form shown in Eq.(137)

$$\mathbf{F}_{WLTD} = \begin{cases} \frac{3}{4} \frac{C_D}{D_b} |\mathbf{v}_{rel}| \frac{\mu_l^t}{\sigma_{TD}} \left(1 + \left(\frac{\alpha}{1-\alpha} \right) \right) \cdot \left(\alpha \frac{1}{y_W} \left(\frac{D_b - 2y_W}{D_b - y_W} \right) \right) \mathbf{n}, & y < D_b/2 \\ 0, & y > D_b/2 \end{cases} \quad (137)$$

The void fraction gradient, $\nabla\alpha$ part of Burn's \mathbf{F}_{TD} model, shown in Eq.(123) is replaced by the relation shown in Eq.(138) to take the bubble size and wall distance into account.

$$\nabla\alpha = \alpha \cdot \frac{1}{y_W} \left(\frac{D_b - 2y_W}{D_b - y_W} \right) \mathbf{n} \quad (138)$$

3.2. Single-Phase Turbulence Closure Models

3.2.1. Algebraic Models

Prandtl [46] proposed the mixing length model, which introduces a characteristic length scale over which turbulent eddies are assumed to mix properties. This model can be utilized for turbulent viscosity prediction.

Prandtl's Mixing Length Model

Analogy to molecular transport of momentum;

$$t_{xy} = \mu \frac{dU}{dy} \quad (139)$$

where,

$$\mu = \frac{1}{2} \rho u_{th} l_{mfp} \quad (140)$$

and,

$$\tau_{xy} = \frac{1}{2} u_m l_m \mu \frac{dU}{dy} \quad (141)$$

Prandtl proposed;

$$u_m = C \cdot l_m \mu \frac{dU}{dy} \quad (142)$$

The shear stress τ_{xy} is defined as:

$$\tau_{xy} = \nu_t \left(\frac{\partial U}{\partial y} \right) \quad (143)$$

where ν_t denotes the turbulent kinematic viscosity, U and y denote the velocity and the normal direction respectively.

Prandtl proposed that the turbulent viscosity could be defined as;

$$\nu_t = l_m^2 \left| \frac{\partial U}{\partial y} \right| \quad (144)$$

where l_m denotes the mixing length. The mixing length changes with respect to the wall distance.

Substituting the expression for ν_t into the shear stress equation:

$$\tau_{xy} = \rho l_m^2 \left(\frac{\partial U}{\partial y} \right) \left| \frac{\partial U}{\partial y} \right| \quad (145)$$

Van Driest's Damping Factor

Van Driest [47] introduced a damping factor to the mixing length model specifically for boundary layers. This modification accounts for the reduced turbulence near walls due to the presence of the boundary layer. The modified mixing length near proposed by Van Driest is shown below;

$$l_m = \kappa y \left(1 - e^{-y^+/A^+}\right) \quad (146)$$

where $\kappa \approx 0.41$, y , y^+ and $A^+ \approx 26$ denote the von Kármán constant, wall distance, the dimensionless wall distance and an empirical constant respectively.

Accordingly, the turbulent viscosity becomes;

$$\nu_t = (\kappa y)^2 \left(1 - e^{-y^+/A^+}\right)^2 \left| \frac{\partial U}{\partial y} \right| \quad (147)$$

and substituting this into the shear stress equation,

$$\tau = \rho(\kappa y)^2 \left(1 - e^{-y^+/A^+}\right)^2 \left(\frac{\partial U}{\partial y} \right) \left| \frac{\partial U}{\partial y} \right| \quad (148)$$

3.2.2. One-Equation Models

Prandtl's One-Equation Hypothesis

Prandtl's one-equation turbulence model introduces the concept of eddy viscosity ν_t , which is expressed with a single transport equation for the turbulent kinetic energy k as shown below:

$$\frac{\partial k}{\partial t} + U_j \frac{\partial k}{\partial x_j} = \tau_{ij} \frac{\partial U_i}{\partial x_j} - \varepsilon + \frac{\partial}{\partial x_j} \left[(\nu + \nu_t/\sigma_k) \frac{\partial k}{\partial x_j} \right] \quad (149)$$

where the dissipation term ε is related to the mixing length l with a model constant C_D ,

$$\varepsilon = C_D k^{3/2}/l \quad (150)$$

and ν_t is expressed as;

$$\nu_t = C_D k^2 / \varepsilon \quad (151)$$

3.2.3. Two-Equation Models

Standard k- ε Model

Launder and Spalding [48] developed the standard k- ε model presented below in Eq.s (152,153) with two transport equations;

$$\frac{\partial k}{\partial t} + U_j \frac{\partial k}{\partial x_j} = \tau_{ij} \frac{\partial U_i}{\partial x_j} - \varepsilon + \frac{\partial}{\partial x_j} \left[\left(\nu + \nu_t / \sigma_k \right) \frac{\partial k}{\partial x_j} \right] \quad (152)$$

for the turbulent kinetic energy (k),

$$\frac{\partial \varepsilon}{\partial t} + U_i \frac{\partial \varepsilon}{\partial x_j} = C_{\varepsilon 1} \frac{\varepsilon}{k} \tau_{ij} \frac{\partial U_i}{\partial x_j} - C_{\varepsilon 2} \frac{\varepsilon^2}{k} + \frac{\partial}{\partial x_j} \left(\nu + \frac{\nu_t}{\sigma_\varepsilon} \right) \frac{\partial \varepsilon}{\partial x_j} \quad (153)$$

and for dissipation rate (ε).

The eddy viscosity ν_t is given by:

$$\nu_t = C_\mu \frac{k^2}{\varepsilon}$$

The model coefficients are given in Table. 3.1.

C_1	C_2	σ_k	σ_ε	C_μ
1.44	1.92	1	1.272	0.09

Table 3.1 Launder and Spalding k- ε Model Coefficients

Standard k- ω Model

Saffman [49] developed the two-equation, k- ω turbulence model. This model includes turbulent kinetic energy (k) and the specific dissipation rate (ω) transport equations as shown in Eqs. (154,155) respectively.

$$\frac{\partial k}{\partial t} + U_j \frac{\partial k}{\partial x_j} = \tau_{ij} \frac{\partial U_i}{\partial x_j} - \beta^* k \omega + \frac{\partial}{\partial x_j} \left[(\nu + \sigma_k \nu_t) \frac{\partial k}{\partial x_j} \right] \quad (154)$$

$$\frac{\partial \omega}{\partial t} + U_j \frac{\partial \omega}{\partial x_j} = \alpha \frac{\omega}{k} \tau_{ij} \frac{\partial U_i}{\partial x_j} - \beta \omega^2 + \frac{\sigma_d}{\omega} \frac{\partial k}{\partial x_j} \frac{\partial \omega}{\partial x_j} + \frac{\partial}{\partial x_j} \left[(\nu + \sigma_\omega \nu_t) \frac{\partial \omega}{\partial x_j} \right] \quad (155)$$

where ν , ν_t are the dynamic and the eddy viscosity. The relation for eddy viscosity ν_t is shown below and the model constants σ_k , σ_ω , β^* , β , and α are given in Table 3.2.

$$\nu_t = \frac{k}{\omega} \quad (156)$$

σ_k	σ_ω	β^*	β	α
2.0	2.0	0.09	0.072	0.52

Table 3.2 Wilcox k- ω Model Coefficients

Menter's Shear Stress Transport (SST) Model

The SST model by Menter [50] introduces the equations for turbulent kinetic energy and specific dissipation rate, as presented in Eqs. (157,158), respectively.

$$\frac{\partial k}{\partial t} + U_i \frac{\partial k}{\partial x_i} = P_k - \beta^* k \omega + \frac{\partial}{\partial x_j} \left[(\nu + \sigma_k \nu_t) \frac{\partial k}{\partial x_j} \right] \quad (157)$$

$$\frac{\partial \omega}{\partial t} + U_i \frac{\partial \omega}{\partial x_i} = \alpha \frac{\omega}{k} P_k - \beta \omega^2 + \frac{\partial}{\partial x_j} \left[(\nu + \sigma_\omega \nu_t) \frac{\partial \omega}{\partial x_j} \right] + (1 - F_1) \frac{2\rho\sigma_{\omega 2}}{\omega} \frac{\partial k}{\partial x_j} \frac{\partial \omega}{\partial x_j} \quad (158)$$

where α and β are model constants, σ_ω is the turbulent Prandtl number, and F_1 is a blending function.

here turbulent viscosity is defined as;

$$\nu_t = \frac{a_1 k}{\max(a_1 \omega, S F_2)} \quad (159)$$

where the second blending function F_2 is introduced alongside the model constants S and a_1 .

Transition between the $k - \omega$ and $k - \varepsilon$ models are achieved by the blending functions F_1 and F_2 shown below;

$$F_1 = \tanh \left(\left(\min \left[\max \left(\frac{\sqrt{k}}{\beta^* \omega y}, \frac{500\nu}{y^2 \omega} \right), \frac{4\sigma_{\omega 2} k}{C D_k \omega y^2} \right] \right)^4 \right) \quad (160)$$

$$F_2 = \tanh \left(\left(\max \left(\frac{2\sqrt{k}}{\beta^* \omega y}, \frac{500\nu}{y^2 \omega} \right) \right)^2 \right) \quad (161)$$

where y is the wall distance and $C D_k$ is a cross-diffusion term. The closure coefficients are given in Table 3.3.

σ_k	σ_{ω}	$beta^*$	β	α	α_1
1.0	1.168	0.09	0.072	0.31	0.31

Table 3.3 Menter $k-\omega$ Model Coefficients

3.2.4. Reynolds Stress Model (RSM)

The RSM equation for incompressible flow is given in Eq. (46)

Algebraic RSM

Rodi [51] introduced the non-linear eddy viscosity model;

$$\frac{\partial \tau_{ij}}{\partial t} + U_k \frac{\partial \tau_{ij}}{\partial x_k} - \frac{\partial}{\partial x_k} \left(\nu \frac{\partial \tau_{ij}}{\partial x_k} + C_{ijk} \right) \approx \frac{\tau_{ij}}{k} \left(\frac{\partial k}{\partial t} + U_k \frac{\partial k}{\partial x_k} - \frac{\partial}{\partial x_k} \left(\nu \frac{\partial k}{\partial x_k} + \frac{1}{2} C_{ijk} \right) \right) \quad (162)$$

$$\frac{\tau_{ij}}{k} \left(\tau_{mn} \frac{\partial U_m}{\partial x_n} - \epsilon \right) = -\tau_{ik} \frac{\partial U_j}{\partial x_k} - \tau_{jk} \frac{\partial U_i}{\partial x_k} + \epsilon_{ij} - \Pi_{ij} \quad (163)$$

Pope [52] and Rodi [51] introduced the algebraic RSM model derived from simplified versions of the Reynolds stress transport equations where R_{ij} is approximated as;

$$R_{ij} = \frac{\nu_t}{2S} \left(\frac{\partial U_i}{\partial x_j} + \frac{\partial U_j}{\partial x_i} \right) \quad (164)$$

and S is a scalar representing the strain rate relation.

Turbulent viscosity is expressed with a model constant C_μ as;

$$\nu_t = C_\mu \frac{k^2}{\epsilon} \quad (165)$$

Reynolds stress tensor is re-written as;

$$R_{ij} = C_\mu \frac{k^2}{2S\epsilon} \left(\frac{\partial U_i}{\partial x_j} + \frac{\partial U_j}{\partial x_i} \right) \quad (166)$$

Differential RSM

Launder et al. [53] developed differential RSM (DRSMs), which solve transport equations for each component of the Reynolds stress tensor.

3.3. Two-Phase Turbulence Closure Models

Bubble-Induced Turbulence (BIT) Models

The existence of bubbles significantly alters the liquid phase turbulence characteristics. BIT models address the change in turbulence generation due to bubbles. The turbulent viscosity in BIT models is often represented as;

$$\nu_t = \nu_{t,SI} + \nu_{t,BI} \quad (167)$$

where $\nu_{t,SI}$ denote the shear-induced and $\nu_{t,BI}$ denote the bubble-induced viscosity.

3.3.1. Algebraic Models

Sato and Sekoguchi

Sato and Sekoguchi [54] proposed an algebraic model for BIT as shown below where they consider a linear combination of BIT with the shear induced turbulence (SIT) through the viscosity.

$$\nu_{t,BI} = C_{la} \alpha d_b u_r \quad (168)$$

where C_{la} is an empirical constant for which Sato et al. [55] proposed the constant value of 0.6.

Michiyoshi and Serizawa

Michiyoshi and Serizawa [56] applied the Van Driest damping factor and extended the algebraic BIT model to wall-bounded flows.

$$\nu_{t,BI} = \begin{cases} C_{la1} \alpha la1 u_r D(y^+) & \text{for } y > d_b \\ C_{la2} \alpha la2 u_r D(y^+) & \text{for } y^* < y < d_b \end{cases} \quad (169)$$

where C_{la1} and C_{la2} are model coefficients, $la1$ and $la2$ are the length scales, y is the wall distance and y^* is the minimum clearance between the wall and the bubble, defined as 20 μm .

Kataoka et al.

Kataoka et al. [57] defined the effective viscosity, (ν_t) as;

$$\nu_t = C_{\mu\alpha} l \sqrt{k_1} \quad (170)$$

and defined the length scale l as;

$$l = l_{SI} + l_{BI} \quad (171)$$

where;

$$l_{SI} = 0.4y \quad , \quad l_{BI} = \frac{1}{3} \alpha d_b \quad (172)$$

and,

$$k_1 = \frac{3}{4} \frac{\alpha C_D l / D_b}{0.04 \alpha_l + \alpha l / D_b} |u_r^2| \quad (173)$$

where C_D dependency is introduced.

3.3.2. One-Equation Models

One-equation two-phase turbulence models typically solve only the turbulent kinetic energy equation.

Kataoka and Serizawa

In their work, Kataoka and Serizawa [58] proposed the below equation for turbulent kinetic energy.

$$\alpha \left(\frac{\partial k_l}{\partial t} + U_j \frac{\partial k_l}{\partial x_j} \right) = \frac{\partial}{\partial x_j} \left(\alpha \mu_t \frac{\partial k_l}{\partial x_j} \right) + \alpha (P - \varepsilon_l) + S_{k_{li}} \quad (174)$$

where P_k and $S_{k_{li}}$ are the production and source terms rising from interfacial transfer.

$$S_{k_{li}} = M_{li}^D u_r \quad (175)$$

$$l_{SI} = 0.4yD(y^+) \quad (176)$$

$$l_{BI} = \begin{cases} \frac{1}{3}\alpha l_{a1} & \text{for } \frac{3}{2}d_b \leq yR \\ \frac{1}{6}\alpha l_{a2} & \text{for } d_b \leq yy \leq y\frac{3}{2}d_b \\ \frac{1}{6}\alpha l_{a3} & \text{for } 0 \leq y \leq d_b \end{cases} \quad (177)$$

3.3.3. Two-Equation Models

While the form of the two-phase models are similar to the single phase counterparts, additional source terms are included for the respective equations.

Elghobashi and Abou-Arab

Elghobashi and Abou-Arab [59] proposed the two-phase $k - \varepsilon$ model by introducing additional source terms to represent the dispersed phase effect on continuous phase turbulence.

Turbulent kinetic energy (k) equation;

$$\alpha \left(\frac{\partial k_1}{\partial t} + U_j \frac{\partial k_1}{\partial x_j} \right) = \frac{\partial}{\partial x_j} \left(\alpha \mu_t \frac{\partial k_1}{\partial x_j} \right) + \alpha (P - \varepsilon_1) + S_{ki} \quad (178)$$

where S_k denotes the source term due to the dispersed phase.

Dissipation rate (ε) equation;

$$\alpha \left(\frac{\partial \varepsilon_1}{\partial t} + U_j \frac{\partial \varepsilon_1}{\partial x_j} \right) = \frac{\partial}{\partial x_j} \left(a_1 \frac{\mu_t}{\sigma_\varepsilon} \frac{\partial \varepsilon_1}{\partial x_j} \right) + \alpha \frac{\varepsilon_1}{k_1} (C_{\varepsilon 1} P_{SI} - C_{\varepsilon 2} \varepsilon_1) + S_{\varepsilon i} \quad (179)$$

where S_ε is the respective source term.

Kataoka and Serizawa

Kataoka and Serizawa [60] developed a $k - \varepsilon$ model for two-phase flows, emphasizing the effects of bubble-induced turbulence.

Turbulent kinetic energy equation;

$$\frac{\partial k}{\partial t} + U_j \frac{\partial k}{\partial x_j} = P_k - \varepsilon + P_b \quad (180)$$

where P_b is the turbulence production due to bubbles.

Dissipation rate equation;

$$\frac{\partial \varepsilon}{\partial t} + U_j \frac{\partial \varepsilon}{\partial x_j} = C_{\varepsilon 1} \frac{\varepsilon}{k} P_k - C_{\varepsilon 2} \frac{\varepsilon^2}{k} + P_{\varepsilon b} \quad (181)$$

where $P_{\varepsilon b}$ is the bubble-induced dissipation rate.

Lopez de Bertodano et al.

Lopez de Bertodano et al. [61] developed a two-phase $k - \varepsilon$ model, focusing on the effects of interfacial forces and turbulence modulation by the dispersed phase.

Turbulent kinetic energy (k) equation;

$$\frac{\partial k}{\partial t} + U_j \frac{\partial k}{\partial x_j} = P_k - \varepsilon + S_k^{int} \quad (182)$$

where S_k^{int} represents the source term due to interfacial forces.

Dissipation rate (ε) equation;

$$\frac{\partial \varepsilon}{\partial t} + U_j \frac{\partial \varepsilon}{\partial x_j} = C_{\varepsilon 1} \frac{\varepsilon}{k} P_k - C_{\varepsilon 2} \frac{\varepsilon^2}{k} + S_{\varepsilon}^{int} \quad (183)$$

where S_{ε}^{int} is the dissipation rate source term due to interfacial forces.

Troshko and Hassan

Troshko and Hassan [62] introduced the two-phase $k - \varepsilon$ model,

Turbulent kinetic energy (k) equation;

$$\begin{aligned} \frac{\partial(\rho_c \alpha_c k_c)}{\partial t} + \nabla \cdot (\rho_c \alpha_c \mathbf{U}_c k_c) &= \alpha_c \mathbf{T}_c^{Re} : (\nabla \mathbf{U}_c) - \nabla \cdot \left(\frac{\rho_c \mathcal{V}_c^t}{\sigma_k} \nabla k_c \right) \\ &- \rho_c \alpha_c \varepsilon_c + \frac{3}{4} \frac{C_d}{d} \alpha_d \rho_c |U_r|^3 \end{aligned} \quad (184)$$

smallest eddy frequency scale [48];

$$\omega = \frac{\varepsilon}{k} \quad (185)$$

bubble dissipation frequency from bubble relaxation time constant τ_b proposed by Bertodano [61];

$$\omega_b = (\tau_b)^{-1} = \left(\frac{2 C_{vm}}{3 C_D} \frac{D_b}{u_r} \right)^{-1} \quad (186)$$

Dissipation rate (ε) equation;

$$\begin{aligned} \frac{\partial(\rho_c \alpha_c \varepsilon_c)}{\partial t} + \nabla \cdot (\rho_c \alpha_c \mathbf{U}_c \varepsilon_c) = & \omega (C_1 \alpha_c \mathbf{T}_c^{Re} : (\nabla \mathbf{U}_c) - C_2 \rho_c \alpha_c \varepsilon_c) \\ & - \nabla \cdot \left(\frac{\rho_c \nu_c^t}{\sigma_\varepsilon} \nabla \varepsilon_c \right) + \omega_b C_3 \frac{3 C_d}{4 d} \alpha_d \rho_c |U_r|^3 \end{aligned} \quad (187)$$

where C_3 and C_ω are the new model constant, and . The remaining model constants are taken from the standard k- ε model as shown in Table 3.1

Fig.s (3.1-3.3) illustrate the use of Troshko and Hassan model with different turbulence models.

Politano et al.

Politano et al. [63] introduced the two-phase $k - \varepsilon$ model,

Turbulent Kinetic Energy (k) Equation;

$$\alpha_c \frac{dk}{dt} + \alpha_c \mathbf{U}_c \nabla k = \nabla \cdot (\alpha_c \nu^t \nabla k) + P_1 \quad (188)$$

$$- \alpha_c C_{\varepsilon 2} + \alpha_c \phi_k k \quad (189)$$

Dissipation Rate (ε) Equation;

$$\alpha_c \frac{d\varepsilon}{dt} + \alpha_c \mathbf{U}_c \nabla \varepsilon = \nabla \cdot \left(\frac{\nu^t}{\sigma_\varepsilon} \nabla \varepsilon \right) + C_{\varepsilon 1} P_1 \frac{\varepsilon}{k} \quad (190)$$

$$- \alpha_c C_{\varepsilon 2} \frac{\varepsilon^2}{k} + \alpha_c \phi_k C_{\varepsilon 2} \frac{\varepsilon}{k} \quad (191)$$

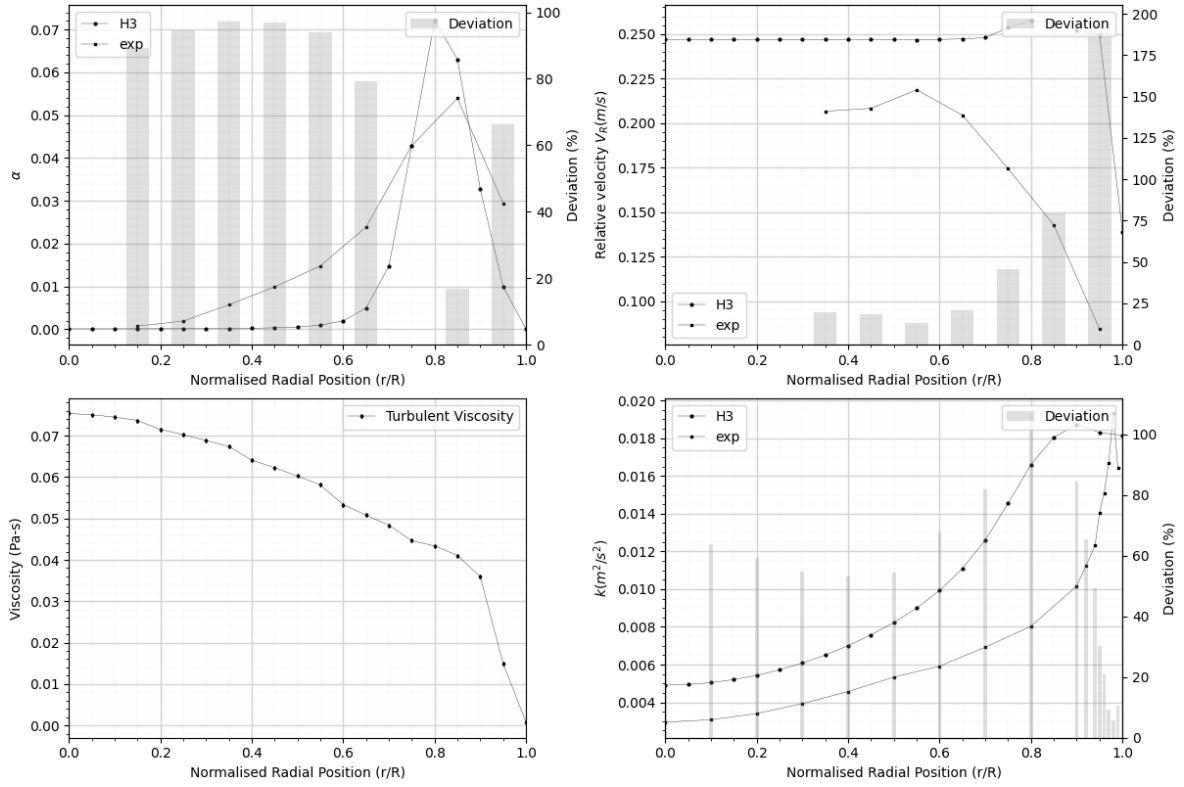


Figure 3.1 Standard k- ϵ with Troshko-Hassan model

where $C_{\epsilon 1}$ and $C_{\epsilon 2}$ are model constants, and ϕ_k is the source term due to the dispersed phase.

where the production term is defined as;

$$P_1 = \alpha_c \nu^t (\nabla \mathbf{U}_c + \nabla \mathbf{U}_c^T) : \nabla \mathbf{U}_c \quad (192)$$

and the source term is defined for a multigroup dispersed phase condition as proposed by Lee et al. [64],

$$\phi_k = C_p \sum_{g=1}^N \frac{\alpha_g |\mathbf{U}_r|^3}{2r_g} \quad (193)$$

and the turbulent viscosity is defined as;

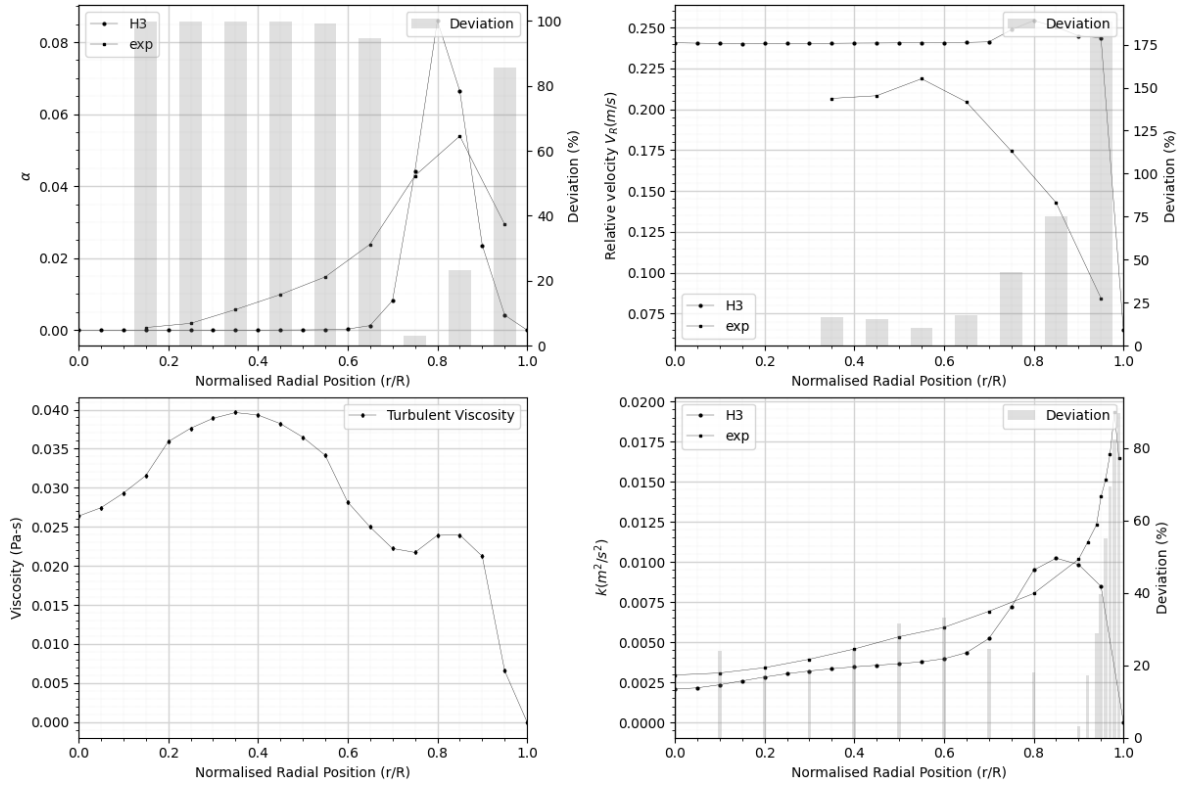


Figure 3.2 Standard $k-\omega$ with Troshko-Hassan model

$$\nu^t = C_\mu \frac{k^2}{\varepsilon} \quad (194)$$

where the model constant C_p is taken 1 and the rest of the model constants are used as proposed by Launder and Spalding [48] as shown in Table 3.1

3.3.4. Reynolds Stress Model (RSM)

Kumar et al.

Kumar [65] proposed an algebraic RSM starting with the bubble induced expression for ν_t as;

$$\nu_{t,BI} = C_\mu \frac{k^2}{\varepsilon} + C_{la} \alpha d_b u_r \quad (195)$$

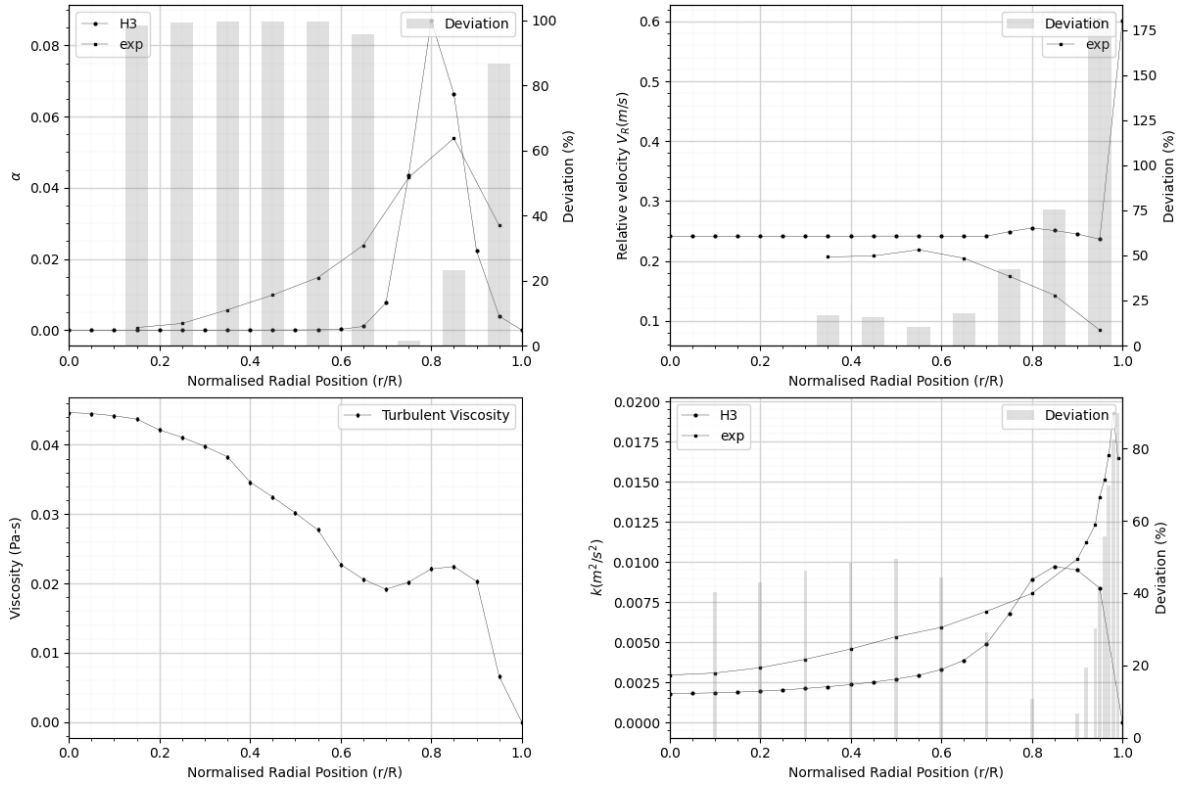


Figure 3.3 SST $k-\omega$ with Troshko-Hassan model

Fig (3.4) illustrate the use of the algebraic RSM model for a test case.

Lopez de Bertodano et al.

Lopez de Bertodano et al. [66] developed a differential RSM. using Lee et al. [64]

Launder et al. [53] developed differential RSM (DRSM), which solve transport equations for each component of the R_{ij} , providing a more detailed representation of turbulence.

The Reynolds stress transport equation is:

$$\alpha_c \frac{D}{Dt} \overline{u'u'} = \alpha_c (\nabla \cdot D_{SI} + P_{SI}) + \varphi_{SI} - 2I\varepsilon_c + P_i \quad (196)$$

where: D_{SI} is the diffusion term, P_{SI} is the production term, φ_{SI} is the pressure-strain term, P_i is the bubble induced production term.

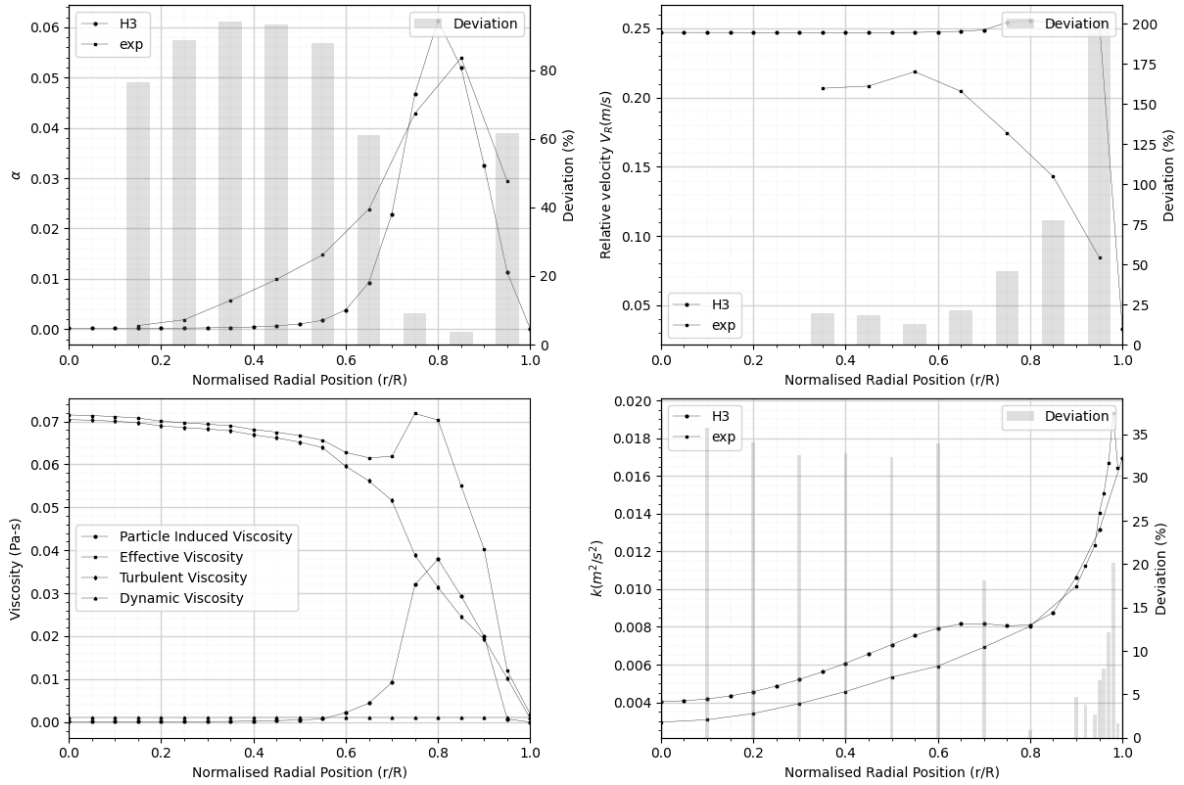


Figure 3.4 Algebraic RSM with Sato viscosity model

The diffusion term is:

$$D_{SI} = \frac{\partial}{\partial x_k} \left(\nu \frac{\partial R_{ij}}{\partial x_k} \right) \quad (197)$$

Turbulent Diffusion Term (D_{ij});

$$D_{SI} = -\frac{\partial}{\partial x_k} \left(\overline{u'_i u'_j u'_k} + \frac{\overline{p' u'_i} \delta_{jk} + \overline{p' u'_j} \delta_{ik}}{\rho} - 2\nu \frac{\partial \overline{u'_i u'_j}}{\partial x_k} \right) \quad (198)$$

The production term is given by:

$$P_{SI} = -R_{ik} \frac{\partial U_j}{\partial x_k} - R_{jk} \frac{\partial U_i}{\partial x_k} \quad (199)$$

The pressure-strain term is:

$$\varphi_{SI} = -\frac{1}{\rho} \left(\overline{p' \frac{\partial u'_i}{\partial x_j}} + \overline{p' \frac{\partial u'_j}{\partial x_i}} \right) \quad (200)$$

The dissipation term is:

$$\varepsilon_c = \frac{2}{3} \varepsilon \delta_{ij} \quad (201)$$

and the dissipation rate equation is in the same form as the one given in Eq.(153)

The bubble induced production term is given by:

$$P_{BI} = \begin{bmatrix} 4/5 & 0 & 0 \\ 0 & 3/5 & 0 \\ 0 & 0 & 3/5 \end{bmatrix} S_{ki} \quad (202)$$

where;

$$S_{ki} = C_i M_{2i}^D \cdot \mathbf{U}_r \quad (203)$$

with the model constant C_i

Fig.s (3.5-3.6) illustrate the effect of DRSM model constant C_i .

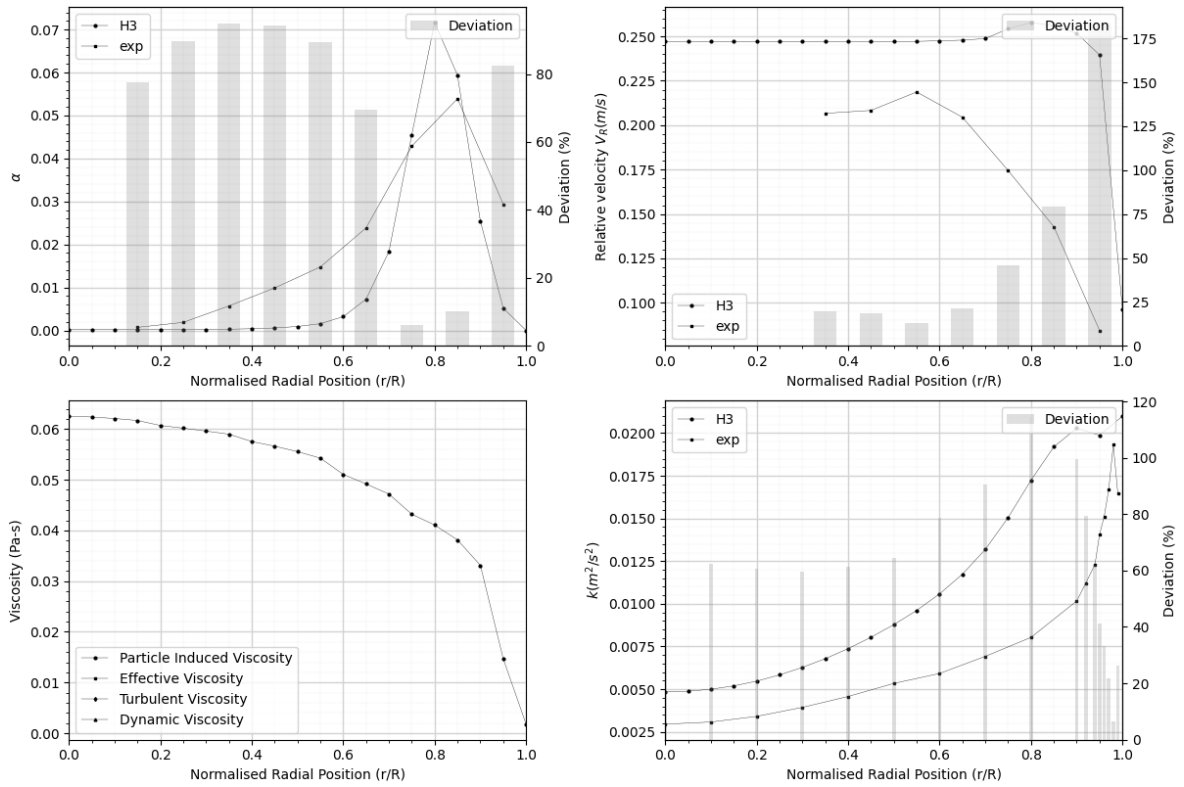


Figure 3.5 Differential RSM model ($C_i = 0.25$)

3.4. Review of Experiments

This literature review focuses on two-phase flow database source experiments, which are critical for developing new momentum closure models and validating existing ones. A broad range of scenarios are listed for various flow conditions across different flow domains such as, but not limited to, bubble columns, circular and rectangular even triangular ducts aligned vertically or horizontally. “The growth of the experiment database over the years is clearly seen; however, Hibiki et al. [1] note in their investigation and review that further systematic experimental efforts are essential to establish solid experimental databases for benchmarking the interfacial area transport equations and both 1D and 3D thermo-fluid dynamic codes.”

In the context of this study, the experiments of interest are iso-thermal and bubbly upward flow in cylindrical pipes, primarily due to its compatibility with 2-D axisymmetric modeling. “The list of experiments of this category is filtered from the review of Hibiki et al. [1] and is listed in Table 3.4”

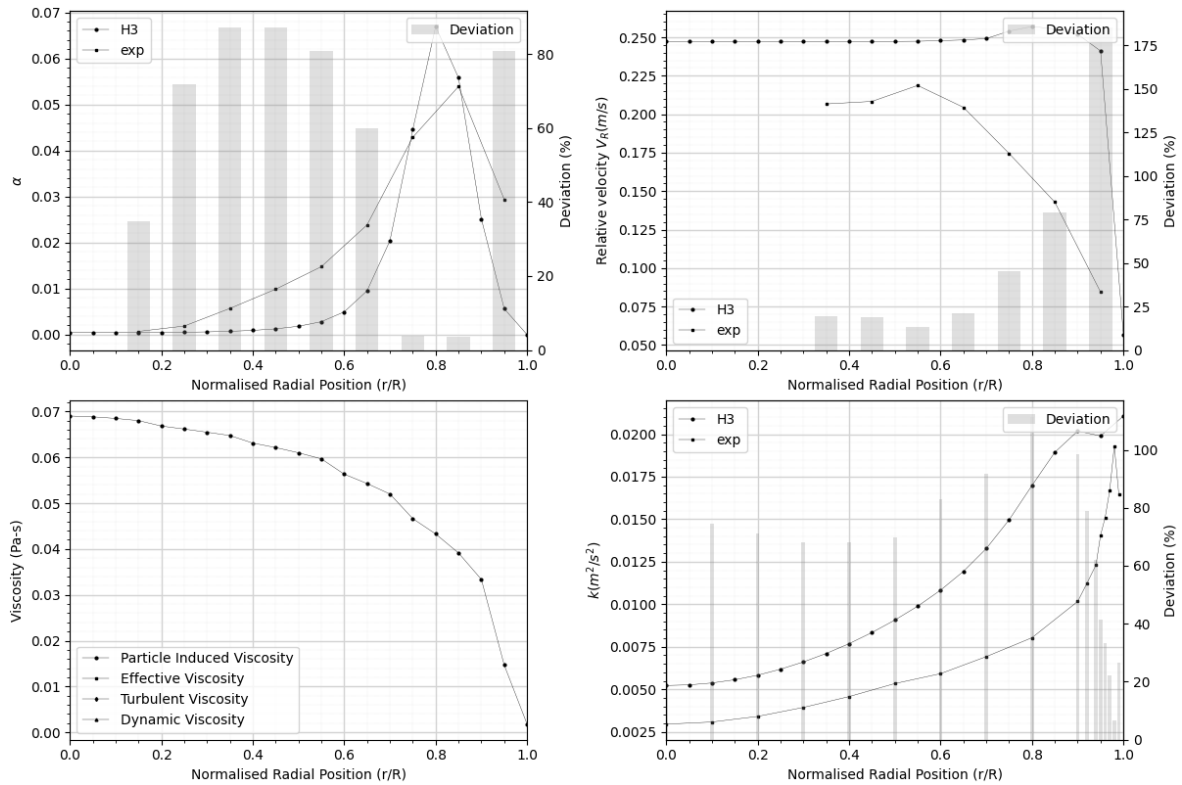


Figure 3.6 Differential RSM model ($C_i = 0.02$)

The availability of the databases mentioned is limited, as investigated and reported by the valuable study of Sari et al. [67]. It is a common exercise for the researchers to digitalize and utilize the related data from referring studies.

Serizawa Experiments

Accessible databases include, the investigations conducted by Serizawa et al. [68] for vertical upwards flow of continuous phase with different dispersed phase fluxes in cylindrical pipes. Two different configurations are for pipe diameters $D = 30$ and 60 mm. Measurement stations are at $L/D = 83$.

Investigators	D_i (mm)	z/D	j_g (m/s)	j_f (m/s)
Serizawa et al. (1991)	30.0	83	0.018-0.54	0.5-5.0
Kaklach-Navarro et al. (1993)	38.1	50	0.0562-0.332	0.3-1.25
Liu and Bankoff (1993)	57.2	30-120	0.1-0.4	0.5-3.0
Leung et al. (1995)	50.8	8-60	0.0192-0.0965	0.1-1.0
Grossetete (1995)	38.1	155	0.0895-0.181	0.877-1.75
Hibiki and Ishii (1998)	50.8	2-62	0.0147-0.0790	0.6-1.3
Hibiki and Ishii (1999)	25.4	125	0.0566-1.27	0.262-3.49
Ohnuki and Akimoto (2000)	20	12-112	0.03-4.7	0.06-1.06
Kim et al. (2001)	50.8	32-64	0.0358-4.87	0.491-5.00
Hibiki and Ishii (2001)	50.8	54	0.0358-4.87	0.491-5.00
Shoukri et al. (2003)	200	43	2.0-10.0	0.0-40.0
Prasser (2007)	195.3	2-40	0.0094-0.53	1.02
Manera et al. (2009)	25.4	13.0-133.0	0.036-2.089	0.647-2.554
Manera et al. (2009)	50.8	7.0-67.0	0.036-2.089	0.647-2.554
Chiva et al. (2010)	52	6.0-52.0	-	0.941-0.981
Xing et al. (2013)	50	20	0.002-0.037	0.072-0.569

Table 3.4 “Filtered list of two-phase flows experiments from Hibiki et al. [1]”

Liu and Bankoff Experiments

Liu and Bankoff [69] studied vertical upward flow of continuous phase with varying dispersed phase mass fluxes in circular pipe with diameter $D = 38$ mm. Measurement station is located at $L/D = 38$. Void fraction, phase velocities, bubble size and turbulence intensity distributions are reported. The conducted experiments include only for wall peaking profiles.

Hibiki Experiments

Hibiki et al. [70], [71] conducted experiments in circular pipes. The setup is upward flow. The pipe diameters are 25.4 mm and 50.8 mm. Their extensive database provides Dispersed phase volume fraction profile, primary phase turbulence intensity and phase velocities. Since this experiment investigates poly-dispersed scenarios, interfacial area concentration data is also provided.

Liu Experiments

Apart from the list presented in Table 3.4 Liu, conducted experiments with varying, bubble size and water and air mass fluxes. The experiments were on bubbly upward flow in a circular pipe sized $D = 57.2$ mm and the measurement station is at $L/D = 60$. Dispersed phase volume fraction, bubble diameter, phase velocities alongside primary phase turbulence intensity are reported.

Hosokawa Experiments

Hosokawa and Tomiyama [72] conducted experiments on bubbly upward flow. The pipe is sized 25 mm in diameter and the measurement station is at $L/D = 68$. Measurement data for dispersed phase volume fraction, phase velocities, and primary phase turbulence kinetic energy are provided. Their experiments cover both wall peak and core peak cases.

Shawkat Experiments

Shawkat et al. [73] has the experiment set up with cylindrical pipe dimension $D = 200$ mm. and the measurement station is at the location $L/D = 42$ of a 9.56 m long cylindrical pipe. Their experiments include wall and core peaking cases. They provide experiment data for continuous phase turbulent kinetic energy. Continuous and dispersed phase superficial velocities span the range 0.2 – 0.68 m/s and 0.005 – 0.18 m/s respectively. Void fraction and bubble diameter range is between 1.2 - 15.4 % and 3 - 6 mm. respectively.

MTLoop Experiments

The MTLoop facility described by Lucas et al. [74] has the experiment set up with cylindrical pipe dimension $D = 51.2$ mm. and the measurement station is at the location $L/D = 60$. Their extensive database provides dispersed phase volume fraction, velocity and diameter data for the investigated continuous and dispersed volumetric flux cases.

3.5. Review of Simulations

Researchers conducting CFD simulations have a variety of momentum closure model sets to choose from. An extensive review study by Irfan Khan et al. [2] presents a comprehensive list of the conducted CFD analysis for bubbly two-phase flow cases. The list consists of various methods for multiphase and turbulence modeling. While many researchers prefer RANS, it is seen that there are cases where LES and DNS is also applied. Additionally, Euler-Lagrangian and Euler-Euler TFM models are both used by the researchers for different cases. Filtering this list to the studies with Euler-Euler Two Fluid and RANS model approaches yields the list in “Table 3.5 adapted from Irfan Khan et al. [2] summarizing different closure model sets preferred by fellow researchers for similar CFD studies of bubbly two-phase flow.”

Researcher	Drag Force	Lift Force	Turbulent Dispersion Force	Wall Lubrication Force	Virtual Mass
Ziegenhein and Lucas (2019)	Tomiyama	Ziegenhein	FAD	Hosokawa	0.5
Colombo and Fairweather (2019)	Tomiyama (modified Eo)	Tomiyama	FAD	Antal	-
Jin et al. (2019)	Grace/Ishii and Zuber	Saffman/Mei and Klausner	FAD	Antal/Tomiyama	-
Chen et al. (2019b)	Tomiyama/Simonnet	Legendre and Magnaudet/Tomiyama	-	Hosokawa/Frank	-
Liao et al. (2019)	Ishii and Zuber	Moraga	Lopez de Bertodano	-	-
Kim and Park (2019)	Ishii and Zuber	Tomiyama	FAD	Hosokawa	0.5
Krepper et al. (2018)	Tomiyama	Tomiyama	Lahey	Frank	-
Parekh and Rzehak (2018)	Ishii and Zuber	Tomiyama/Hosokawa	FAD	Rzehak	0.5
Liao et al. (2018)	Ishii and Zuber	Tomiyama	FAD	-	0.5
Feng and Bolotnov (2018)	Feng and Bolotnov	Tomiyama	-	Hosokawa	-
Chinak et al. (2018)	Loth	Tomiyama	0.1	Hosokawa	-
Marfaing et al. (2018)	Ishii and Zuber/Tomiyama	Tomiyama/Shaver	Podowski Lavié ville/ Burns	Antal	0.5
Shi and Rzehak (2018)	Ishii and Zuber	Tomiyama	FAD	Tomiyama/ Lubchenko	-
Sugrue et al. (2017)	Tomiyama	0.025	FAD	Hosokawa	0.5
Rzehak et al. (2017)	Tomiyama	Tomiyama	FAD	Shaver and Podowski	-
Mimouni et al. (2017)	Ishii and Zuber	Tomiyama	FAD	Hosokawa	0.5
Kriebitzsch and Rzehak (2016)	Ishii and Zuber	Tomiyama	Lavieville	Tomiyama	Zuber
Pakhomov and Terekhov (2016)	Loth	Tomiyama	FAD	Hosokawa	-
Yamoah et al. (2015)	Grace	Tomiyama	Lahey(0.1)	Tomiyama	0.5
Ziegenhein et al.(2015)	Tomiyama	Tomiyama	FAD	Antal	-
Guan et al. (2015)	Ishii and Zuber	Tomiyama	FAD	Hosokawa	0.5
Ma et al. (2015)	Tomiyama	Tomiyama	FAD	Hosokawa	-
Lau et al. (2014)	Roghair	Tomiyama	-	Hosokawa	-
Masood and Delgado (2014)	Ishii and Zuber	Tomiyama	0.3	Tomiyama	0.5
Rzehak and Krepper (2013)	Tomiyama	Tomiyama	FAD	Antal	-
Mohd. Akbar et al. (2013)	Tomiyama	Tomiyama	Lopez de Bertodano	-	0.5
Rzehak et al. (2012)	Ishii and Zuber	Tomiyama	FAD	Tomiyama/Hosokawa/Antal	-
Duan et al. (2011)	Zuber	Tomiyama	FAD	Antal	-
Xiang et al. (2011)	Ishii and Zuber	Tomiyama	FAD	Antal	-
Wang and Sun (2010)	Tomiyama	Tomiyama	0.1	Antal	-
Li et al. (2009)	Grace	Tomiyama	FAD	Antal	0.5
Darmana et al. (2009)	Tomiyama	Tomiyama	Tomiyama	-	0.5
Dhotre et al. (2008)	Ishii and Zuber	Auton (0.5)	0.2	-	0.5
Ekambara et al. (2008)	Ishii and Zuber	-0.2	0.5	Antal	-

Table 3.5 “Adapted List of closure model sets used in recent CFD studies from Irfan Khan et al. [2]”

The most preferred drag force coefficients are Ishii and Zuber [18] and Tomiyama [19] models. Simonnet’s [75] model is preferred as a correction model for drag in specific applicable cases. Regarding the lift models, Tomiyama [28] is the most preferred, although it often necessitates progressive under-relaxation for stable simulations. Alongside Tomiyama’s model, the drag correlated lift correction model is also frequently used. The

Podowski [30] lift correction is commonly implemented as well. For modeling the turbulent dispersion force, the correlation-based FAD [37] is the most preferred. It is also seen that some researchers omit the use of this model. Antal [38] and Hosokawa [40] wall lubrication models are the most preferred models, while some researchers omitted their use. The virtual mass model is either used with a constant coefficient or omitted, however, when bubble induced turbulence is considered, Troshko and Hassan [62] model requires this coefficient even if force is not calculated and used.

It is interesting to see that many combinations are utilized and even in the case of using specific coefficients as constants, they vary in sign and magnitude. Also it should be noted that most of the models do have model coefficients and the researcher do modify these coefficients manually per cases. Even with a particular model set selection, the turbulence modeling has direct effect on simulation outcomes considering direct interaction through dependent variables.

4. METHODOLOGY

This section outlines the approach employed and the method implemented in this study, focusing on CFD simulations for modeling momentum transfer mechanisms in two-phase flow. The approach for selecting and configuring closure models, and assessment against experimental data, is detailed. The method for the development of new and improvement of existing closure models with design space exploration approach in an automated fashion is introduced.

Since most of the closure models have tunable parameters, these parameters can be defined as variables and since the effectiveness of these closure models are benchmarked against experiment data, the deviation of the results of the simulations conducted with these models can be defined as responses. The complex structure of multiphase simulations rises quite a few number of tunable parameters that can be specified as variables in this method, not only for closure models but also for other models such as turbulence so the description of variables and responses are not limited.

The effectiveness of closure models, or more precisely, the entire set of selected models for simulations, can be measured by the relative error against experimental data. The focus is on minimizing the relative error during the development and tuning of the available models.

General applicability is desired for the closure models to cover a broad spectrum of conditions. The reviewed experiments demonstrate a considerable amount of experimental data available for model testing. Repetitive simulations during the testing phase may rise issues. Automating these repetitive tasks reduces the required effort and eliminates potential errors inherent in manual processes.

This is an optimization problem with a high-dimensional solution space. Optimization techniques may align with the challenges and requirements of developing and testing closure models for two-phase flow CFD simulations.

In multi-objective optimization scenarios, such as those encountered in CFD simulations for two-phase flow, the challenges include managing trade-offs between conflicting objectives. A hybrid, adaptive, and efficient search algorithm is required for this research, to ensure effective design space exploration.

4.1. Design Space Exploration

The SHERPA algorithm offered with the commercial process automation and design space exploration software HEEDS-MDO is a hybrid and adaptive search algorithm. This algorithm is capable of combining multiple search strategies and adapts while the learning about the design space progresses and is capable of handling both, single objective and multi-objective studies. SHERPA algorithm is a hybrid algorithm combining global search strategies, which explores the design space broadly, with local search strategies, which refine solutions in promising regions. This is critical for finding globally optimal solutions in complex optimization problems since algorithms with local only capabilities requires a narrower search space.

There are two options for multi-objective studies. The first one is the weighted sum of all objectives type where all objectives are taken into account and the provided solutions are based on a performance function defined as;

$$P = \sum_{i=1}^{N_{\text{obj}}} \left(\frac{W_{\text{lin},i} \cdot S_i \cdot O_i}{N_{\text{obj},i}} + \frac{W_{\text{quad},i} \cdot S_i \cdot O_i^2}{N_{\text{obj},i}^2} \right) - \sum_{j=1}^{N_{\text{con}}} \left(\frac{W_{\text{lin},j} \cdot C_j \cdot O_i}{N_{\text{con},j}} + \frac{W_{\text{quad},j} \cdot C_j^2 \cdot O_i}{N_{\text{con},j}^2} \right) \quad (204)$$

where: N_{obj} is the number of objectives in the design study. $W_{\text{lin},i}$ and $W_{\text{quad},i}$ are the linear and quadratic weights for the i^{th} objective, respectively. S_i is the sign for the i^{th} objective. O_i is the response value for the i^{th} objective. $N_{\text{obj},i}$ is the normalization value for the i^{th} objective. N_{con} is the number of constraints in the design study. $W_{\text{lin},j}$ and $W_{\text{quad},j}$ are the linear and quadratic weights for the j^{th} constraint, respectively. C_j is the amount by which the

j^{th} constraint is violated. $N_{\text{con},j}$ is the normalization value for the j^{th} constraint. Depending on the type of objective, S_i is set to -1 for minimization and 1 for maximization.

The performance function, P , is a weighted sum of all the objectives and constraints in a design study. It allows for optimization based on a single objective or multiple objectives. When multiple objectives are defined, linear weighting is used to convert all objectives into a single objective. Running this analysis with multiple objectives returns a single best design.

A typical performance history plot for a study is shown in Fig. 4.1. There are three categories namely, feasible, infeasible and error designs. Baseline design is the first design and regarding the study type, it can be a member of any of the categories. If the study is set as an exploration with the performance function referencing the baseline for normalization $N_{\text{obj},i}$, that is an improvement type of study, the baseline design must be a member of the feasible designs. On the other hand, if the procedure as defined as an exploration without any reference where $N_{\text{obj},i}$ can be set to any value, in that case the baseline design can be a member of any of the categories.

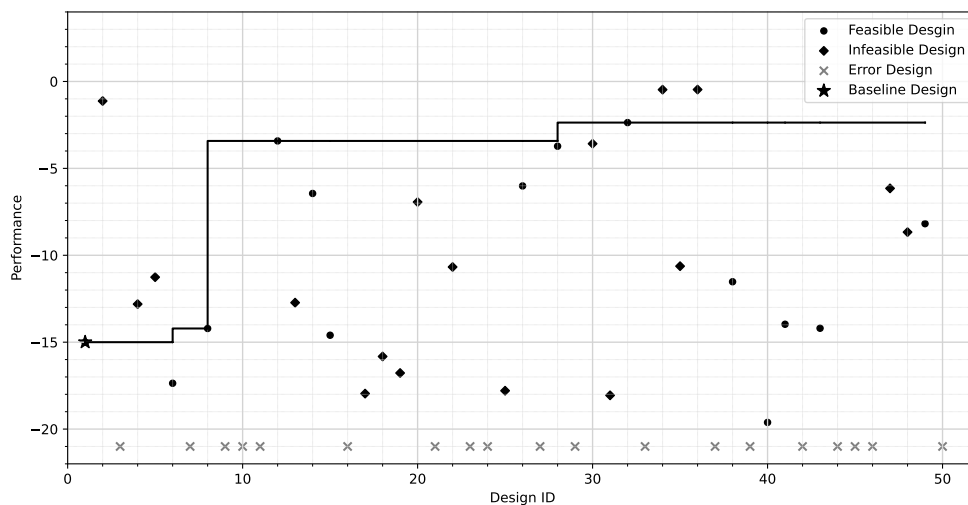


Figure 4.1 Performance history plot

The second option is the multiple objective trade-off study also called Pareto optimization is suitable when there are conflicting objectives. It works in the same principal as the weighted

sum of all objectives option, but offers handling of multiple objectives independently resulting in a set of solutions. Each solution is considered best in a specific aspect for one of the objectives. This option is preferred for optimization studies where the trade-offs are important. Pareto optimization study does not provide a single optimum design, instead results in a curve. This curve is the Pareto front. Pareto front is used to identify the trade-off relationships of competing objectives.

SHERPA is an iterative algorithm which allows continuous refinement of solutions. Starting with a broad exploration of the solution space, the algorithm incrementally narrows down the search, focusing more on areas with high potential based on the feedback from each cycle of simulations.

Given the complexity and resource intensive nature of CFD simulations with , multi-objective optimization scenarios, such as minimizing deviations from experimental data across different flow conditions SHERPA algorithm's efficiency in converging towards optimal solutions in relatively low number of cycles is beneficial.

In the context of this research, the SHERPA algorithm is used to explore the parameters of closure models in two-phase flow simulations by iteratively adjusting these parameters and evaluating the simulation results against experimental data. SHERPA guided the exploration process towards the most accurate and reliable models by systematically exploring their effects on the simulation results.

4.2. Simulation

CFD simulations are carried out utilizing the commercial software suit STAR-CCM+. This tool offers comprehensive multi-physics solvers and state-of-the-art capabilities required for detailed modeling of two-phase flow dynamics, essential for this study's objectives. A key feature of this tool is its flexibility in customizability and automatability. This feature is utilized in this study. Specifically, the process involves creating simulation templates with pre-defined solvers, models, and settings, while leaving geometric dimension, boundary conditions, operating conditions, and tunable model parameters as adjustable simulation

automation parameters for the automated exploration procedure. This enables generation of diverse simulation scenarios.

A critical step of the methodology is the automated pre-processing and case generation. This is achieved by defining flow domain dimensions as simulation parameters. This automation also handles mesh generation, where cell sizes are linked to these dimensions.

For the solution phase Eulerian multiphase solver is selected. This solver is capable of solving mass conservation and momentum conservation equations for multiple phases. This solver utilizes the TFM and offers a variety of closure models. Among the range of available turbulence models, the Realizable $k-\varepsilon$ model is chosen for the primary phase with the turbulence response model. Closure model sets selection is narrowed according to bubbly flow compatibility. All these selections are guided by the literature review of existing CFD studies.

Furthermore, the post-processing capabilities of STAR-CCM+ include automatic report generation and data exporting. Placement of probes in the flow domain, represented the measurement stations in related experimental configurations. This alignment with experimental configurations enables the digital representation of the conducted experiments. The acquisition of simulation data, including void fraction α_g , relative velocity v_{rel} , and turbulent kinetic energy of water k_l , is performed using STAR-CCM+'s built-in reporting functionality. The deviation of CFD simulation outputs against the experimental results at specified probes and corresponding measurement stations is assessed as shown in Eq.(205) providing a quantitative measure as the response.

$$E_{rel} = \frac{|V_{sim} - V_{exp}|}{|V_{exp}|} \quad (205)$$

The overall measure of error for the entire data-set is calculated as shown in Eq.(206) This allows systematic data collection and is required for the exploration process.

$$\bar{E}_{\text{rel}} = \frac{1}{N} \sum_{i=1}^N \frac{|V_{\text{sim},i} - V_{\text{exp},i}|}{|V_{\text{exp},i}|} \quad (206)$$

The CFD models for this study are prepared in STAR-CCM+, with templates and in an automated fashion to ensure consistency across all simulations. Each model is configured to replicate the conditions of a corresponding experiment, as outlined in Table 5.2, which summarizes the diverse experimental conditions examined. This approach offers a broad and robust basis for validating the closure models across a range of two-phase flow scenarios.

4.3. Automated Process Workflow

Two-phase flow CFD simulations work-flow automation is established with HEEDS and STAR-CCM+ through a coupling portal. The functionality of HEEDS is to automate the simulation processes, manage data and apply the advanced search algorithm SHERPA for design space exploration. It is designed to handle complex engineering problems where the design space is extensive and non-linear, with multiple competing objectives and constraints. In this study, HEEDS and the SHERPA algorithm are used for multi-objective design space exploration, to minimize the deviation between CFD simulations and experiment data across a range of flow conditions. The algorithm iteratively explores various combinations of design variables, which include tunable parameters of the closure models, and evaluates their performance against the predefined objectives.

In the context of this research, HEEDS is instrumental in systematically refining the closure models for two-phase flow. By leveraging its advanced optimization capabilities, the study aims to achieve closure models that not only fit the experimental data with high fidelity but also maintain robustness and applicability across various scenarios. an innovative approach to model development and validation, ensuring that the findings of this study are both scientifically and practically relevant.

This process involves the submission of all prepared CFD simulations to HEEDS, which then executes them sequentially. The baseline variables, representing the tunable parameters of the closure models, are consistently applied across all simulations.

HEEDS, utilizing its SHERPA algorithm, systematically evaluates the results of each CFD simulation against the corresponding experiment data. The algorithm then adjusts the baseline variables across all models and initiates a new set of simulations. This iterative process of running simulations, evaluating results, and adjusting variables continues until the optimal set of parameters is identified.

The objective functions in HEEDS are equi-weighted, focusing on minimizing the overall discrepancy between CFD results and experimental data. This multi-objective approach ensures that the optimized models perform well across a range of different experimental conditions, providing a comprehensive validation of their accuracy and applicability.

In this research, the integration of CFD with sophisticated search algorithms represents a key element of the methodology bringing an alternative perspective as utilizing the design space exploration approach to develop coefficient models for momentum closure relations in two-phase flow and validating the new models in an automated fashion.

The SHERPA algorithm conducts a comprehensive, iterative process, adjusting variables and rerunning simulations until an optimal set of parameters is identified. Performance metrics, according to the alignment of simulation results with experimental measurements, guide the optimization.

4.4. Test Case

The method is demonstrated with a test case using reference data from the experiment, H3, of Hosokawa and Tomiyama [72]. Void fraction data for this experiment is collected from 9 measurement stations. The simulation outputs at these stations for the respective variables are designated as responses. The set of selected closure models, correction models, turbulence models and their respected tunable model parameters are given below in Table 4.1 below,

	model	constants
C_D	Tomiyama	-
C_D correction	α^n	$-50 \leq n \leq 0$
C_L	Tomiyama	-
C_L correction	Podowski	-
C_{TD}	Burns	$0.1 \leq \sigma_\alpha \leq 10$
C_{WL}	Antal	$-0.1 \leq C_{w1} \leq 0$ $0 \leq C_{w2} \leq 0.1$
TR	Issa	-
BIT	Troshko and Hassan	$0.01 \leq C_3 \leq 10$ $0 \leq C \leq 10$

Table 4.1 Closure model set and tuning parameter ranges

The objective of this method is to minimize the mismatch of experimental data and simulation results at each corresponding measurement station. This deviation is quantified as the relative error, calculated using the formula given in Eq.(205). The procedure adopted is classified as a multi-objective design optimization. The performance regarding each design iteration is calculated based on the weighted sum of all objectives. The performance improvement is evaluated relative to the baseline model, which represents the simulation conducted with default values of the tunable parameters.

	baseline	tuned
n	0	-27
σ_α	1	0.1
C_{w1}	-0.01	-0.099
C_{w2}	0.05	0.33
C_3	0.45	4.35
C	1	0.54
P	-6.85	-1.99

Table 4.2 Tuning parameters for the baseline and tuned models

The results and relative errors of the base model are shown in Fig. (4.2), with a calculated performance value of -6.85. After 500 evaluations, the optimal design emerged with a performance value of -1.99, indicative of reduction in deviation compared to the base model. The outcomes of this optimal design are detailed in Figure.(4.2). Presented figure not only display the simulation results but also presents relative errors, showing the effectiveness of the proposed method.

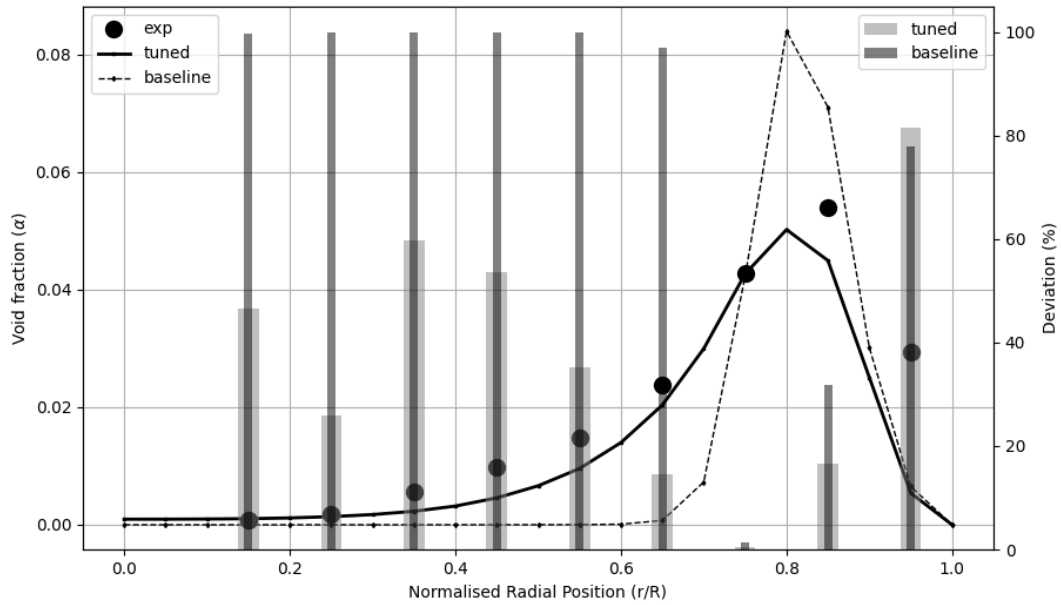


Figure 4.2 Baseline vs. tuned model comparison plot

In conclusion, this method demonstrates a systematic and efficient approach to enhancing the accuracy of simulations by fine-tuning the parameters of closure models. The use of a design space exploration multi-objective optimization framework allows for a comprehensive evaluation of model performance, ensuring improvement over the base model. The significant reduction in deviation from experimental data shows the method's effectiveness in refining simulations.

5. DATA AND ANALYSIS

This section introduces the outcomes of the simulations conducted using Star-CCM+ with an Eulerian multiphase solver, against the selected experiment data listed in Table 5.2. The listed experiments are selected to cover both wall and core peaking categories. Pipe diameters and void fractions varies between, 25 mm and 60 mm and 2.5% and 16% respectively. The continuous phase superficial velocities span 0.5 m/s to 1.03 m/s, dispersed phase superficial velocities span 0.018 m/s and 0.2 m/s and the bubble diameters in the experiments span 2.94 mm to 4.25 mm. Cases with experiment data for single-phase conditions are used to determine cell sizes for the simulations.

Initially a case is presented to show the effect of model combinations on the results of the simulation in terms of predicting the volume fraction distribution. Table.4.2 shows the selected closure model set. This set is also used for method testing. The case is a wall peaking case with the corresponding experiment ID H3 with 2.8% void fraction and 3.52 mm. bubble diameter with continuous and dispersed superficial velocities, 1.0 m/s , 0.035 m/s respectively. Momentum closure model set used in default simulations is presented with the regarding tunable parameters.

Tomiyama Drag Coefficient Model

Tomiyama et al.[19], general drag coefficient is given in Eq.(84). This model is used as presented thus no tunable parameter is present however case specific particle size is taken into account by the model through the Eo number.

Volume Fraction Exponent Drag Correction

The form of this correction factor is presented below;

$$C_D = f_D C_{D\infty} \quad (207)$$

where,

$$f_D = \alpha_c^{n_D} \quad (208)$$

This correction model utilizes the void fraction value thus has the respective tunable parameter.

Tomiyama Lift Coefficient

The Tomiyama lift coefficient model [28], is shown in Eq.(106) Since no tunable parameter exists, this model is used as presented. This C_L model is used as presented thus no tunable parameter is present however as the C_D model, case specific particle size is considered by this model via the E_o number.

Burns' Turbulent Dispersion Force Model (FAD)

Burns [37] F_{TD} model is given in Eq.(123). The F_{TD} model is used with the tunable parameter σ_{TD} within the defined range given in Table. 5.1.

Antal Wall Lubrication Force Model and Coefficient

Antal et al. [38] F_{WL} model [38], is given in Eq.(124) with the coefficients C_{W1} and C_{W2} as;

$$C_{W1} = 0.06|\mathbf{v}_g - \mathbf{v}_l| + 0.14 \quad (209)$$

$$C_{W2} = 0.147 \quad (210)$$

where these coefficients are set as tunable parameters with the defined range given in Table. 5.1.

Shaver and Podowski Wall Damping Lift Coefficient Model

Shaver and Podowski [30] lift model is presented in Eq. 110. Since this correction model is a self adjusting function, no tunable parameter exists and is used as presented.

Troshko and Hassan

Troshko and Hassan [62] BIT model is presented below in Eq.s 211, 214 with the source definitions

Turbulent Kinetic Energy (k) Equation;

$$\begin{aligned} \frac{\partial(\rho_c \alpha_c k_c)}{\partial t} + \nabla \cdot (\rho_c \alpha_c \mathbf{U}_c k_c) = \alpha_c \mathbf{T}_c^{Re} : (\nabla \mathbf{U}_c) - \nabla \cdot \left(\frac{\rho_c \mathcal{V}_c^t}{\sigma_k} \nabla k_c \right) \\ - \rho_c \alpha_c \varepsilon_c + \frac{3}{4} \frac{C_d}{d} \alpha_d \rho_c |U_r|^3 \end{aligned} \quad (211)$$

smallest eddy frequency scale [48];

$$\omega = \frac{\varepsilon}{k} \quad (212)$$

bubble dissipation frequency from bubble relaxation time constant τ_b proposed by Bertodano [61];

$$\omega_b = (\tau_b)^{-1} = \left(\frac{2}{3} \frac{C_{VM}}{C_D} \frac{D_b}{u_r} \right)^{-1} \quad (213)$$

Dissipation Rate (ε) Equation;

$$\begin{aligned} \frac{\partial(\rho_c \alpha_c \varepsilon_c)}{\partial t} + \nabla \cdot (\rho_c \alpha_c \mathbf{U}_c \varepsilon_c) = \omega (C_1 \alpha_c \mathbf{T}_c^{Re} : (\nabla \mathbf{U}_c) - C_2 \rho_c \alpha_c \varepsilon_c) \\ - \nabla \cdot \left(\frac{\rho_c \mathcal{V}_c^t}{\sigma_\varepsilon} \nabla \varepsilon_c \right) + \omega_b C_3 \frac{3}{4} \frac{C_d}{d} \alpha_d \rho_c |U_r|^3 \end{aligned} \quad (214)$$

where C_3 and C_ω are the new model constant, and they are used as tunable parameters with the limits given below in Table. 5.1. The remaining are the standard k- ε model constants in Table. 3.1 and they are not subject to tuning.

The tunable parameters and their limits are presented in Table. 5.1

min	variable	max	resolution
0	Drag Correction Volume Fraction Exponent n	1	101
0	BIT Source C_3	1	101
0	BIT Production Calibration Factor C_{CF}	1	101
0	Turbulent Dispersion Prandtl Number σ_α	1	101
-0.1	Wall Lubrication Coefficient C_{w1}	0	101
0	Wall Lubrication Coefficient C_{w2}	0.1	101

Table 5.1 Limits and resolution for the variables

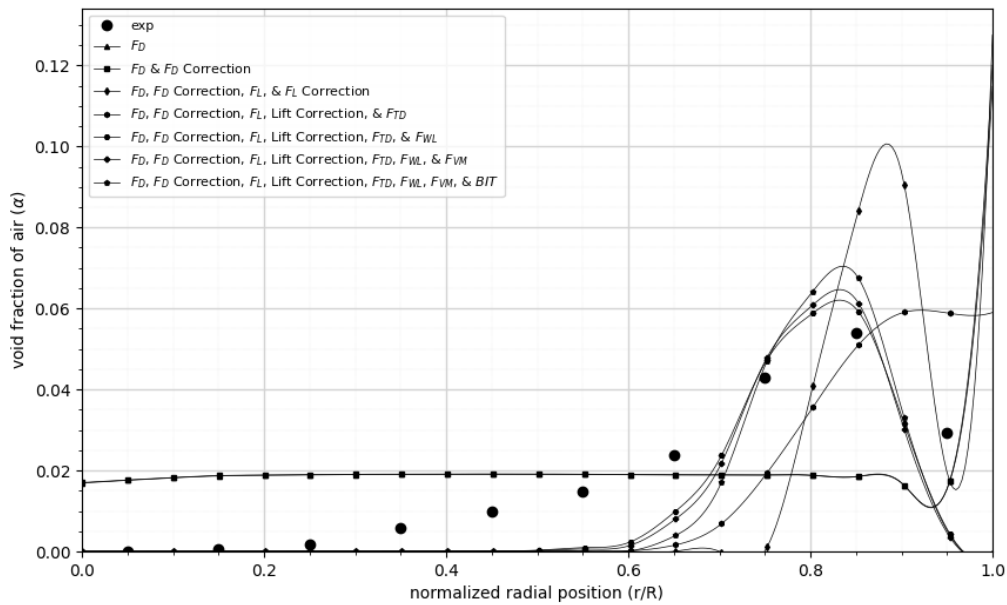


Figure 5.1 H3 Void fraction (closure model sets)

The initial simulations, focusing solely on the drag model, showed negligible effects on void fraction distribution. Addition of the swarm corrector over the drag model did not have any effect since the absence of any lateral force sustained the flat volume fraction distribution. The subsequent addition of the lift model, although physically accurate, led to unrealistic results, pushing the air phase towards the pipe wall and causing accumulation. Although the lift correction model, Podowski sets $C_L = 0$ for the neighboring cells to the wall, accumulation was not entirely eliminated, suggesting the presence of competing additional factors influencing the volume fraction profile in wall boundary proximity. However, the

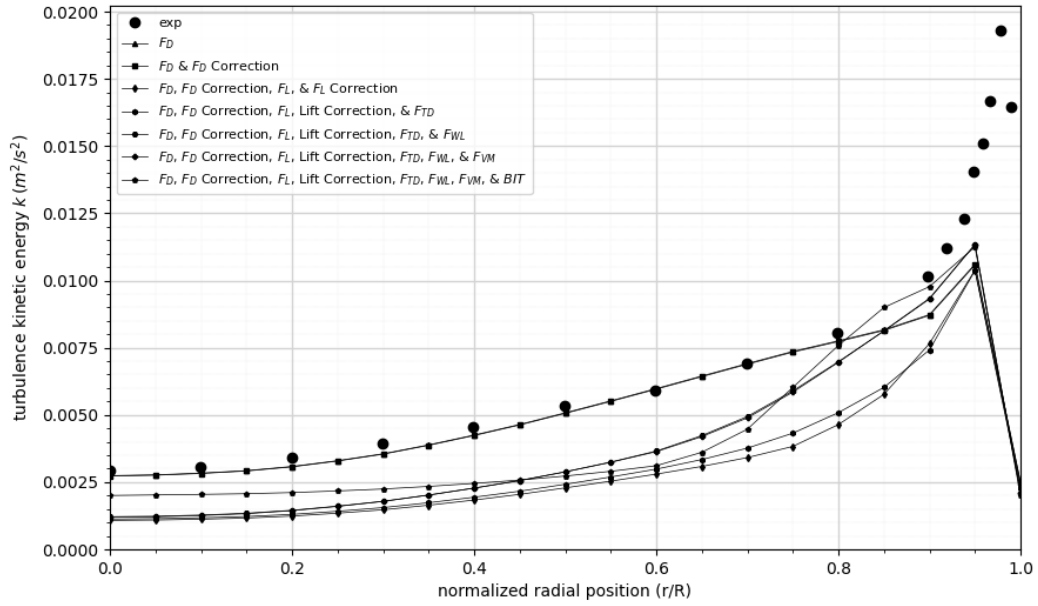


Figure 5.2 H3 Turbulence kinetic energy (closure model sets)

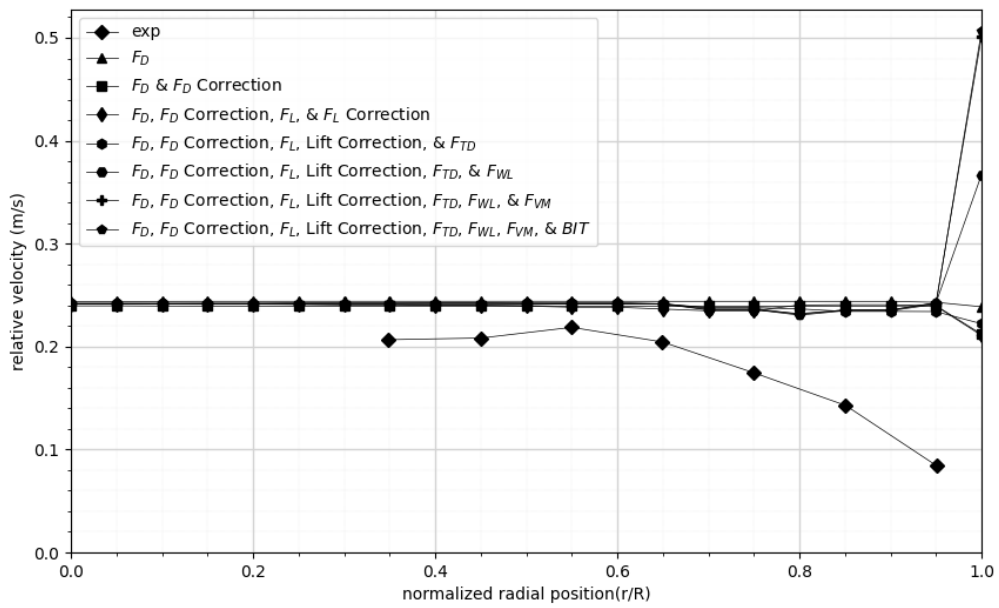


Figure 5.3 H3 Relative velocity (closure model sets)

incorporation of the F_{WL} model considerably improved the results by reducing void fraction near the wall and creating a more realistic peak. The inclusion of F_{TD} further refined the distribution, flattening the peak in wall proximity. Taking the dispersed phase turbulence into account by use of BIT model enhanced the turbulence resolution and overall solution. Yet it is still interesting to see that a widely preferred closure model set directs the results towards a clustering near the wall boundary. This is a good indicator that models developed for single bubbles need to be corrected with the appropriate correction models which are functions mostly functions of void fraction or gradient of relative velocity.

Data for this study is collected from 24 measurement stations. Among these, 9 provide data on void fraction, 7 on relative velocity, and 17 on turbulence kinetic energy. Error analysis, revealed high discrepancies across all cases, often exceeding 50% relative error. Although such error values are not acceptable for single-phase CFD simulations, they are quite common for multi-phase simulations which results from the added complexity rising from closure models. The Eulerian solver's requirement to solve the conservation equations for each phase individually, coupled with the need for inter-phase closure relations (including drag and non-drag models), introduces an additional level of non-linearity absent in single-phase flow simulations.

The simulation results revealed the role of specific models, particularly the models that effect the near wall behavior. Wall lubrication model and the lift correction models are critical in predicting the correct void fraction distribution trend. However, the persistent high error rates across all cases indicate a gap in the current modeling approach for multiphase flows.

5.1. Experiment Groups

The experiments selected for this study span a broad range of flow conditions with the details given in Table 5.2. The experiments by Serizawa et al. [76], [77], [78], provide data sets that include void fraction, phase velocities, scaled turbulence kinetic energy. Their experiment data for the phase velocities are normalized by values at pipe center-line. Liu's [69], [79], [80] experiments were conducted at 2 different liquid velocities.

Measurements include void fraction, phase velocities and turbulence kinetic energy presented scaled. These experiments are notable for their high bubble Reynolds number conditions. Hosokawa's [72] experiments focus on multi-scale in bubbly flows. These experiments provide void fraction, relative velocities and turbulence kinetic energy. None of these experiments provide detailed inlet profile data. Given bubble size data is used with mono-dispersed case assumption. Each of these experiments offers data for validating the single-phase. These data is used for validating our approaches parameter sets.

The series of reference experiments shown in Table 5.2 is selected towards the assessment of simulation results via comparison. The selected experiments provide single phase data besides two-phase data. Although the majority of the data is for wall peak profiles, there are also core peak profile data provided with certain experiments.

Table 5.2 List of reference experiments

ID	d_d (mm)	J_l (m/s)	J_b (m/s)	d_b (mm)	α_b (%) (%)	Re_b	Profile
S0	60	1.03					
S1	60	1.03	0.0753	4.0	3.97	763	Wall Peak
S2	60	1.03	0.151	4.0	10.23	1480	Wall Peak
S3	60	1.03	0.151	4.0	16.27	930	Wall Peak
L01	57.2	0.5					
L1	57.2	0.5	0.1	2.94	15.2	1934	Wall Peak
L02	57.2	1.0					
L2	57.2	1.0	0.1	3.03	10.6	2859	Wall Peak
L3	57.2	1.0	0.2	3.89	15.7	4942	Wall Peak
H01	25.0	0.5					
H1	25.0	0.5	0.018	3.21	2.5	579	Core Peak
H2	25.0	0.5	0.031	4.25	4.1	1285	Core Peak
H02	25.0	1.0					
H3	25.0	1.0	0.035	3.52	2.8	1257	Wall Peak
H4	25.0	1.0	0.042	3.66	3.2	1204	Wall

5.2. Single Phase

Simulation results with grid sensitivity investigation for the single phase scenarios are presented for the corresponding experiments. The selected grid size per case is used for

the corresponding two-phase simulations.

Single phase simulation result for the Serizawa al. [76], [77], [78] experiment with the ID S0 is presented in Fig. 5.4. It is noted that the experiment data is normalized for the velocity by the velocity value at the pipe center and scaled turbulent kinetic energy is provided. The simulation versus experiment data mismatch is significant especially for the turbulent kinetic energy. The cause of mismatch is the poor near wall resolution besides the selected turbulence model.

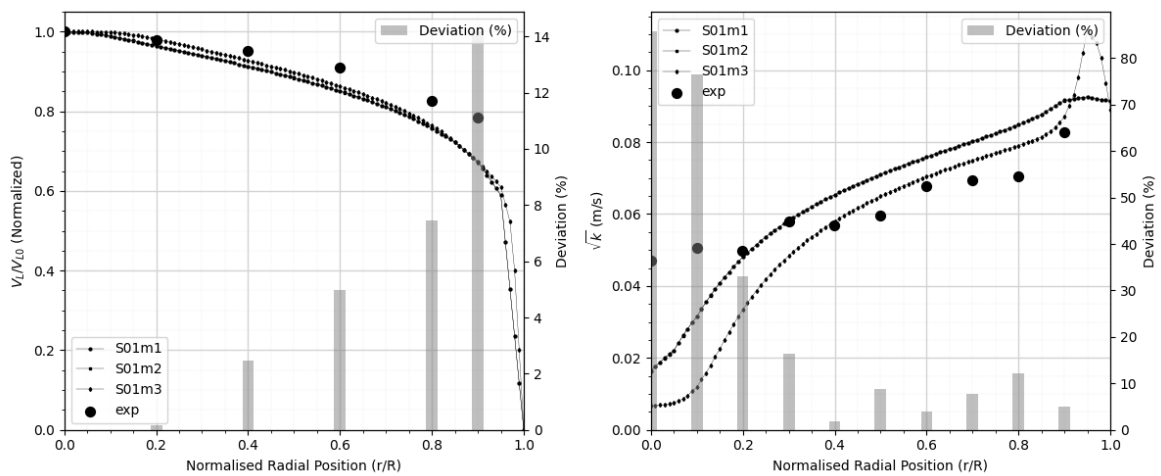


Figure 5.4 S0 results

Fig. 5.5 presents the single phase simulation result for the Liu [80] experiment with the ID's L01 and L02 corresponding to high and low velocity cases respectively is presented in Fig 5.5. There is only turbulent kinetic energy data for this experiment. The simulation and experiment data mismatch is significant in the wall boundary proximity for velocity besides turbulent kinetic energy throughout the whole flow domain.

Single phase simulation result for the Hosokawa [72] experiments with the ID H01 and H02 corresponding to high and low velocity cases respectively is presented in Fig. 5.6. It is noted that the experiment data is normalized for the velocity by the velocity value at the pipe center and scaled turbulent kinetic energy is provided. The simulation and experiment data mismatch is significant especially for the turbulence kinetic energy.

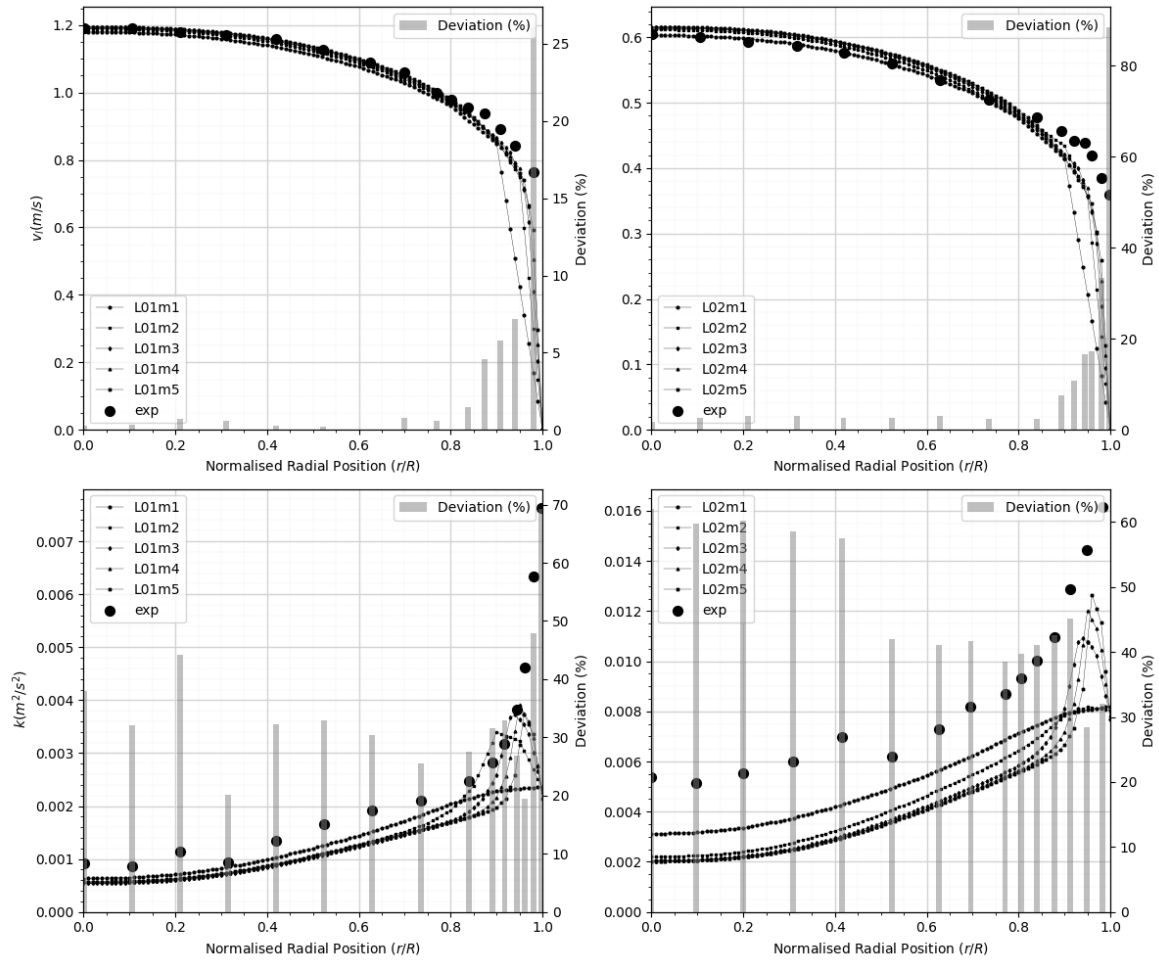


Figure 5.5 L01-L02 results

Although mismatch of simulated and experiment data is observed, the reason being the near wall resolution efficiency, it is a typical practice for two-phase flow CFD simulations to disregard it since the grid size and grid size change profile of two-phase simulations effect the stability of the overall simulation.

5.3. Default Parameters

5.3.1. Wall Peak

Two phase simulations for the selected experiments are conducted and the results are presented. The set of closure models selected for the conducted simulations are presented

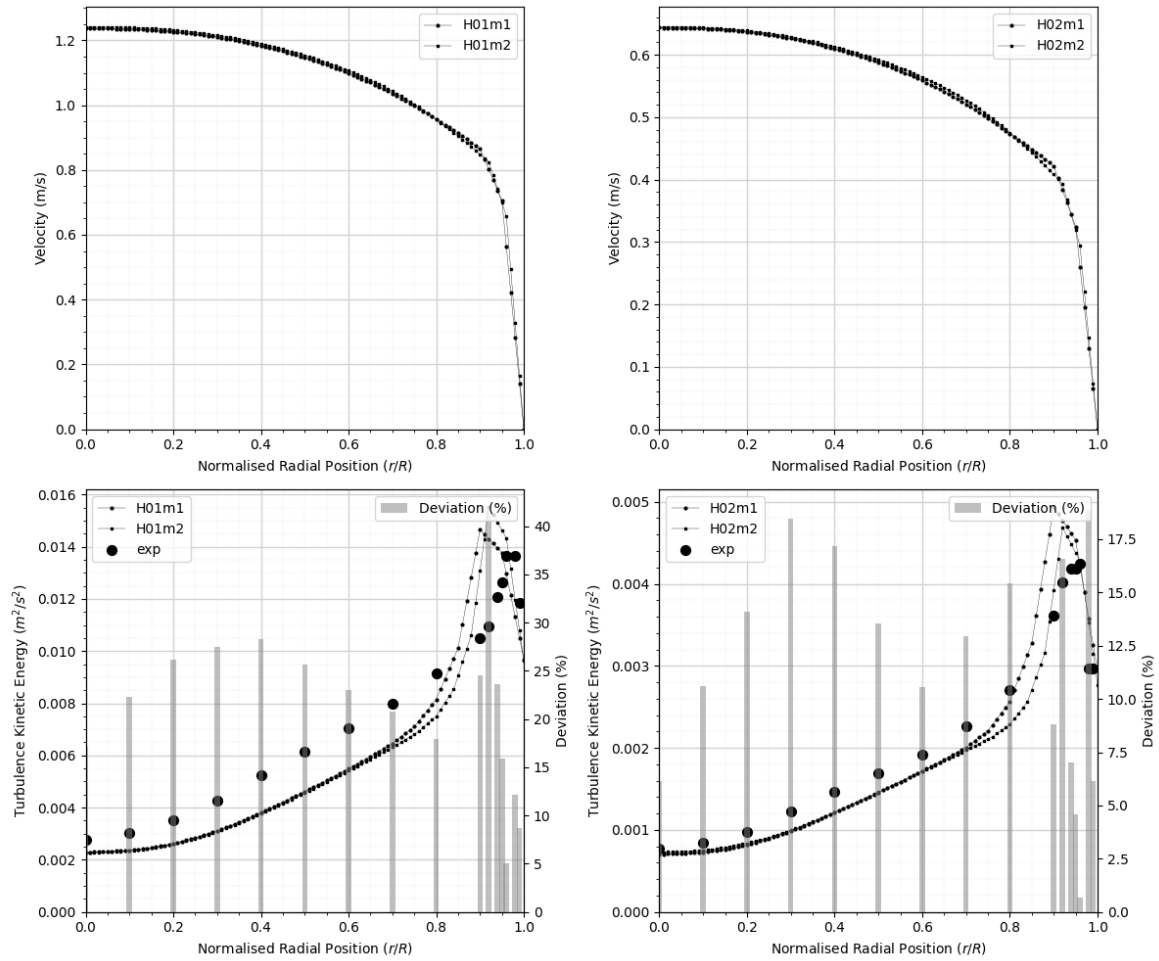


Figure 5.6 H01-H02 results

below in Table 4.1 and the related coefficients are presented in Table 4.2 as the default parameter set.

Two phase simulation result for the Serizawa al. [76], [77], [78] experiment with the ID S1 is presented in Fig. 5.7 . Besides comparison, Fig. 5.8 is presented to indicate the profiles for drag and lift coefficients (C_D, C_L) and bubble and rotational Reynolds numbers, (Re_b, Re_ω) along the measurement stations. It is noted that although the trend match is observed experiment data mismatch is significant.

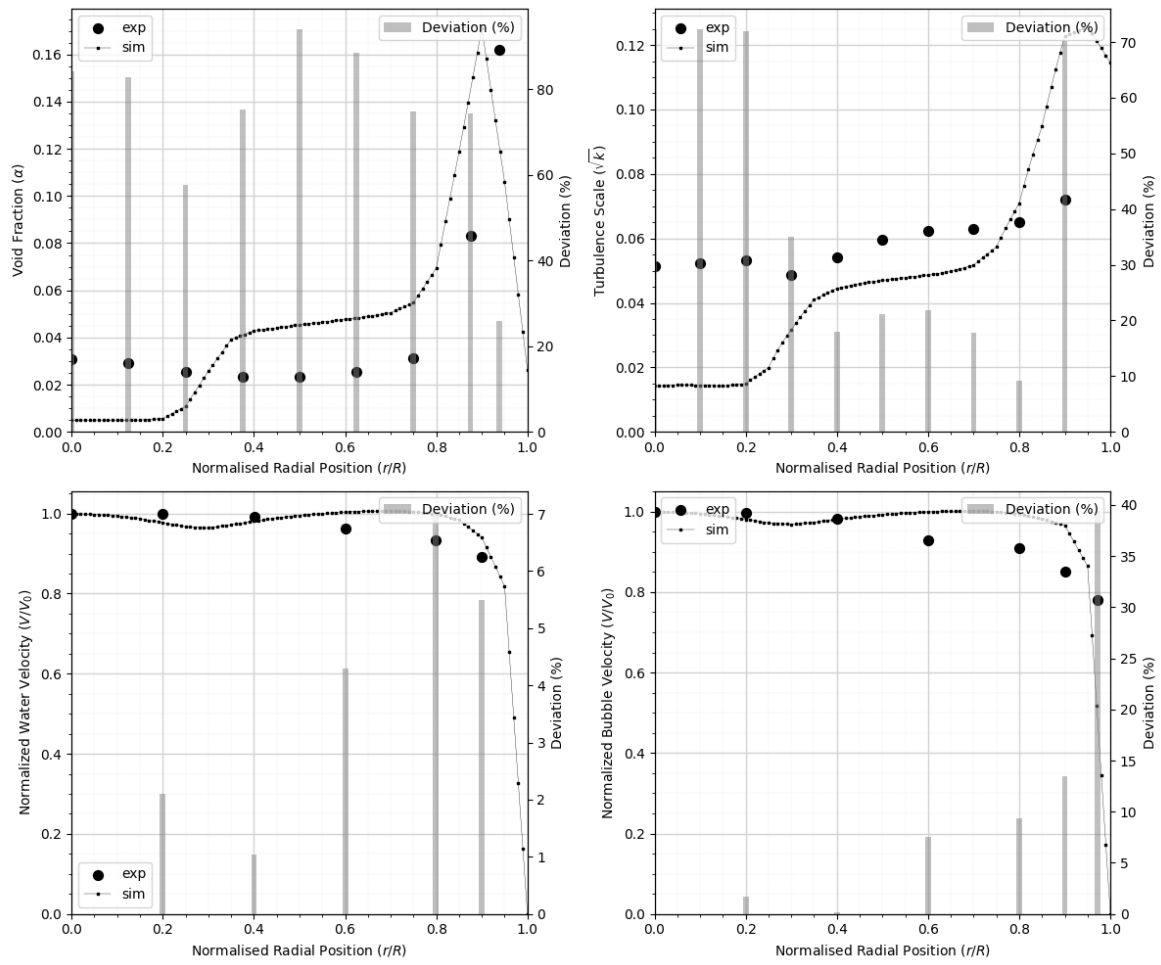


Figure 5.7 S1 results 1 (default sets)

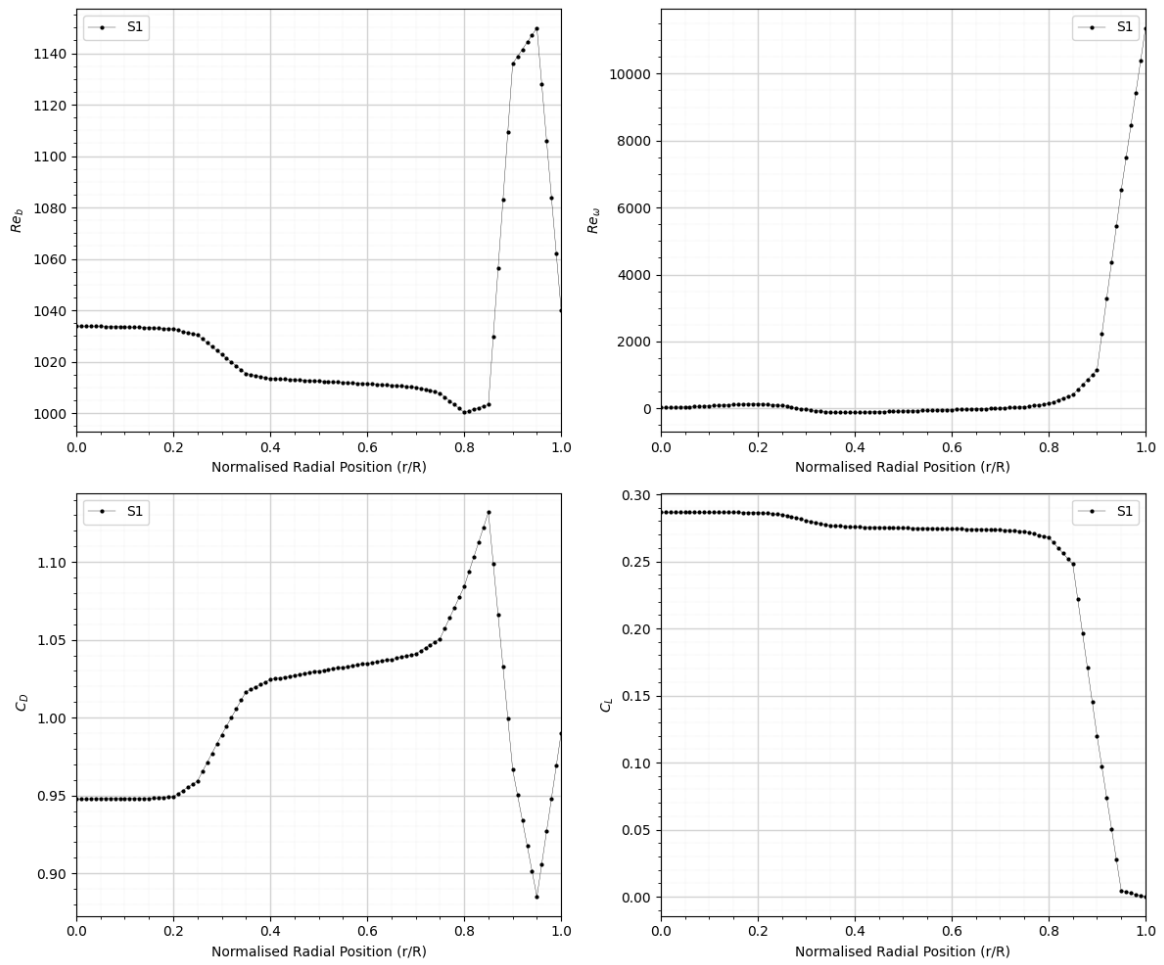


Figure 5.8 S1 results 2 (default sets)

Fig. 5.8 shows the steep change in the magnitude of the Re_w in the respective plot. This clearly indicates the significance of the wall boundary for most of the phenomena

Result for the experiment with the ID S2 is presented in Fig. 5.9. Simulated and experiment data mismatch especially for the void fraction distribution is observed while normalized water velocity deviation was relatively low.

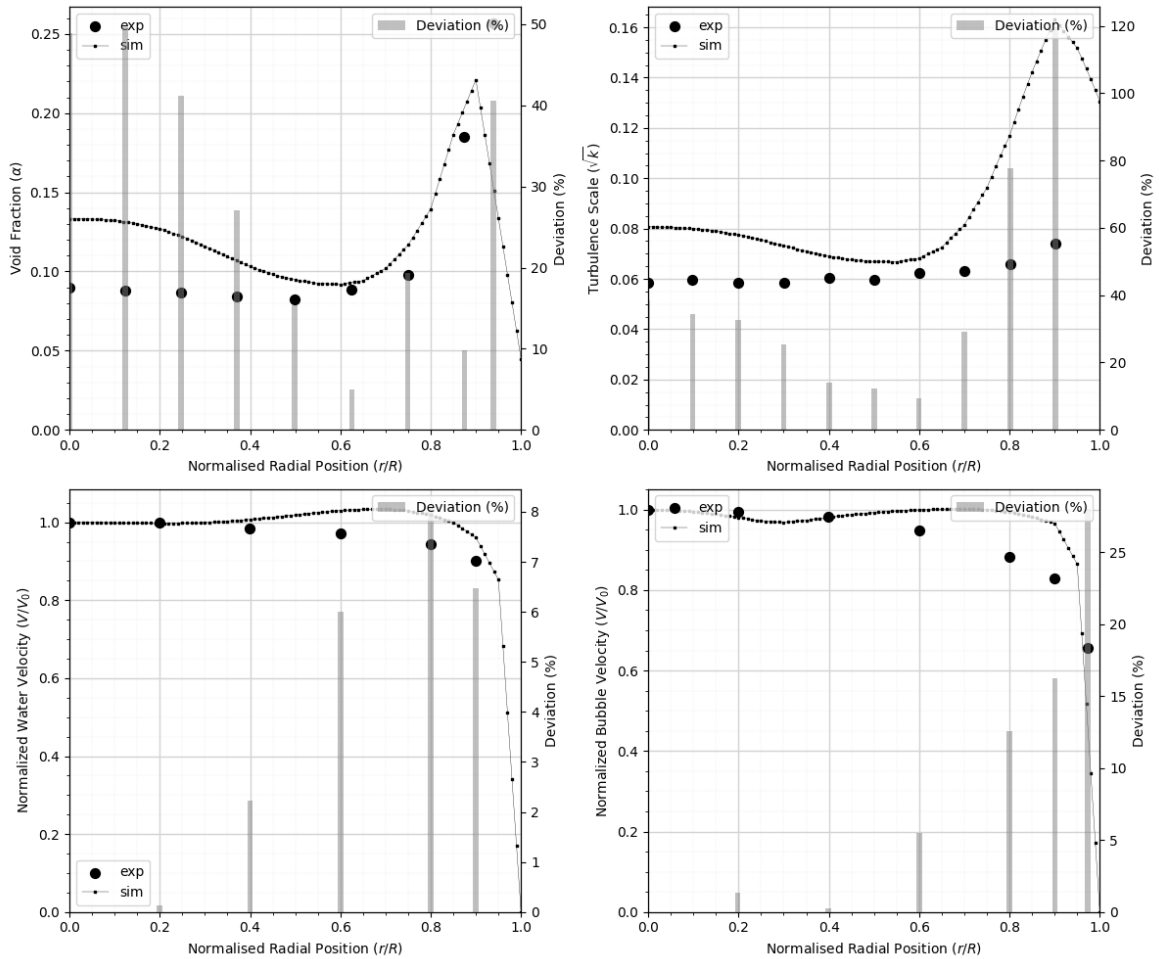


Figure 5.9 S2 results (default sets)

Result for the experiment with the ID S3 is presented in Fig. 5.10. Simulated and experiment data mismatch especially for the void fraction distribution is observed while normalized water velocity deviation was relatively low.

Two phase simulation result for the Liu [80] experiments with the IDs L1, L2 and L3 corresponding to wall peaking cases are presented in Figs 5.11, 5.12 and 5.13 respectively.

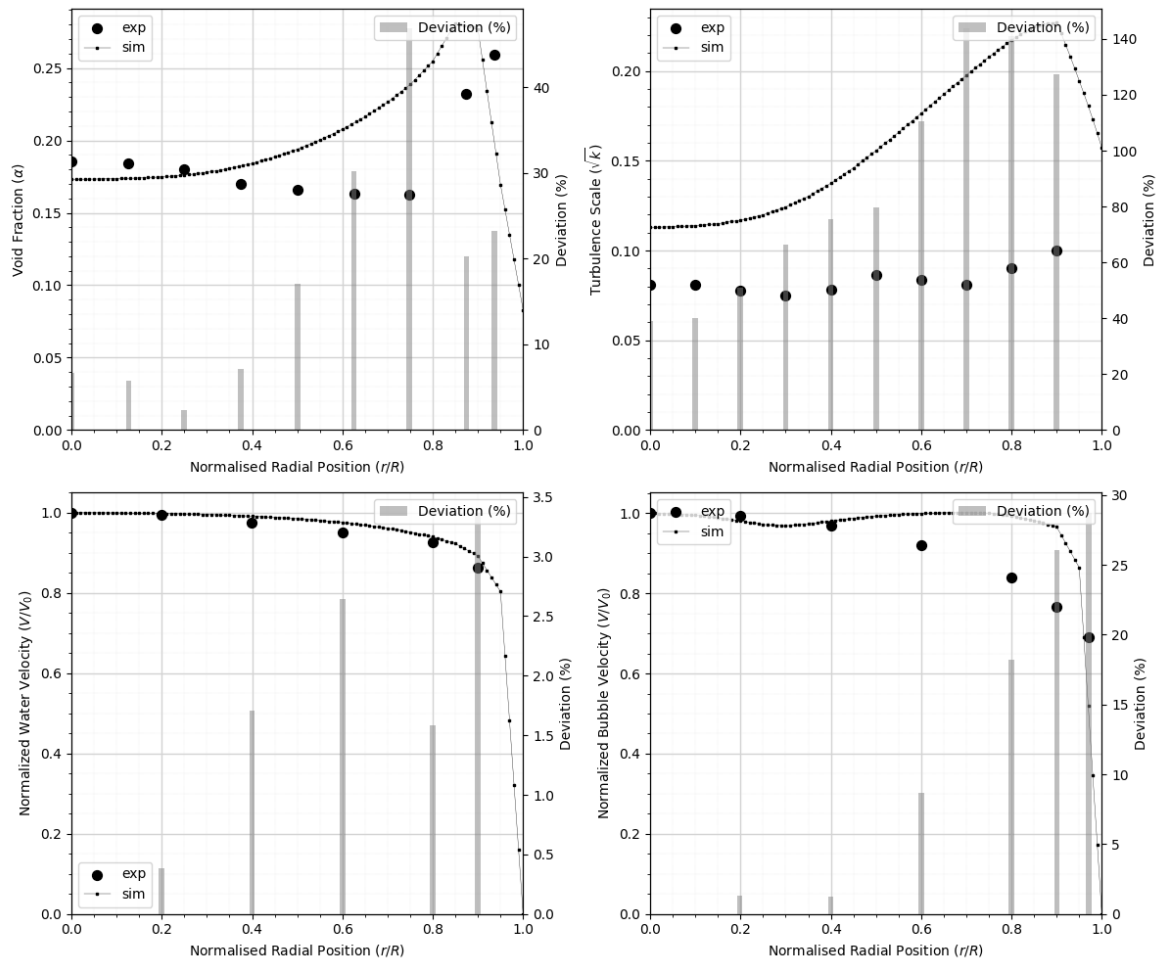


Figure 5.10 S3 results (default sets)

Two phase simulation result for the Hosokawa [72] experiments with the ID H3 and H4 corresponding to wall peaking cases are presented in Figs 5.14 and 5.15 respectively.

5.3.2. Core Peak

Two phase simulation result for the Hosokawa [72] experiments with the ID H1 and H2 corresponding to core peaking cases are presented in Figs 5.16 and 5.17 respectively.

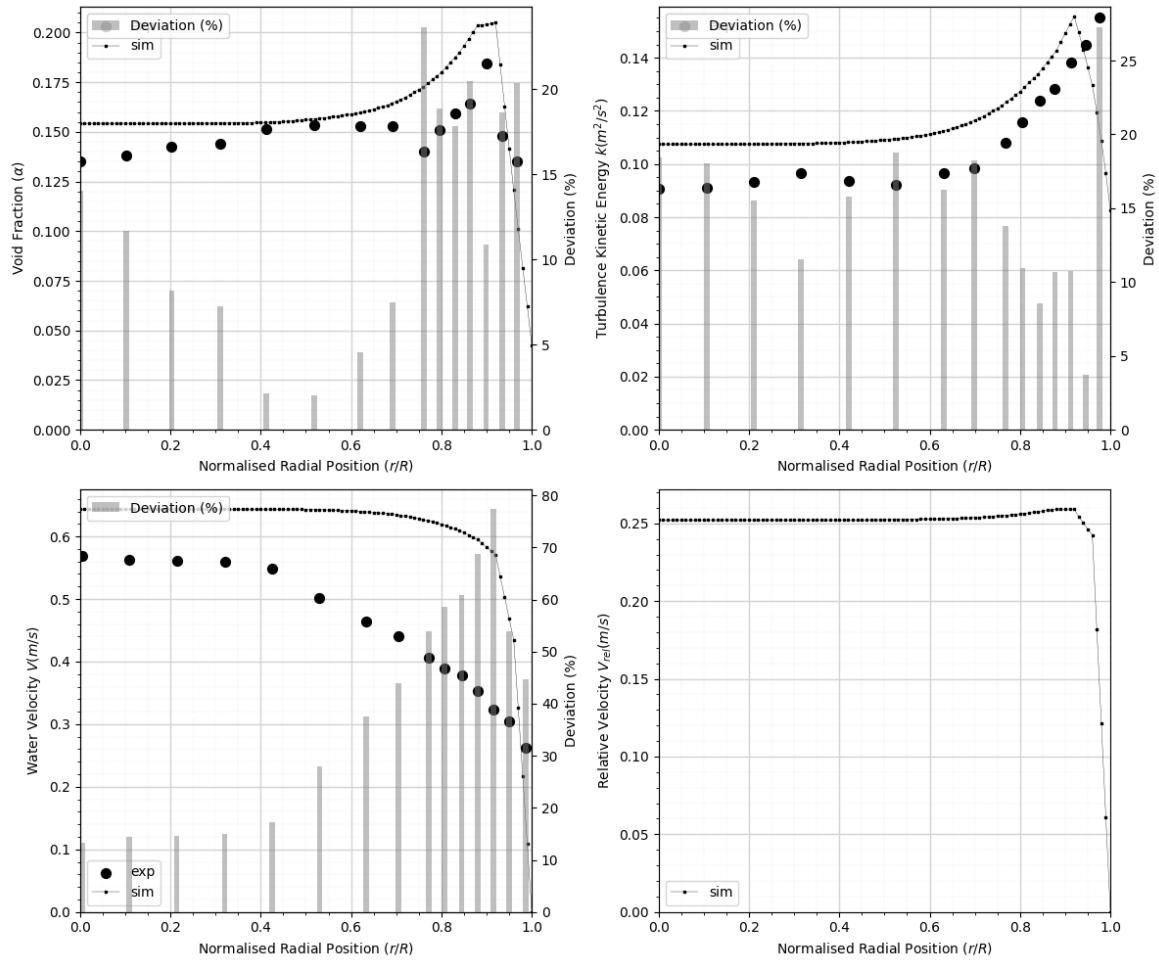


Figure 5.11 L1 results (default sets)

5.4. Parameter Tuning

5.4.1. Wall Peak

L1-L2-L3 tuning

Liu [80] experiments with the IDs L1, L2 and L3 corresponding to wall peaking cases are selected for parameter tuning simultaneously. The baseline model has 6 tunable parameters and the experiment provides void fraction, turbulence kinetic energy and liquid velocity data from 15 measurement stations making a total of 135. This results in an optimization statement with 135 responses to be minimized by modifying 6 variables between the predefined range given in Table. 5.3 at the specified resolution. The performance value P

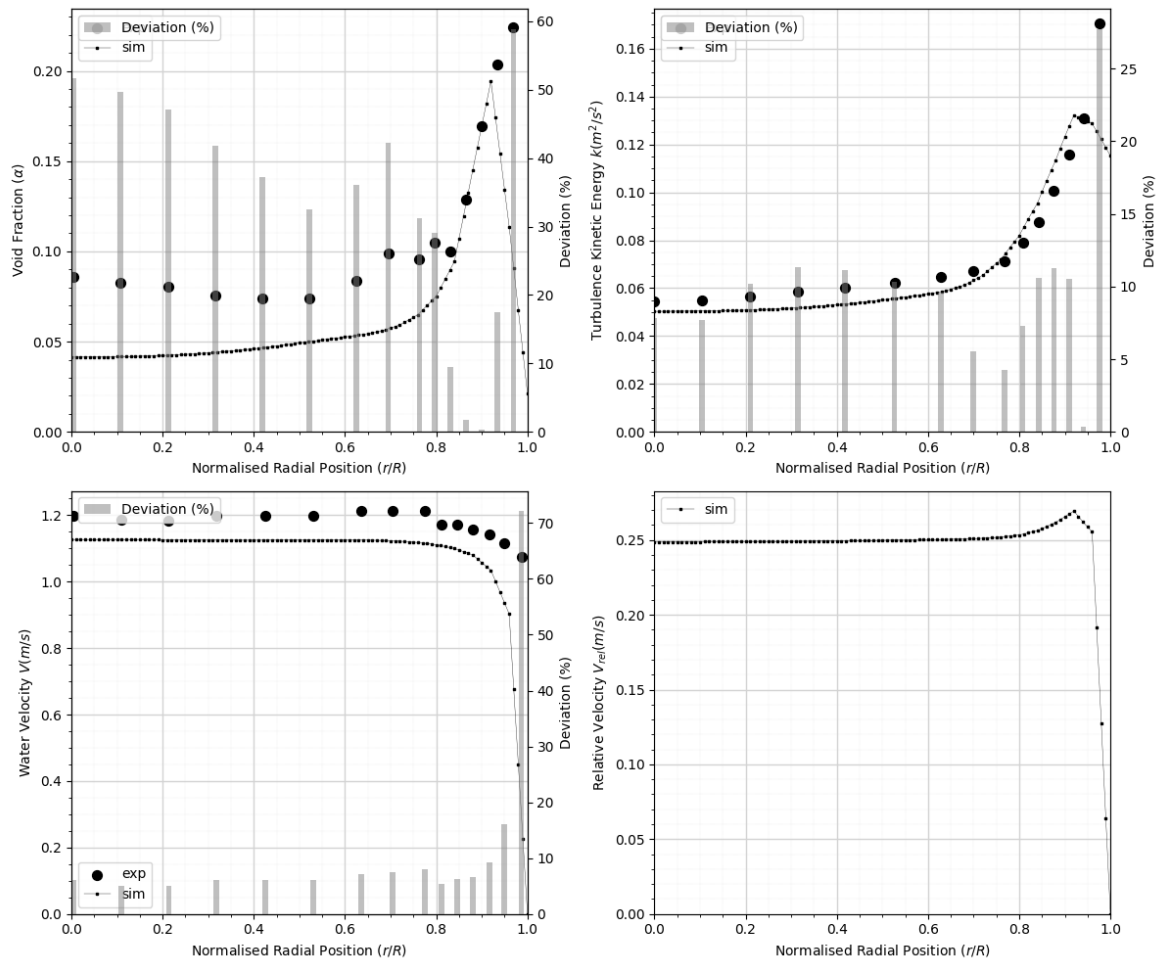


Figure 5.12 L2 results (default sets)

for the baseline value is set to -270 due to weighting. The responses related to turbulence kinetic energy and liquid velocity for all 3 cases were set to have linear weights of 1 while the void fraction responses were set to 4 for their linear weights. After the specified 4000 runs, the performance value P reached the value of 249. The comparison plot of this study is presented in Figs 5.18, 5.19, 5.20.

The default and the tuned model set parameters are presented in Table. 5.4.

It is seen that for the L1 case, simulation with the tuned parameter set performed well in turbulence kinetic energy and velocity predictions. Void fraction distribution in contrast is arguable thus, while better prediction was obtained for the near wall region, core region showed poor performance.

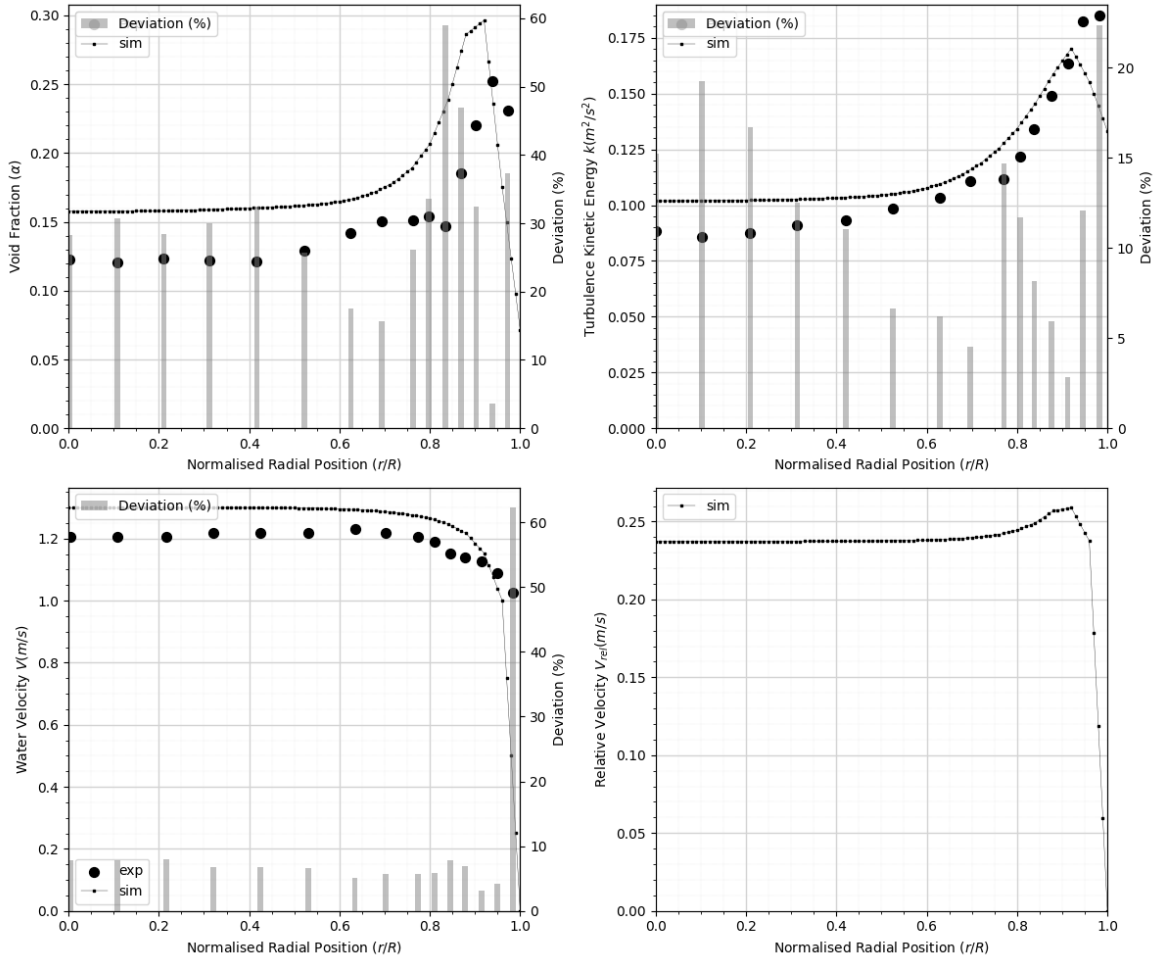


Figure 5.13 L3 results (default sets)

min	variable	max	resolution
0	Drag Correction Volume Fraction Exponent n	1	101
0	BIT Source C_3	1	101
0	BIT Production Calibration Factor C_{CF}	1	101
0	Turbulent Dispersion Prandtl Number σ_α	1	101
-0.1	Wall Lubrication Coefficient C_{w1}	0	101
0	Wall Lubrication Coefficient C_{w2}	0.1	101

Table 5.3 Limits and resolution for the variables

	n	σ_α	C_{w1}	C_{w2}	C_3	C_{CF}	P
baseline	0	1	-0.01	0.05	0.45	1	-270
tuned	0.02	0.82	-0.014	0.49	0.41	0.98	-249

Table 5.4 Baseline vs. tuned model parameters for L1-L2-L3

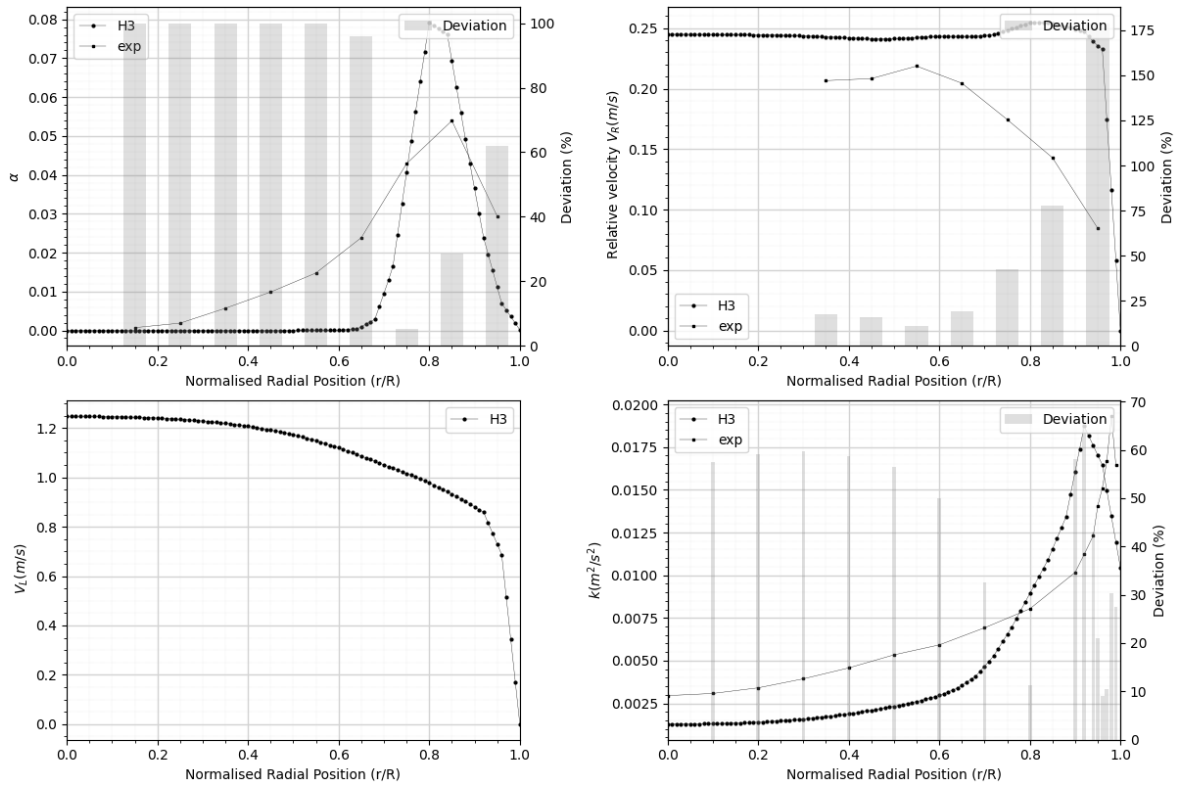


Figure 5.14 H3 results (default sets)

The simulation for the L2 case with the tuned parameter set showed poor performance on all comparisons.

The simulation for the L3 case with the tuned parameter set resulted in considerable in performance on all comparisons.

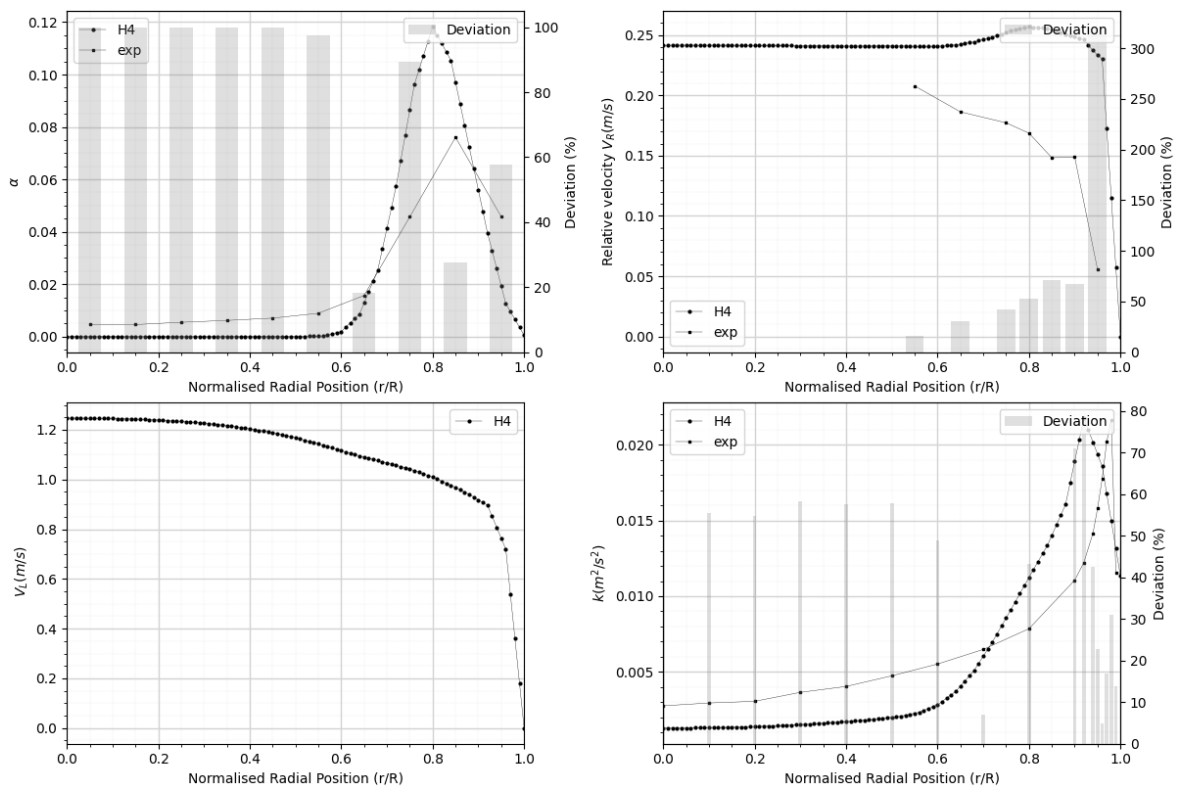


Figure 5.15 H4 results (default sets)

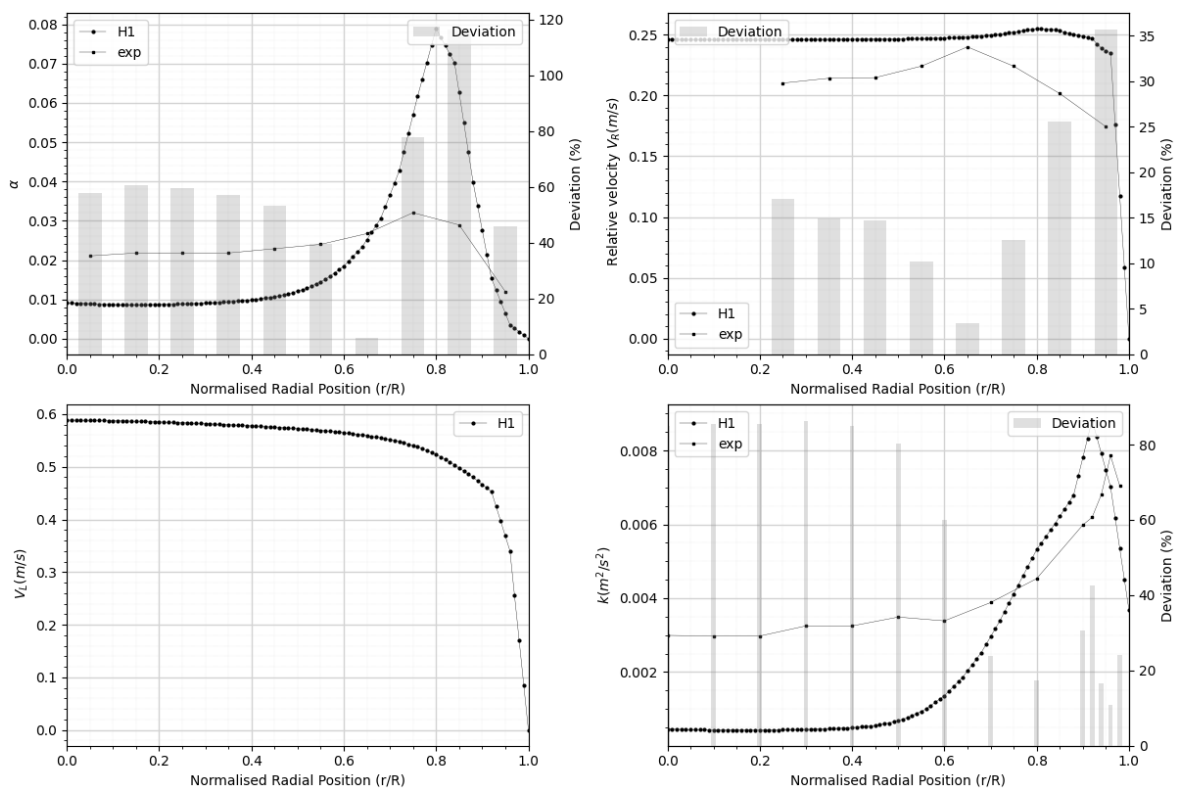


Figure 5.16 H1 results (default sets)

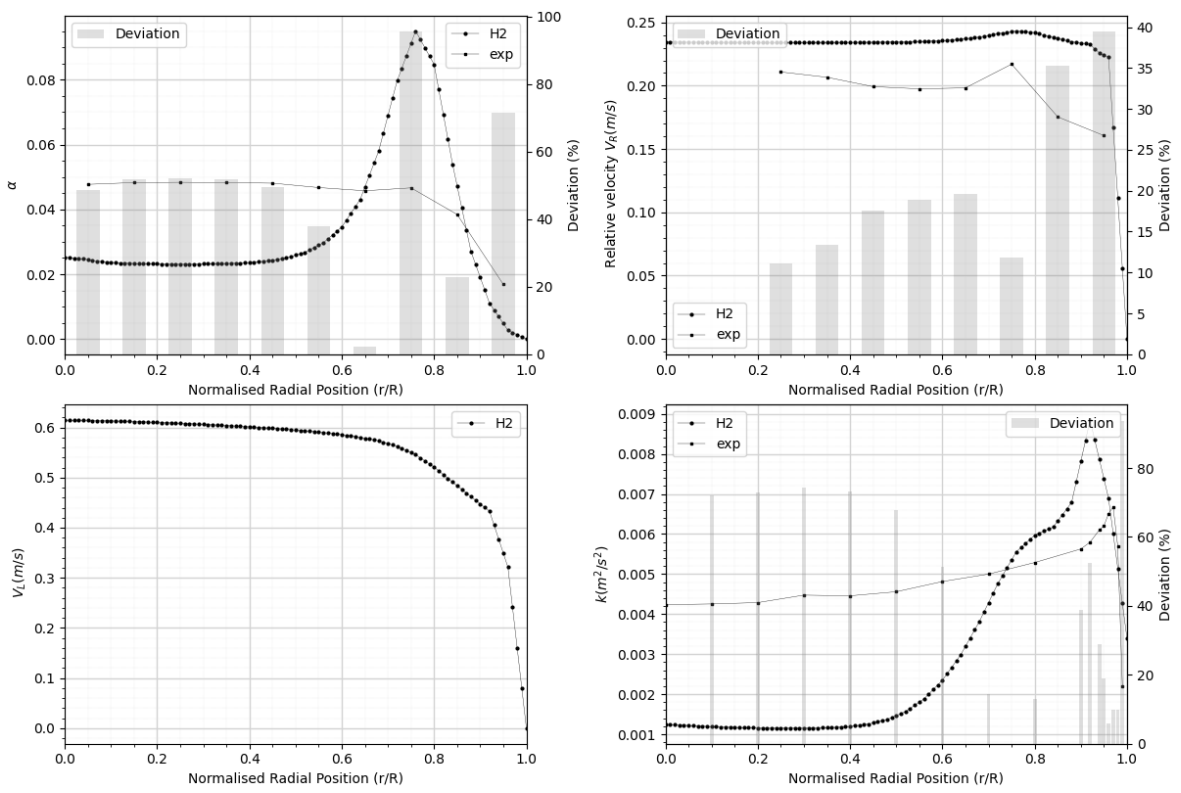


Figure 5.17 H2 results (default sets)

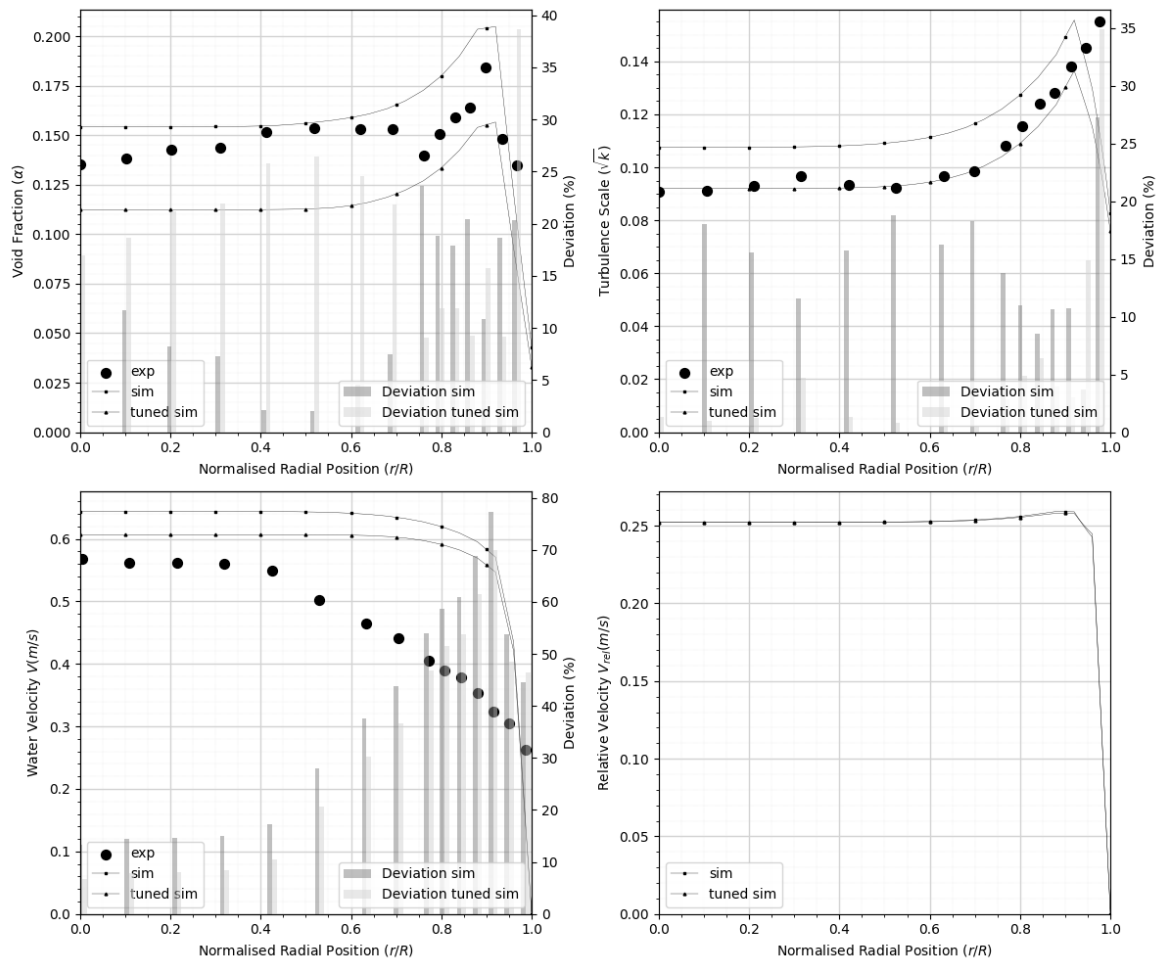


Figure 5.18 L1 results (tuned vs. default sets)

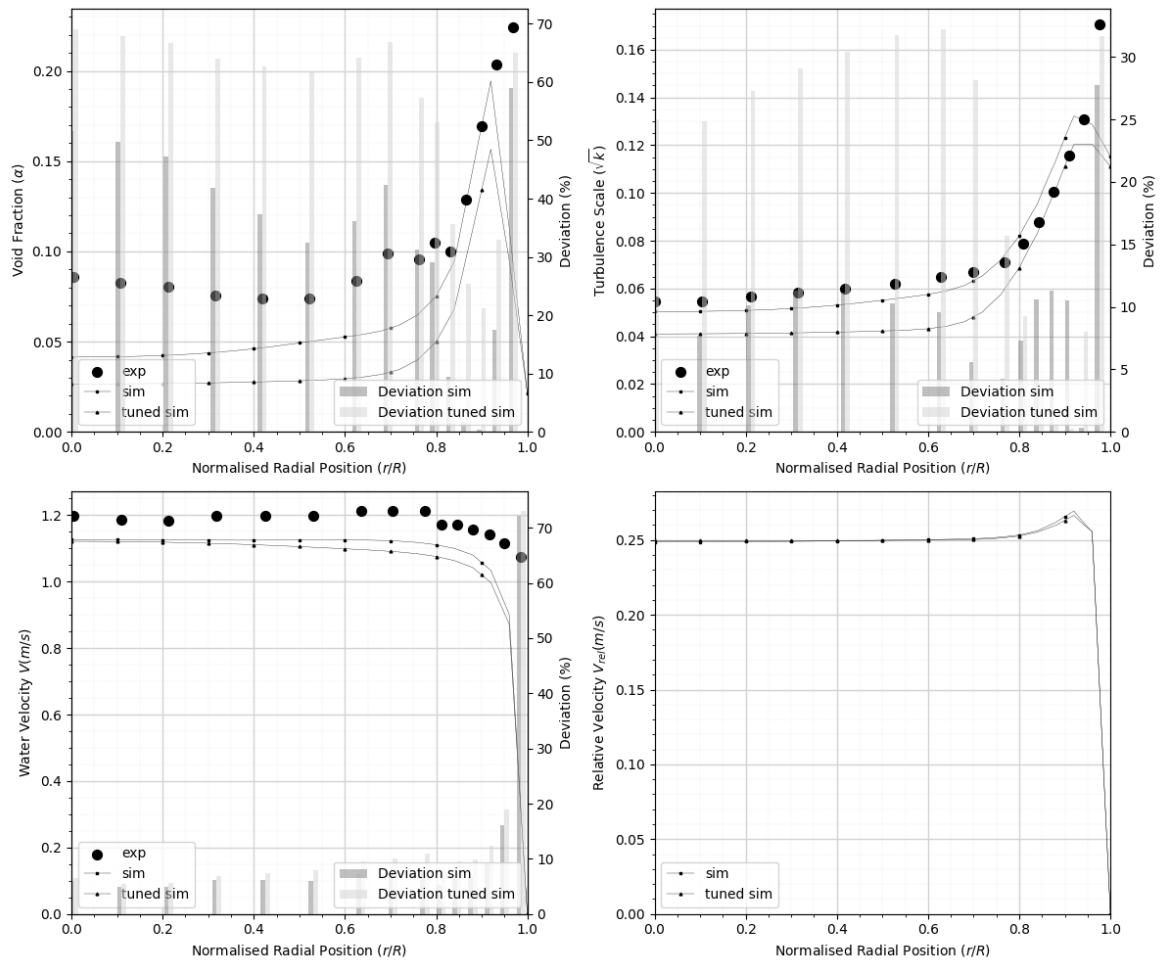


Figure 5.19 L2 results (tuned vs. default sets)

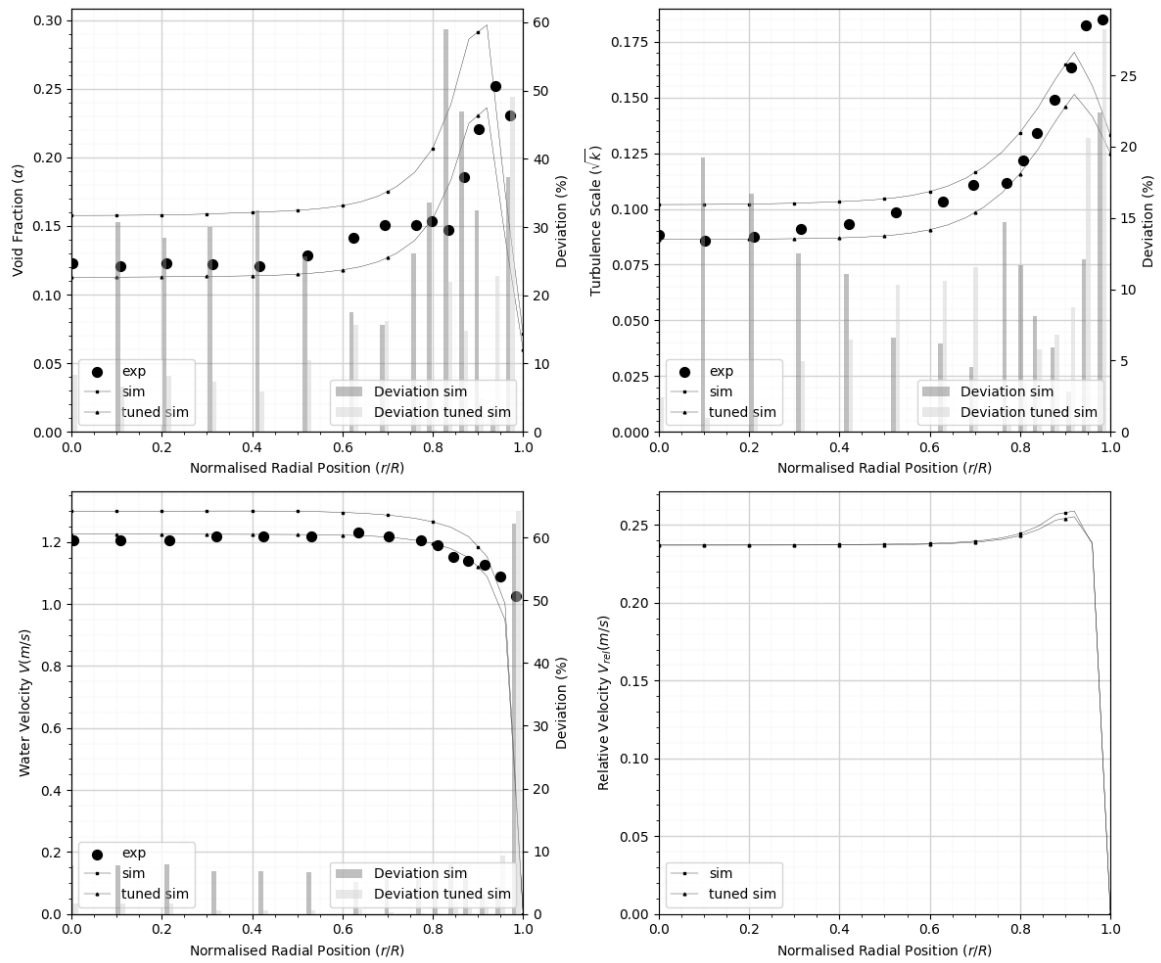


Figure 5.20 L3 results (tuned vs. default sets)

5.4.2. Core Peak

Hosokawa [72] experiment core peak profile cases are presented.

H1-H2 tuning

	n	σ_α	C_{w1}	C_{w2}	C_3	C_{CF}	P
baseline	0	1	-0.01	0.05	0.45	1	-
tuned	-12.6	0.69	-0.035	0.5	0.3	1.82	-3.89

Table 5.5 Baseline vs. tuned model parameters for H1-H2

Baseline performance value is not present due to the fact that the use of default values for the simultaneous simulations of H1 and H2 resulted successfully but tagged in-feasible, where the feasibility condition was set as the maximum value of 0.1 for α at the wall boundary of the axial position of the measurement stations.

Fig. 5.21 presents the tuned coefficient set for H1 obtained from simultaneous simulations of H1 and H2.

Fig. 5.22 presents the tuned coefficient set for H2 obtained from simultaneous simulations of H1 and H2.

The overall results indicate the general applicability of a randomly selected readily available momentum closure model set with tunable parameters may not be possible.

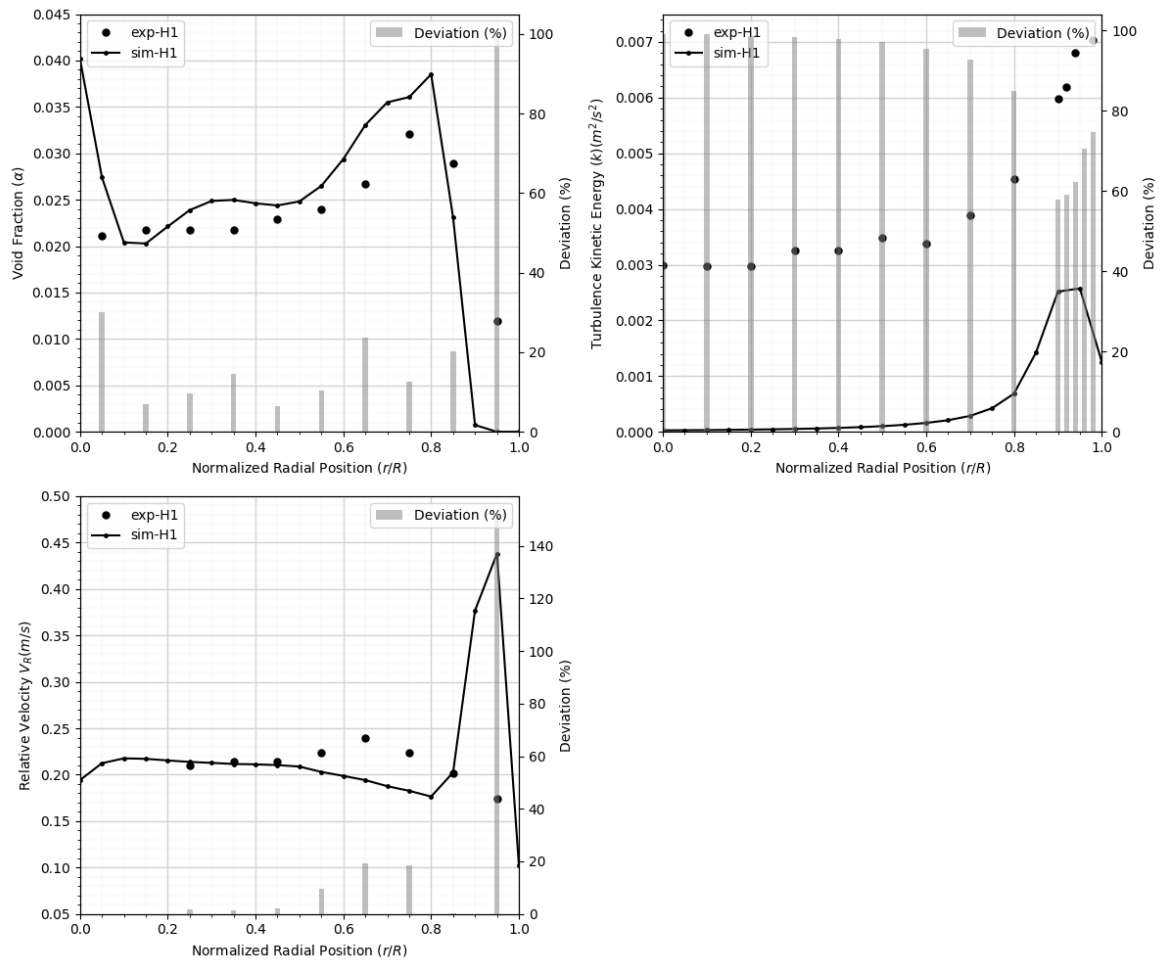


Figure 5.21 H1 tuned coefficient results (H1-H2)

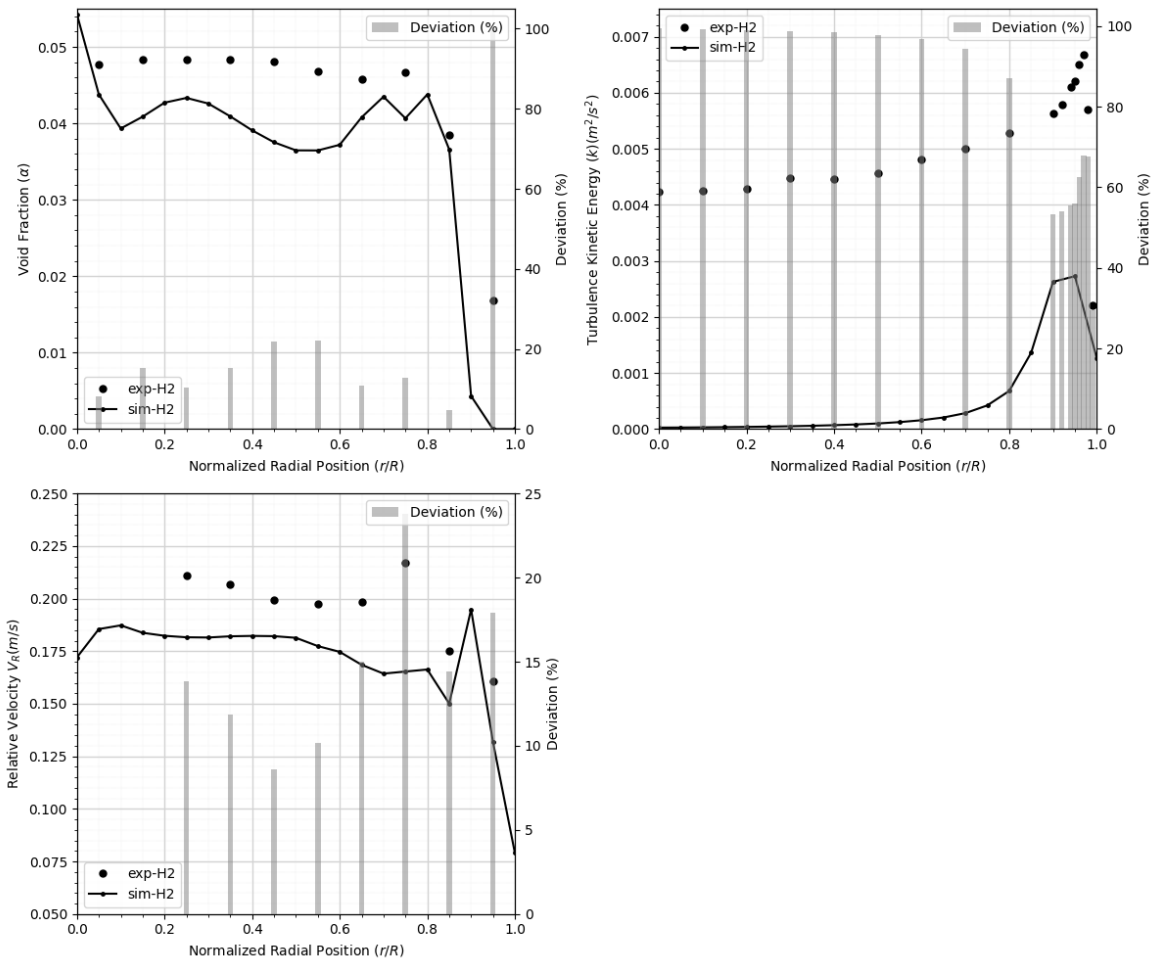


Figure 5.22 H2 tuned coefficient results (H1-H2)

6. MODEL DEVELOPMENT AND VALIDATION

6.1. Model Description

The research focused on developing models specifically for drag coefficient and lift coefficient in bubbly two-phase upward flow conditions. The theoretical foundation was based on single bubble drag and lift coefficients. Data from relevant experiments previously reviewed in the dissertation are used as reference. The power law functional form as shown below in Eq.(215) is considered for the relevant parts of the proposed models. A novel methodological approach was adopted, utilizing an efficient search algorithm to identify and fine-tune unknown constants in the proposed functional forms of drag and lift coefficient models. This approach allowed for a more precise and adaptive model development, capable of accounting for a wide range of variables.

$$f_{\gamma} = C_{\gamma 1} \gamma^{C_{\gamma 2}} \quad (215)$$

To achieve the best-performing models, it is essential to develop and validate against a wide array of reference experiments, covering a broad spectrum of flow conditions. A complete model should account for all the dimensionless numbers and flow-dependent variables such as, Re_b , rotational Reynolds number Re_{ω} , void fraction α , bubble size d , turbulent kinetic energy k , E_o , E_{o_d} , the Weber number We and so forth. The addition of these parameters would help the models to capture more complex interactions within the flow.

The coefficient model, which integrate the effects of multiple parameters, is presented below in Eq.(216) as;

$$C = C_0 \cdot f_{Re_b} \cdot f_{\alpha} \cdot f_{Re_{\omega}} \cdot f_d \cdot f_k \cdot f_{E_o} \cdot f_{E_{o_d}} \cdot f_{We} \cdot \dots \quad (216)$$

Such models are expected to offer a significant improvement in predictive capability for a broader range of conditions.

In this study, relatively simplified versions of the models are proposed and the FAD F_{TD} model is used as is with the new set in certain cases and the effect is observed.

Regarding the drag coefficient model, rotational Reynolds number Re_ω and the swarm effect is also considered besides the bubble Reynolds number, Re_b . Although function constants for Re_b part in most of the already available coefficient models are widely accepted and utilized, as an additional indicator of the performance of the exploration procedure, these constants are also set to be explored with the new coefficient model.

The proposed drag coefficient model with integrated effects can be represented as;

$$C_D = C_{D0} \cdot f_{Re} \cdot f_\alpha \cdot f_{Re_\omega} \quad (217)$$

where,

$$C_{D0} = \frac{24}{Re} \quad (218)$$

The lift coefficient model is proposed with Re_b and swarm effect dependencies. Additionally, since the rotational Reynolds number Re_ω is implicitly including the wall effects through steep change in value with wall distance, it is also included to capture the related effects. This form of the model is to handle the dynamics without the need of any near wall correction model.

The proposed lift coefficient model is presented below as;

$$C_L = C_{L0} \cdot f_{Re} \cdot f_\alpha \cdot f_{Re_\omega} \quad (219)$$

where,

$$C_{L0} = C_1 \quad (220)$$

The limits and the resolution of the coefficients are presented below in Table 6.1,

min	variable	max	resolution
-5	$C_{\alpha 2}^D$	5	101
0.1	$C_{Re_{b1}}^D$	1	101
0.1	$C_{Re_{b2}}^D$	1	101
0	$C_{Re_{\omega 2}}^D$	1	101
0.005	C_1^L	0.5	101
-5	$C_{\alpha 2}^L$	5	101
0	$C_{Re_{b1}}^L$	1	101
0	$C_{Re_{b2}}^L$	10	101
0	$C_{Re_{\omega 1}}^L$	1	101
0	$C_{Re_{\omega 2}}^L$	1	101

Table 6.1 Limits for the new model coefficients

6.2. Wall Peak

Wall peak profile cases of Hosokawa [72] and Serizawa al. [76], [77], [78] are examined and related coefficient model constants are determined in a single and grouped fashion and presented for the respective cases.

6.2.1. S1 new model set

The single S1 experiment of Serizawa al. [76], [77], [78] is chosen for determining the coefficients. Only the lift and drag forces are used and no turbulence related force or model is used. The search procedure is set only against the radial distribution of the volume fraction.

The results for the model parameter search against the single experiment, S1 are presented in Fig. 6.1 and the model constants are shown in Table 6.2. As expected, while good fit is

$C_{\alpha 1}^D$	$C_{Re_b 1}^D$	$C_{Re_b 2}^D$	$C_{Re_\omega 1}^D$	C_0^L	$C_{\alpha 1}^L$	$C_{Re_b 2}^L$	$C_{Re_b 1}^L$	$C_{Re_\omega 1}^L$	$C_{Re_\omega 2}^L$
0.70	0.81	0.71	0.4	0.12	-0.6	6.64	0.29	0.8	0.19

Table 6.2 Model coefficients for S1

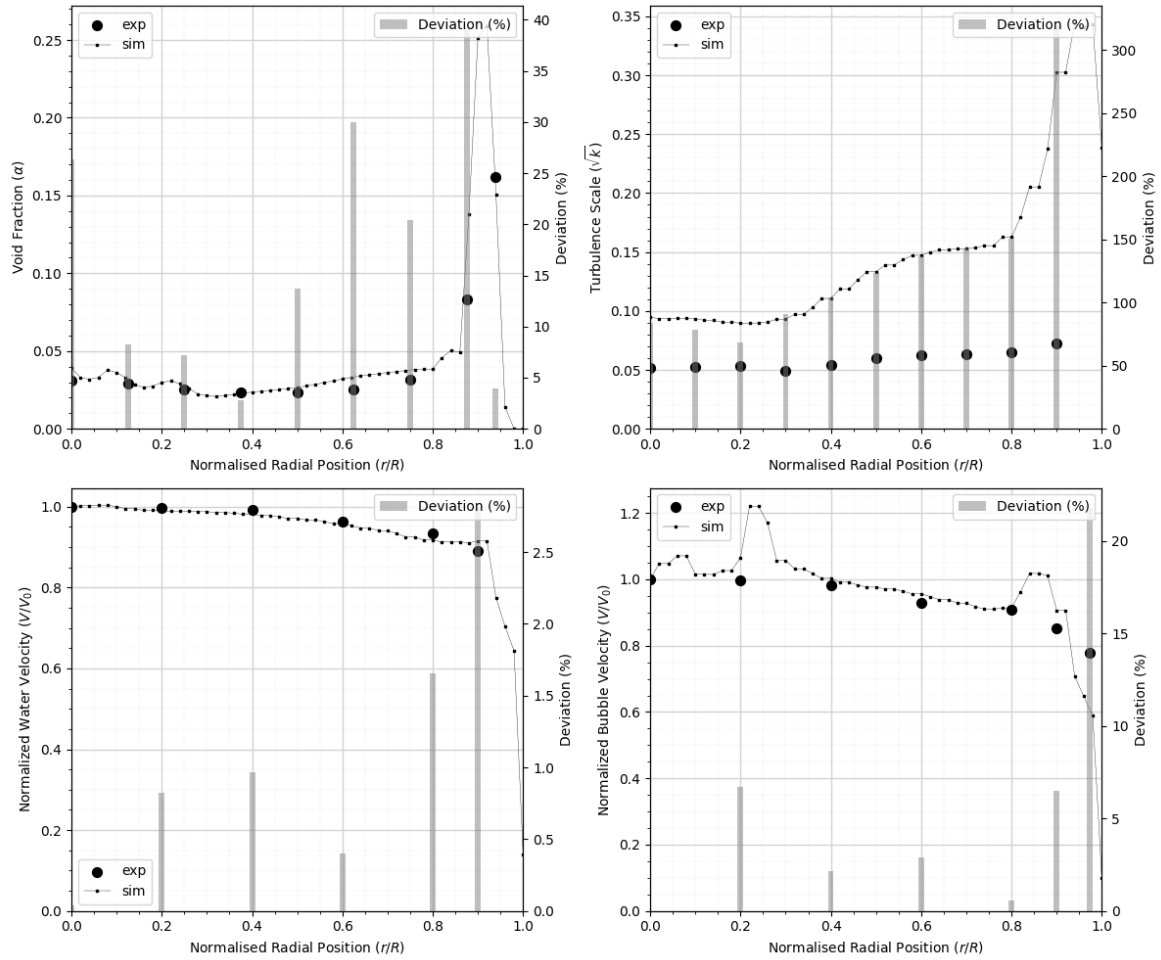


Figure 6.1 S1 (new model sets)

achieved against the volume fraction profile, relatively higher deviation is observed for the turbulence scale. It is also noted that the coefficients for the Re_b part of the drag coefficient model appear to be in good agreement with the readily available alternative models.

6.2.2. S1-S2-S3 new model set

The three experiments of Serizawa al. [76], [77], [78] referred to as S1-S2-S3 are chosen for determining the coefficients. A single set of coefficients are investigated for simultaneous application across these cases. Only the lift and drag forces were considered, with no turbulence-related forces or models included. The search procedure focused solely on the radial distribution of the volume fraction.

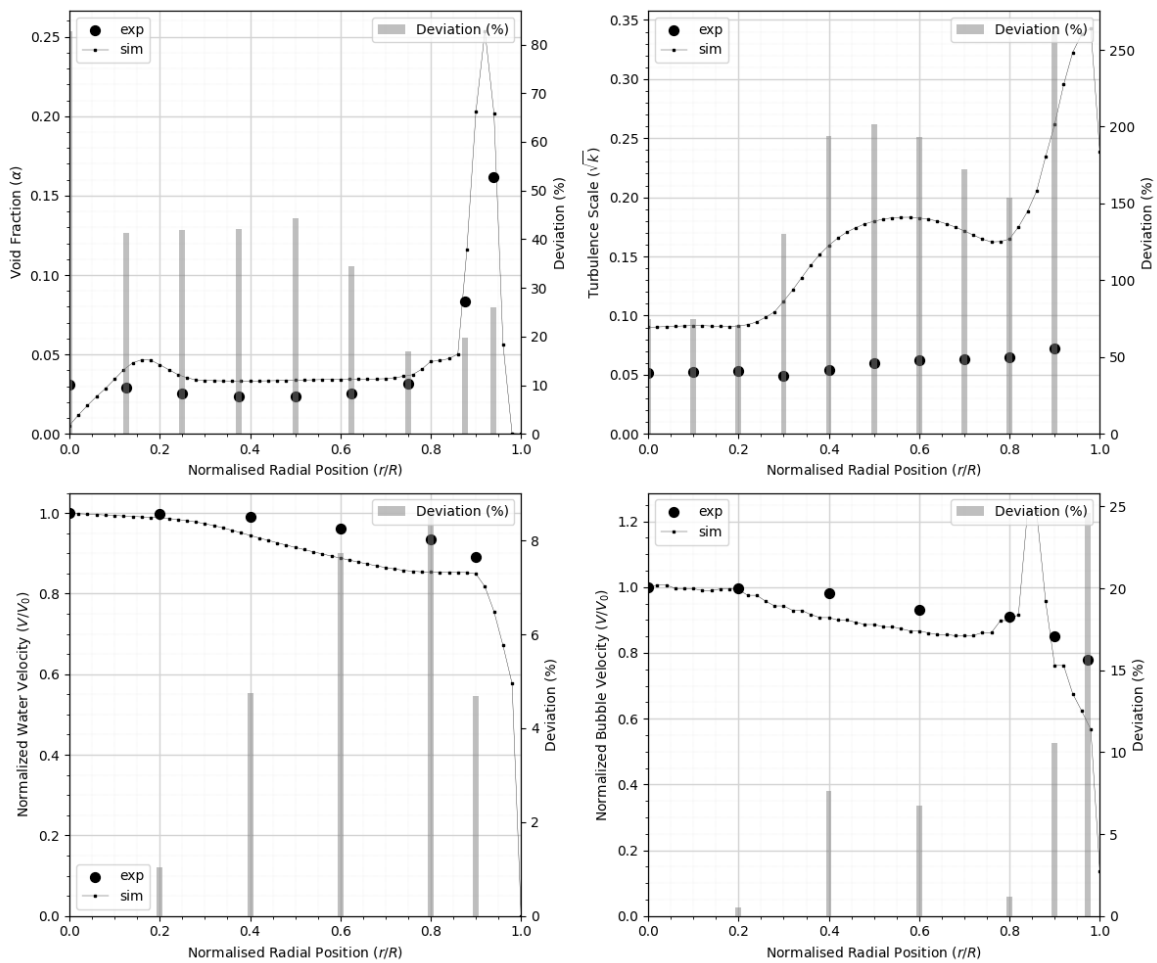


Figure 6.2 S1 model coefficient results (S1-S2-S3)

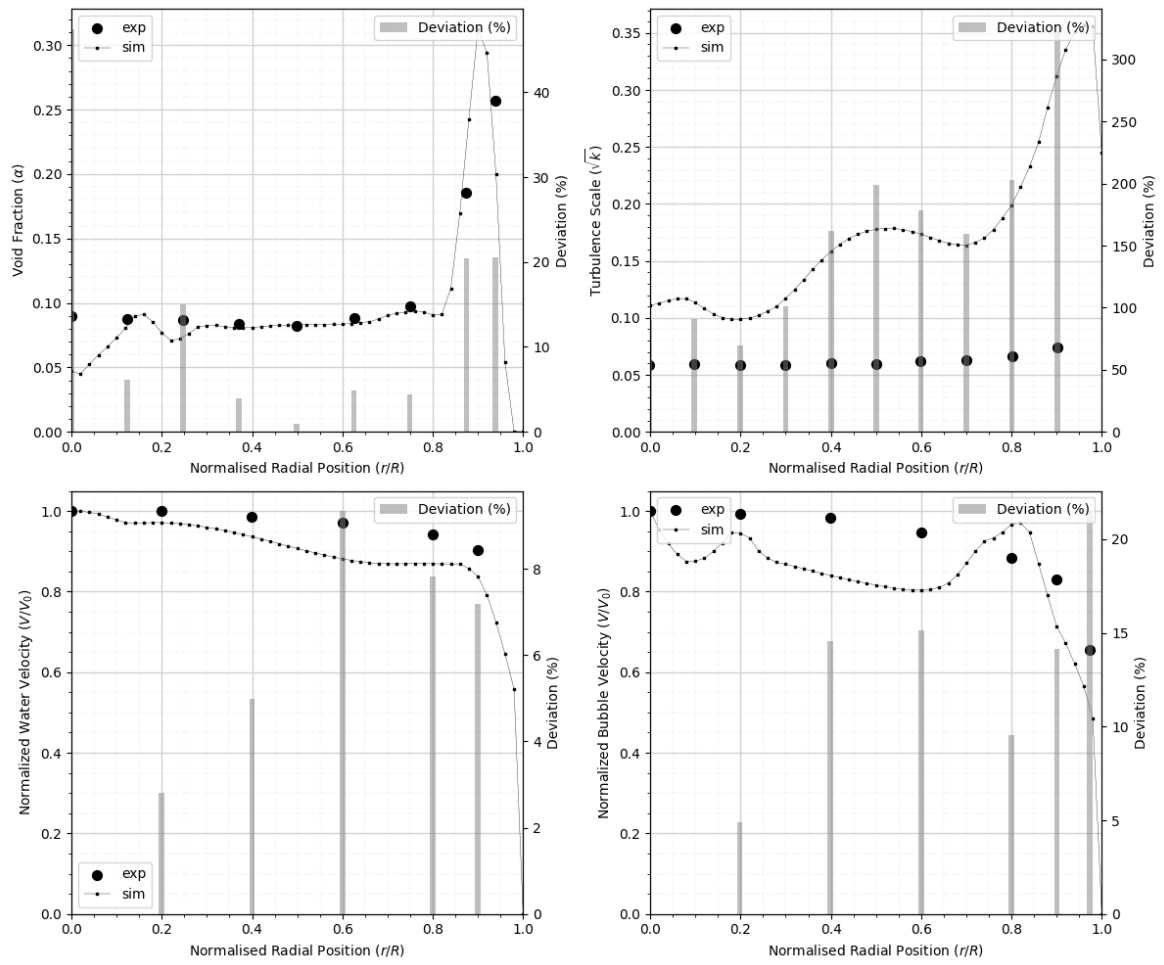


Figure 6.3 S2 model coefficient results (S1-S2-S3)

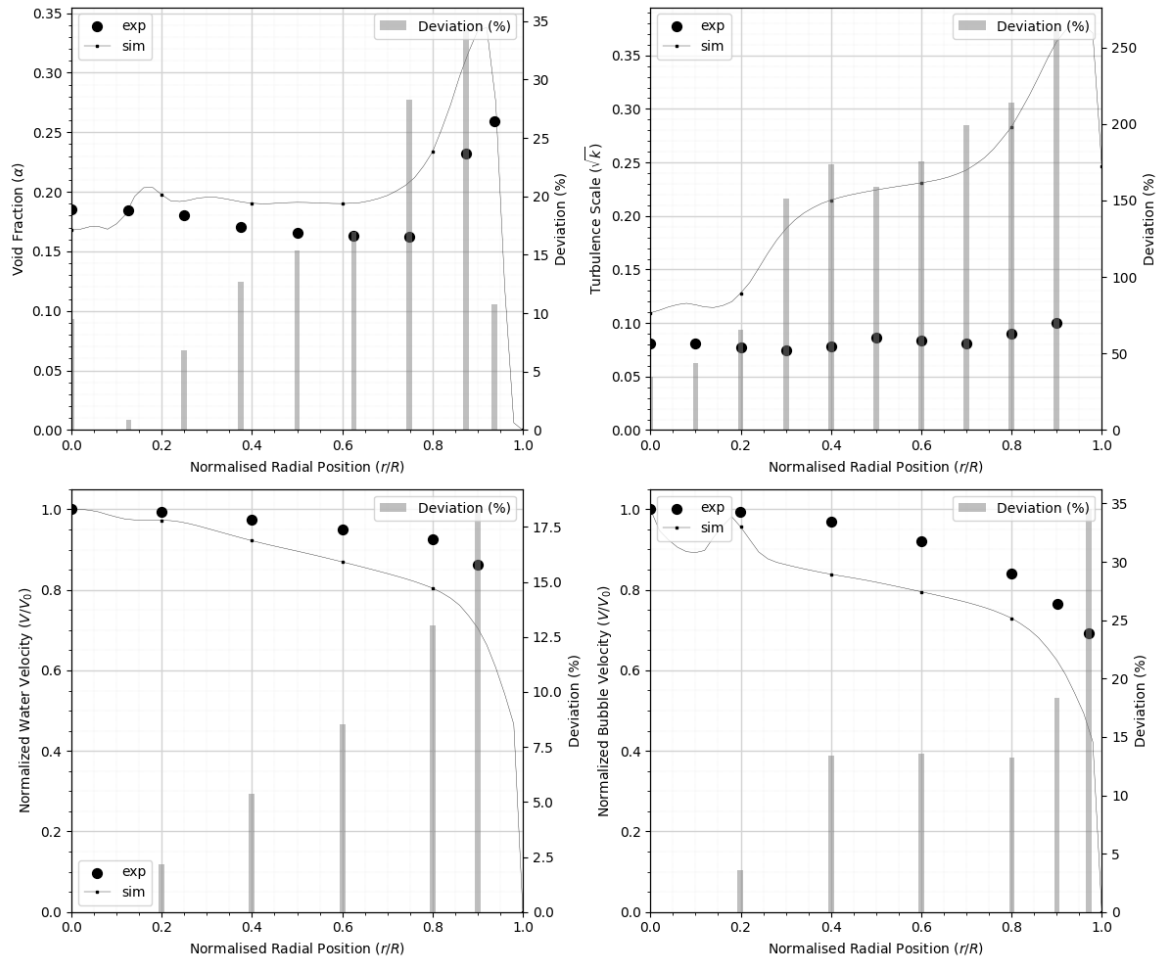


Figure 6.4 S3 model coefficient results (S1-S2-S3)

The results for the model parameter search against multiple experiments, i.e. S1-S2-S3 are presented in Figs (6.2, 6.3, 6.4) and the model constants are shown in Table 6.3. While good agreement for the void fraction profiles were achieved, omitting turbulence related models and forces resulted in poor prediction of turbulence scales.

$C_{\alpha 1}^D$	C_{Reb1}^D	C_{Reb2}^D	$C_{Re\omega 1}^D$	C_0^L	$C_{\alpha 1}^L$	C_{Reb2}^L	C_{Reb1}^L	$C_{Re\omega 1}^L$	$C_{Re\omega 2}^L$
-2.2	0.99	0.62	0.3	0.26	4.9	0.26	0.17	0.78	0.16

Table 6.3 Model coefficients for S1-S2-S3

6.2.3. S1-S2-S3 new model set (F_{TD} and BIT)

The three experiments of Serizawa al. [76], [77], [78] referred to as S1-S2-S3 are chosen for determining the coefficients. A single set of coefficients are investigated for simultaneous application across these cases. Besides the lift and drag forces, F_{TD} and BIT are also considered to enhance turbulence scale prediction. The search procedure focused solely on the radial distribution of the volume fraction.

FAD turbulent dispersion force model included simulation results for the model parameter search against multiple experiments, i.e. S1-S2-S3 are presented in Figs (6.5, 6.6, 6.7) and the model constants are shown in Table 6.4. As expected, the void fraction profiles are smoothed out and the turbulence scale prediction is relatively enhanced. It is also noted that the coefficients for the Re_b part of the drag coefficient model appear to be in good agreement with the readily available alternative models. Addition of the F_{TD} & BIT) affected the swarm and Re_w parts of the coefficient model. While a sign change and increase in amplitude is observed for the swarm part, compared against single and grouped cases respectively, coefficient for Re_w approached to zero.

$C_{\alpha 1}^D$	$C_{Re_b 1}^D$	$C_{Re_b 2}^D$	$C_{Re_w 1}^D$	C_0^L	$C_{\alpha 1}^L$	$C_{Re_b 2}^L$	$C_{Re_b 1}^L$	$C_{Re_w 1}^L$	$C_{Re_w 2}^L$	σ_T
-3.1	0.58	0.41	0	0.097	4.4	0.64	0.21	1	0.02	0.06

Table 6.4 Model coefficients for S1-S2-S3 (F_{TD} & BIT)

C_3	C_{CF}
0.27	0.96

Table 6.5 BIT coefficients for S1-S2-S3

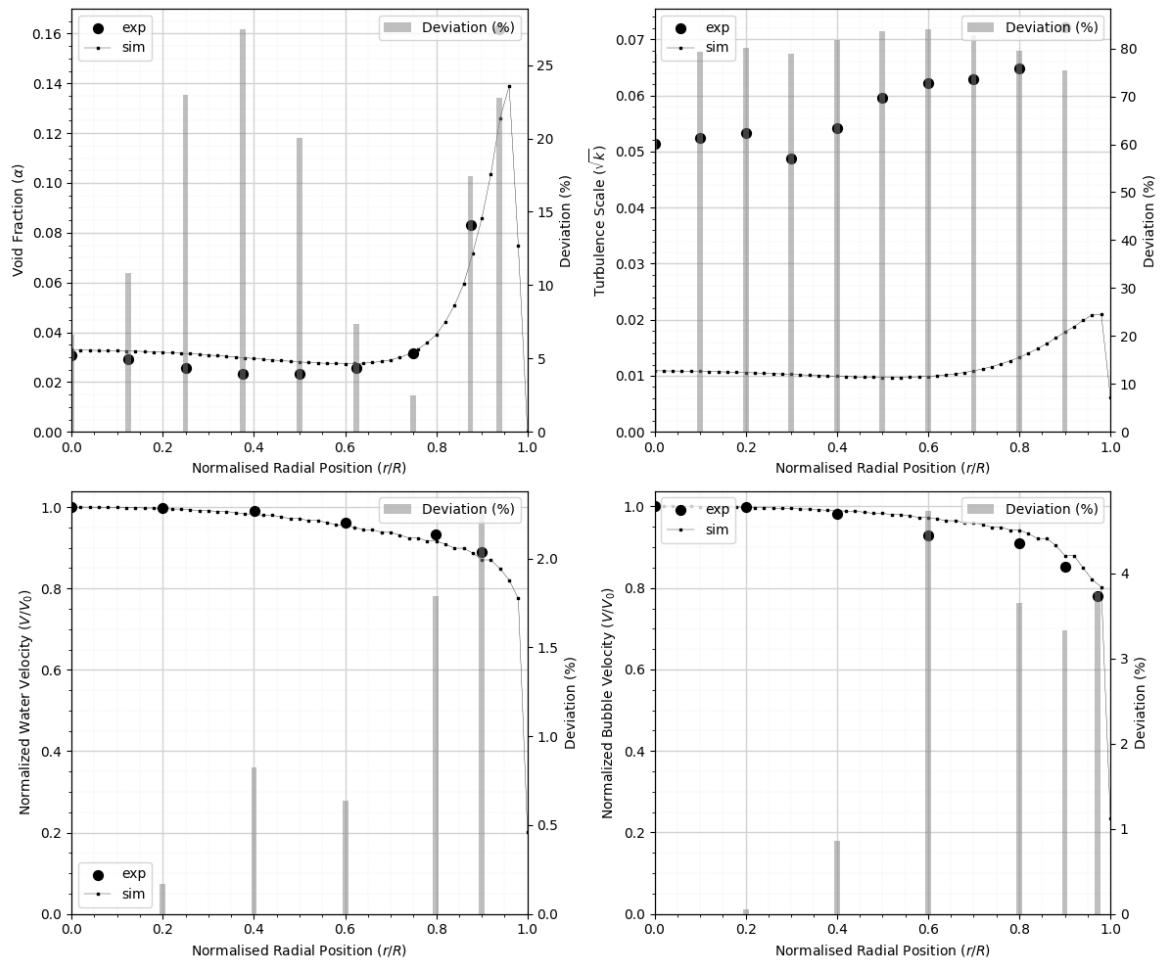


Figure 6.5 S1 model coefficient results (S1-S2-S3) (F_{TD} & BIT)

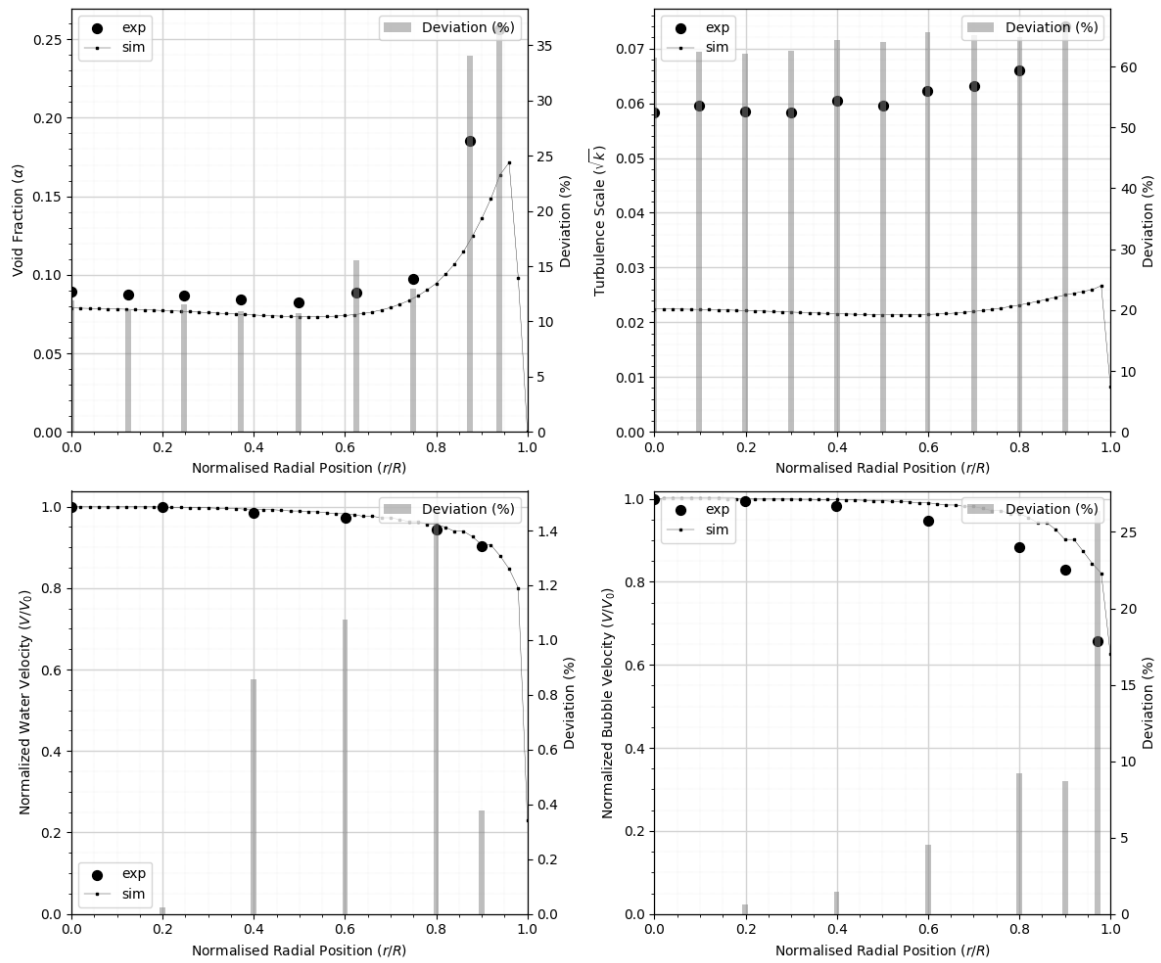


Figure 6.6 S2 model coefficient results (S1-S2-S3) (F_{TD} & BIT)

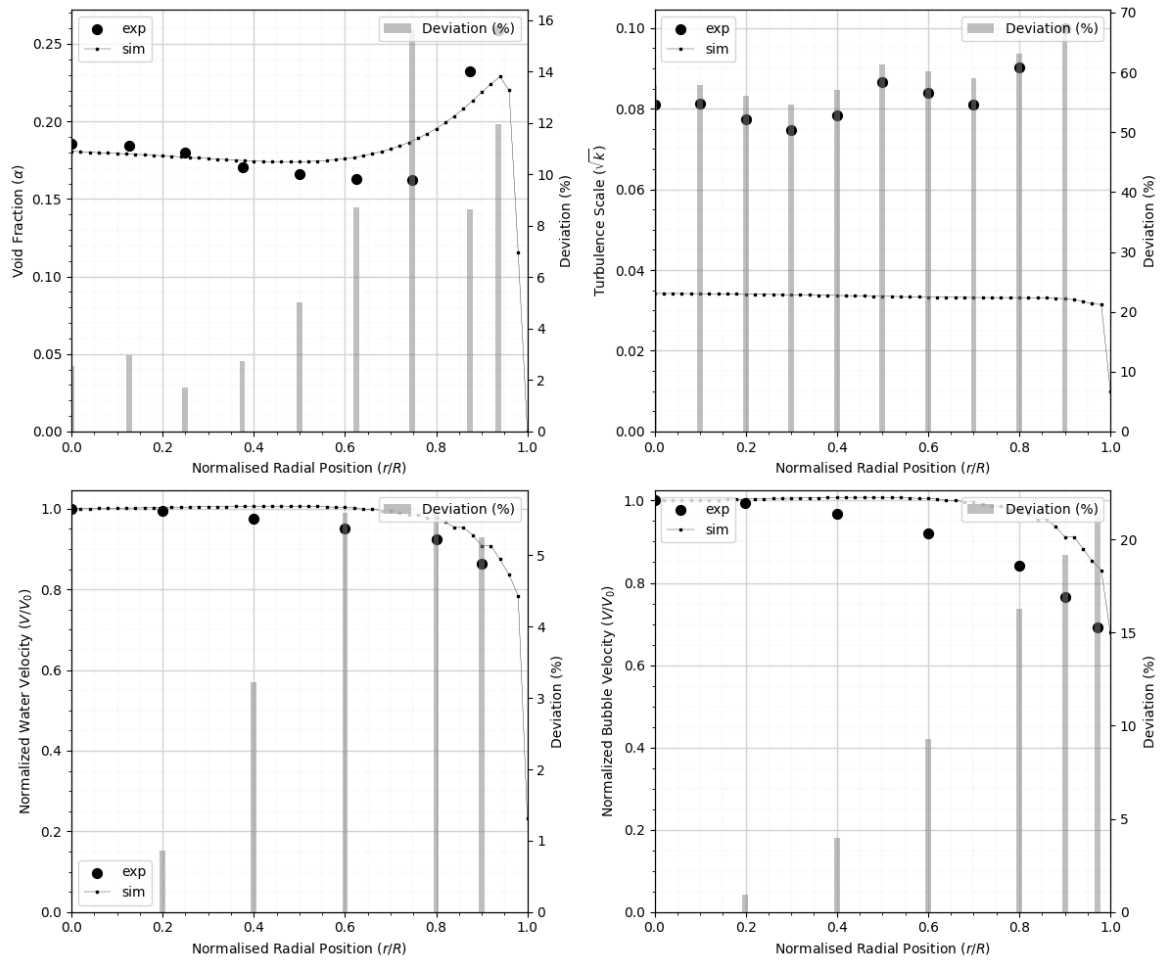


Figure 6.7 S3 model coefficient results (S1-S2-S3) (F_{TD} & BIT)

6.2.4. H3-H4 new model set

Wall peak profile cases H3-H4 of Hosokawa [72] are chosen for determining the coefficients. A single set of coefficients are investigated for simultaneous application across these cases. Besides the lift and drag forces, F_{TD} and BIT are also considered.

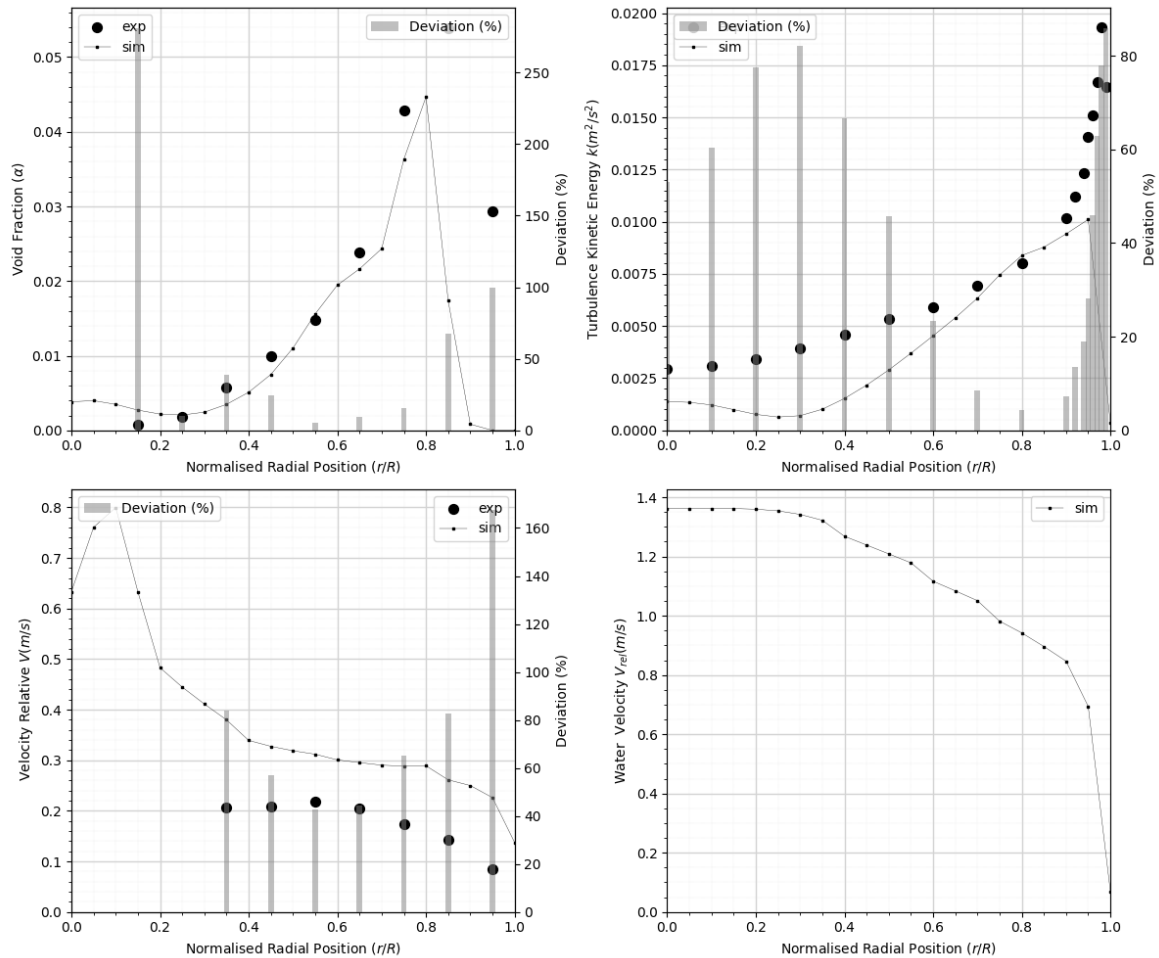


Figure 6.8 H3 model coefficients (F_{TD} & BIT)

The results for the model parameter search against multiple experiments, Figs (6.8-6.9) and the model coefficients are shown in Tables 6.6, 6.7. While a relatively good prediction is achieved, it is observed that the deviation is still significant.

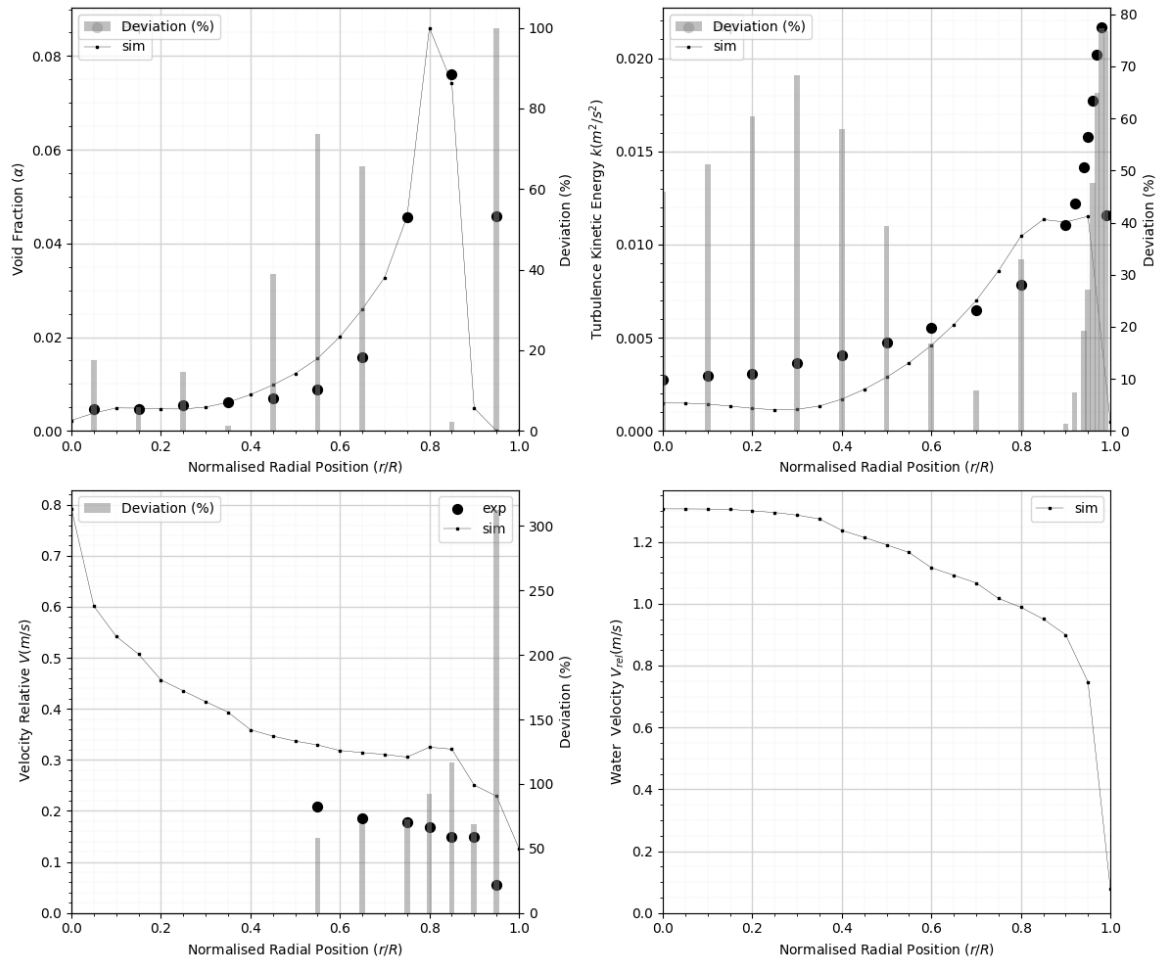


Figure 6.9 H4 model coefficients (F_{TD} & BIT)

C_{Reb1}^D	C_{Reb2}^D	$C_{\alpha1}^D$	$C_{Re\omega1}^D$	C_0^L	$C_{\alpha1}^L$	C_{Reb2}^L	C_{Reb1}^L	$C_{Re\omega1}^L$	$C_{Re\omega2}^L$
0.8	0.65	1.95	0.17	0.2	0.0181	2.5	0.2	0.8	0.9

Table 6.6 Model coefficients for H3-H4 (F_{TD} & BIT)

C_3	C_{CF}
0.36	9.7

Table 6.7 BIT coefficients for H3-H4

6.3. Core Peak

Core peak case of Hosokawa [72] experiment is examined and related coefficient model constants are determined for the respective case.

6.3.1. H2 new model set

Table 6.8, 6.9 presents the model coefficients. As expected, there is a notable change in the coefficients, specifically the parts of the lift coefficient, reason being the radical change in the peak profile.

$C_{\alpha 1}^D$	$C_{Re_{b1}}^D$	$C_{Re_{b2}}^D$	$C_{Re_{\omega 1}}^D$	C_0^L	$C_{\alpha 1}^L$	$C_{Re_{b2}}^L$	$C_{Re_{b1}}^L$	$C_{Re_{\omega 1}}^L$	$C_{Re_{\omega 2}}^L$
-2.73	1	0.90	0.24	0.18	0.05	0.31	0.06	1	0.22

Table 6.8 Model coefficients for H2 with (F_{TD} & BIT)

C_3	C_{CF}
-0.7	0.22

Table 6.9 BIT coefficients for H2 (F_{TD} & BIT)

Fig. 6.10 presents the new coefficient model with the addition of turbulence dispersion force F_{TD} . It is seen that, reasonable prediction is achieved.

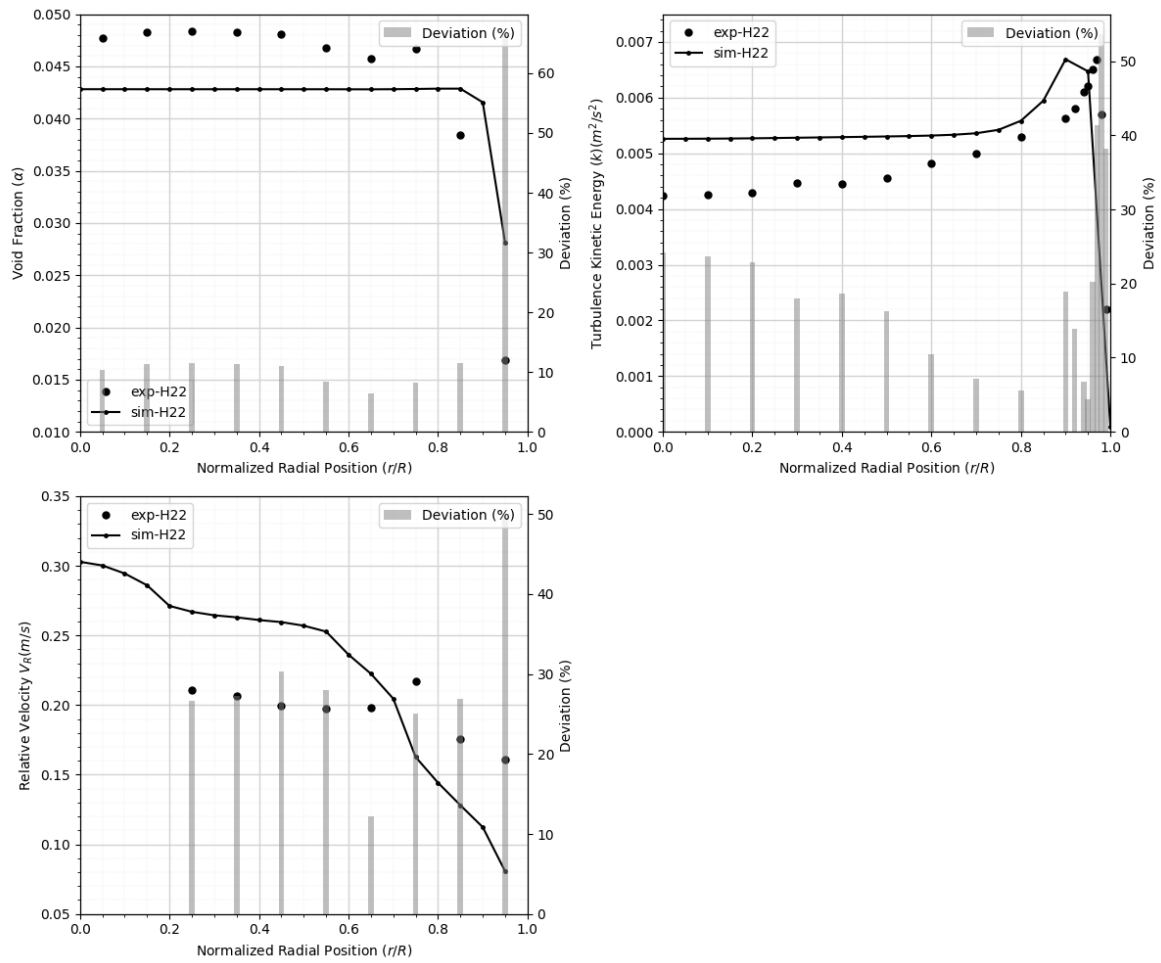


Figure 6.10 H2 model coefficient results (F_{TD} & BIT)

6.4. All Peak

Both wall and core peak cases of Hosokawa [72] experiments are examined and related coefficient model constants are determined for the respective cases. For the assessment of the performance of the proposed coefficient model set, tuned coefficients achieved earlier are referenced for comparison.

6.4.1. H1-H2-H3-H4 new model vs. tuned set

Table 6.10, 6.11 presents the model coefficient set, model BIT coefficients and tuning parameters for the simultaneous simulations of all 4 Hosokawa [72] experiment cases which include 2 wall peak and 2 core peak profiles.

$C_{\alpha 1}^D$	$C_{Re_{b1}}^D$	$C_{Re_{b2}}^D$	$C_{Re_{\omega 1}}^D$	C_0^L	$C_{\alpha 1}^L$	$C_{Re_{b2}}^L$	$C_{Re_{b1}}^L$	$C_{Re_{\omega 1}}^L$	$C_{Re_{\omega 2}}^L$
2.5	0.208	0.838	0.2	0.0609	-0.4	0.8	0.11	0.42	0.7

Table 6.10 Model coefficients for H1-H2-H3-H4 with (F_{TD} & BIT)

C_3	C_{CF}
0.838	0.19

Table 6.11 BIT coefficients for H1-H2-H3-H4 with (F_{TD} & BIT)

Fig.s 6.11, 6.12, 6.13 presents the comparison of void fraction distribution, turbulence kinetic energy profile and relative velocity profile predictions of the proposed approach against tuned sets respectively.

The results show considerable prediction performance of the new model, while requiring additional improvements.

This study is conducted for mono-dispersed cases. For further improvement, functions including turbulence kinetic energy, bubble shape, size and aspect ratio should be included.

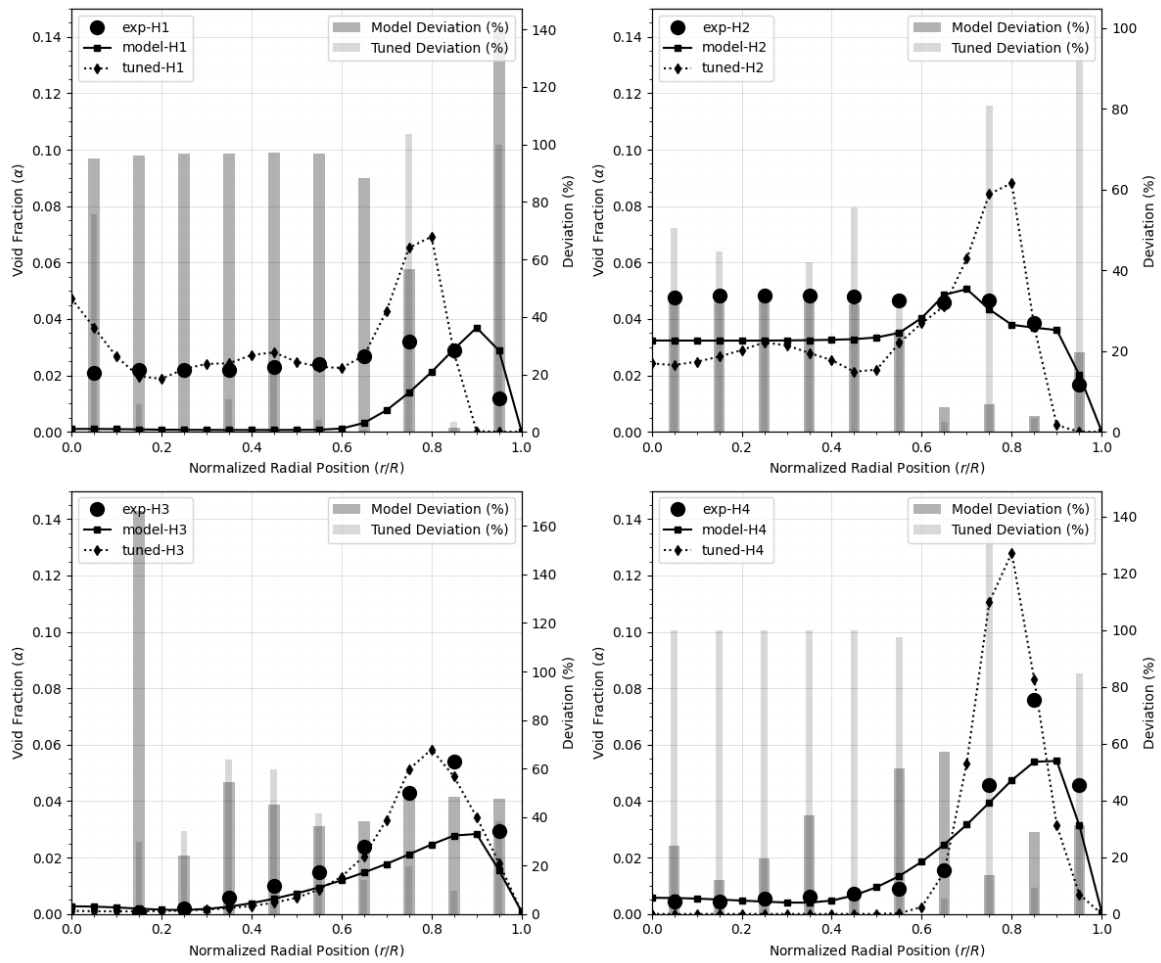


Figure 6.11 H1-H2-H3-H4 new coefficients vs. tuned set (F_{TD} & BIT)

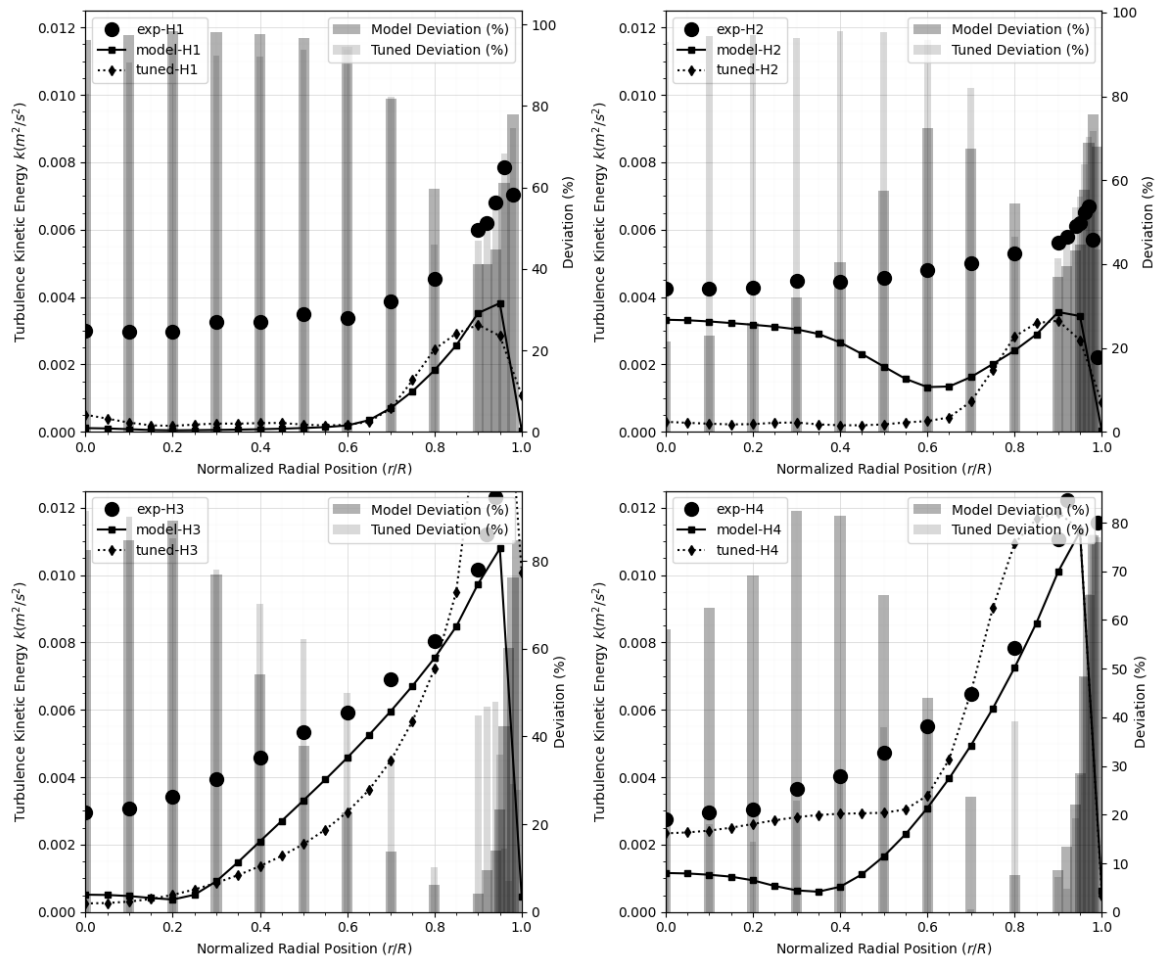


Figure 6.12 H1-H2-H3-H4 new coefficients vs. tuned set (F_{TD} & BIT)

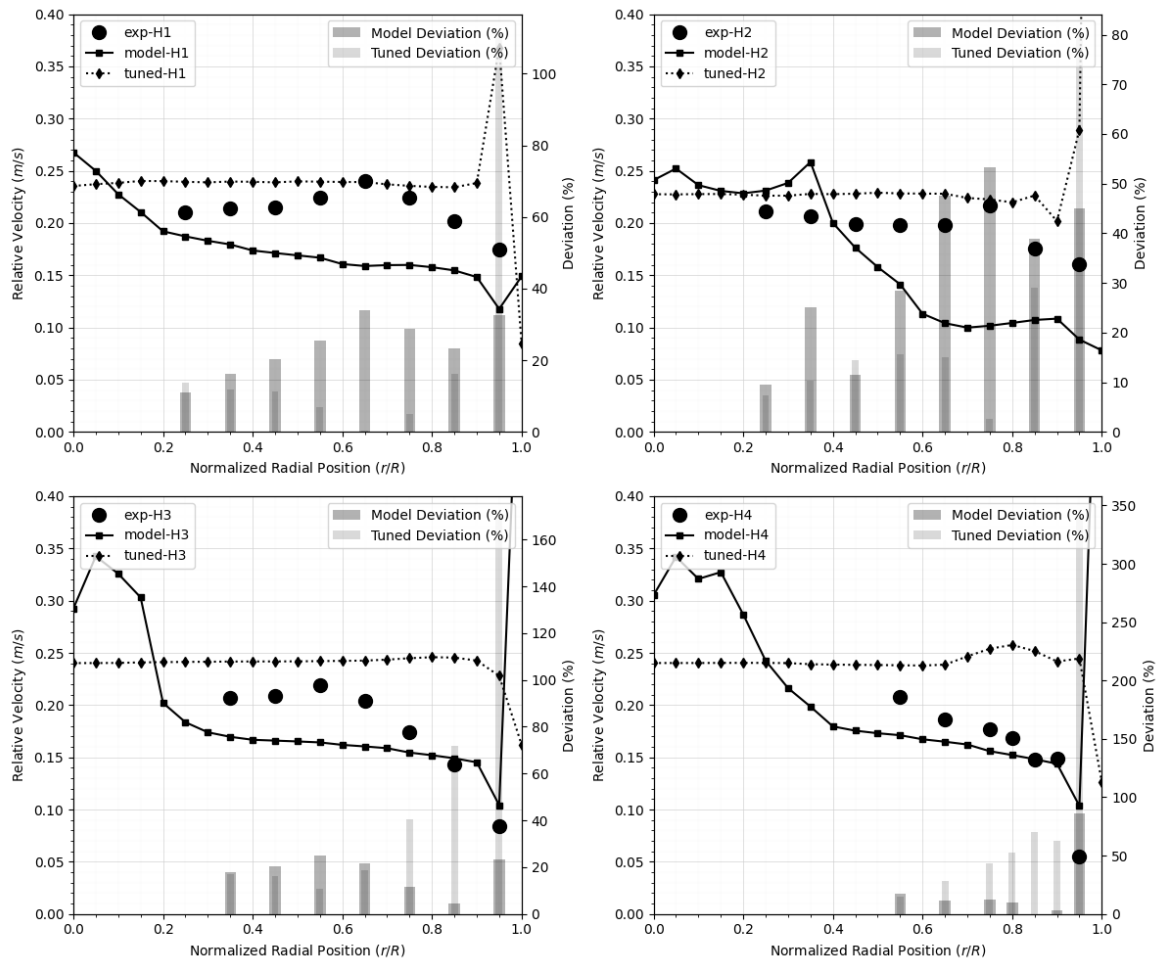


Figure 6.13 H1-H2-H3-H4 new coefficients vs. tuned set (F_{TD} & BIT)

7. DISCUSSION

Current momentum closure models are confined to the particular experimental conditions which they were developed against. By addressing this gap, this study aimed to propose new drag coefficient model and lift coefficient model and determine the model coefficients using design space exploration method. CFD simulations were conducted for validation against experiment data. The proposed drag coefficient and lift coefficient models were formulated with the dependencies on flow dependent parameters such as shear rate, volume fraction and Reynolds number to provide a more robust closure relation. The design space exploration method, aimed to minimize the mismatch between CFD simulation outcomes and experiment measurement data by automatically changing model coefficients.

The exploration process revealed that while the proposed models can be calibrated to match void fraction distributions closely, this alone was insufficient. It is observed that, matching void fraction distributions does not guarantee accurate predictions for other flow variables such as turbulence kinetic energy and continuous and dispersed phase velocities. This shows that relying solely on void fraction distribution data for model calibration leads to significant discrepancies in the rest of the flow parameters. This is also highly coupled with turbulence modeling and may result in inaccuracy. The use of shear rate for the lift model handled the sign change of the lift coefficient, however, further theoretical development is required. Furthermore, two-phase bubbly upward flow in cylindrical pipes can be classified regarding void fraction profiles as wall and core-peaking based on phase velocities, volume fraction profiles, and bubble shape and sizes. Models and constants determined against core peaking experiments did not perform well for wall peaking cases and vice versa. Calibration attempts for both peak types simultaneously resulted in poor performance for both cases. This may highlight the difficulty in developing a generally applicable model. An advantage of the proposed models is, unlike many existing momentum closure models, there are no non-flow parameters such as wall distance or any conditional functions such as bubble size conditions. The proposed models only depends on flow parameters. This simplicity enhances its adaptability and ease of implementation.

Stability issues are common in two-phase flow CFD simulations. To mitigate, smoothing methods and low under-relaxation factors were applied. The turbulence model sensitivity of the proposed coefficient models was another challenge. The choice of turbulence method and turbulence model, and even any additional momentum closure models like the turbulent dispersion model directly affected the performance of the proposed drag and lift models. This dependency shows a limitation in the generality of the proposed models.

For general applicability of the proposed models, future models should consider dependencies on additional flow variables, such as turbulence kinetic energy, void fraction gradient, dispersed phase shape functions and so forth. Smoothing techniques should be considered for stability issues during flow development, particularly until steady-state conditions are achieved.

A coupled or hybrid turbulence and momentum closure model may offer a more robust solution. This would also support general applicability for different turbulence models and flow conditions.

More experimental data spanning a broad range of flow variables representing diverse scenarios are required to improve the calibration and validation of the models. A deeper theoretical examination of the dependent flow variables used in the models, particularly the use of shear rate in the lift model, is needed to ensure mathematical consistency.

The method demonstrated potential for developing more universally applicable momentum closure models. The findings show the importance of data sets for model calibration. The proposed methodology can be applied, but not limited to turbulence modeling for more generalized turbulence closure models.

In summary, this research aimed improvement for the generality of momentum closure models used and applicable in bubbly two-phase flow studies and highlighted the potential and the challenges. Further refinement and validation is required for practical applications.

8. CONCLUSION

This thesis has addressed the complex problem of modeling momentum transfer mechanisms in isothermal bubbly two-phase upward flow in cylindrical pipes and the gap between theoretical predictions and experimental observations.

A novel method of the integration of simulations, for model selection, validation, and development processes with sophisticated design exploration techniques is introduced. This integration enabled automated, optimization process, ensuring a robust and innovative framework for the study. This integration enables more comprehensive exploration of the design space, leading to more precise and reliable closure models.

A new closure set with drag and lift coefficients is proposed for improved representation of the dynamics of momentum transfer mechanisms for isothermal conditions. The proposed set has been successfully integrated into a CFD framework and validated with a comprehensive set of experimental data. The validation process demonstrated improvement in predicting void fraction, while a relatively poor performance of prediction for continuous phase turbulent kinetic energy, phase velocities and relative velocity distribution, against the available reference sets was observed. This set represents an improvement over existing sets, particularly in terms of adaptability to different flow conditions and pipe diameter range of 25-60 mm.

In conclusion, presented approach outlined in this research represents a supplementary method to existing numerical methods in the development of closure models. This method enhances and supports the current numerical techniques used in CFD simulations and is valuable in refining the precision and applicability of closure models. The method not only has the ability to enhance model development and validation, but also has the potential of offering a robust framework that can be adopted to wide ranging challenges in the field of fluid dynamics.

REFERENCES

- [1] Chih-Hung Lin and Takashi Hibiki. Databases of interfacial area concentration in gas–liquid two-phase flow. *Progress in Nuclear Energy*, 74:91–102, **2014**.
- [2] Irfan Khan, Mingjun Wang, Yapei Zhang, Wenxi Tian, Guanghui Su, and Suizheng Qiu. Two-phase bubbly flow simulation using cfd method: A review of models for interfacial forces. *Progress in Nuclear Energy*, 125:103360, **2020**.
- [3] Han Bao, Jinyong Feng, Nam Dinh, and Hongbin Zhang. Computationally efficient cfd prediction of bubbly flow using physics-guided deep learning. *International Journal of Multiphase Flow*, 131:103378, **2020**.
- [4] Han Bao, Jinyong Feng, Nam Dinh, and Hongbin Zhang. Deep learning interfacial momentum closures in coarse-mesh cfd two-phase flow simulation using validation data. *International Journal of Multiphase Flow*, 135:103489, **2021**.
- [5] S Hänsch, I Evdokimov, F Schlegel, and D Lucas. A workflow for the sustainable development of closure models for bubbly flows. *Chemical Engineering Science*, 244:116807, **2021**.
- [6] Mamoru Ishii and Takashi Hibiki. *Thermo-fluid dynamics of two-phase flow*. Springer Science & Business Media, **2010**.
- [7] Rutherford Aris. *Vectors, tensors and the basic equations of fluid mechanics*. Courier Corporation, **2012**.
- [8] Mamoru Ishii. Thermo-fluid dynamic theory of two-phase flow. *NASA Sti/recon Technical Report A*, 75:29657, **1975**.
- [9] Mamoru Ishii and Kaichiro Mishima. Two-fluid model and hydrodynamic constitutive relations. *Nuclear Engineering and design*, 82(2-3):107–126, **1984**.

- [10] Andrei Nikolaevich Kolmogorov. The local structure of turbulence in incompressible viscous fluid for very large reynolds numbers. *Proceedings of the Royal Society of London. Series A: Mathematical and Physical Sciences*, 434(1890):9–13, **1991**.
- [11] Andrei Nikolaevich Kolmogorov. Dissipation of energy in the locally isotropic turbulence. *Proceedings of the Royal Society of London. Series A: Mathematical and Physical Sciences*, 434(1890):15–17, **1991**.
- [12] Uriel Frisch. *Turbulence: the legacy of AN Kolmogorov*. Cambridge university press, **1995**.
- [13] David C. Wilcox. *Turbulence Modeling for CFD*. DCW Industries, La Canada, California, **2006**.
- [14] Steven A Orszag. Analytical theories of turbulence. *Journal of Fluid Mechanics*, 41(2):363–386, **1970**.
- [15] Jean Boussinesq. *Essai sur la théorie des eaux courantes*. Imprimerie nationale, **1877**.
- [16] Theodore Von Kármán. *Mechanical similitude and turbulence*. 611. National Advisory Committee for Aeronautics, **1931**.
- [17] L. Schiller and A. Naumann. A drag coefficient correlation. *Z. Ver. Deutsch. Ing*, 77:318–320, **1935**.
- [18] Mamoru Ishii and Novak Zuber. Drag coefficient and relative velocity in bubbly, droplet or particulate flows. *AIChE Journal*, 25(5):843–855, **1979**.
- [19] Akio Tomiyama, Isao Kataoka, Iztok Zun, and Tadashi Sakaguchi. Drag coefficients of single bubbles under normal and micro gravity conditions. *JSME International Journal Series B Fluids and Thermal Engineering*, 41(2):472–479, **1998**.

- [20] A Tomiyama, GP Celata, S Hosokawa, and S Yoshida. Terminal velocity of single bubbles in surface tension force dominant regime. *International journal of multiphase flow*, 28(9):1497–1519, **2002**.
- [21] I.A. Vakhrushev and G.I. Efremov. Interpolation formula for computing the velocities of single gas bubbles in liquids. *Chemistry and Technology of Fuels and Oils*, 6(5):376 – 379, **1970**. doi:10.1007/BF01171684.
- [22] Philip Geoffrey Saffman. The lift on a small sphere in a slow shear flow. *Journal of fluid mechanics*, 22(2):385–400, **1965**.
- [23] I Žun. The transverse migration of bubbles influenced by walls in vertical bubbly flow. *International Journal of Multiphase Flow*, 6(6):583–588, **1980**.
- [24] T. Auton. The lift on a spherical body in a rotational flow. *Journal of Fluid Mechanics*, 183:199–218, **1987**. doi:10.1017/S002211208700260X.
- [25] D.A. Drew and R.T. Lahey. The virtual mass and lift force on a sphere in rotating and straining inviscid flow. *International Journal of Multiphase Flow*, 13(1):113 – 121, **1987**. ISSN 0301-9322. doi:https://doi.org/10.1016/0301-9322(87)90011-5.
- [26] SK Wang, SJ Lee, OC Jones Jr, and RT Lahey Jr. 3-d turbulence structure and phase distribution measurements in bubbly two-phase flows. *International Journal of multiphase flow*, 13(3):327–343, **1987**.
- [27] Dominique Legendre and Jacques Magnaudet. The lift force on a spherical bubble in a viscous linear shear flow. *Journal of Fluid Mechanics*, 368:81 – 126, **1998**. doi:10.1017/S0022112098001621.
- [28] Akio Tomiyama, Hidesada Tamai, Iztok Zun, and Shigeo Hosokawa. Transverse migration of single bubbles in simple shear flows. *Chemical Engineering Science*, 57(11):1849–1858, **2002**.

- [29] Takashi Hibiki and Mamoru Ishii. Lift force in bubbly flow systems. *Chemical Engineering Science*, 62(22):6457 – 6474, **2007**. ISSN 0009-2509.
- [30] DR Shaver and MZ Podowski. Modeling of interfacial forces for bubbly flows in subcooled boiling conditions. *Trans. Am. Nucl. Soc.(Proc. ANS Winter Mtg.)*, 113:1368, **2015**.
- [31] N. Zuber. On the dispersed two-phase flow in the laminar flow regime. *Chemical Engineering Science*, 19(11):897–917, **1964**. ISSN 0009-2509. doi:[https://doi.org/10.1016/0009-2509\(64\)85067-3](https://doi.org/10.1016/0009-2509(64)85067-3).
- [32] M Ishii and K Mishima. Study of two-fluid model and interfacial area. Technical report, Argonne National Lab., IL (USA), **1980**.
- [33] Martin Aurelio Lopez de Bertodano. *Turbulent bubbly two-phase flow in a triangular duct*. Rensselaer Polytechnic Institute, **1992**.
- [34] R.T. Lahey, M. Lopez de Bertodano, and O.C. Jones. Phase distribution in complex geometry conduits. *Nuclear Engineering and Design*, 141(1):177–201, **1993**. ISSN 0029-5493. doi:[https://doi.org/10.1016/0029-5493\(93\)90101-E](https://doi.org/10.1016/0029-5493(93)90101-E).
- [35] D.A. Drew. A turbulent dispersion model for particles or bubbles. *Journal of Engineering Mathematics*, 41(2-3):259 – 274, **2001**. doi:10.1023/A:1011901711594.
- [36] Dirk Lucas, Eckhard Krepper, and Horst-Michael Prasser. Prediction of radial gas profiles in vertical pipe flow on the basis of bubble size distribution. *International Journal of Thermal Sciences*, 40(3):217–225, **2001**. ISSN 1290-0729. doi:[https://doi.org/10.1016/S1290-0729\(00\)01211-4](https://doi.org/10.1016/S1290-0729(00)01211-4).
- [37] Alan D Burns, Thomas Frank, Ian Hamill, Jun-Mei Shi, et al. The favre averaged drag model for turbulent dispersion in eulerian multi-phase flows. In *5th international conference on multiphase flow, ICMF*, volume 4, pages 1–17. ICMF, **2004**.

- [38] S.P. Antal, R.T. Lahey, and J.E. Flaherty. Analysis of phase distribution in fully developed laminar bubbly two-phase flow. *International Journal of Multiphase Flow*, 17(5):635 – 652, **1991**. ISSN 0301-9322. doi:[https://doi.org/10.1016/0301-9322\(91\)90029-3](https://doi.org/10.1016/0301-9322(91)90029-3).
- [39] A. Tomiyama, A. Sou, I. Zun, N. Kanami, and T. Sakaguchi. Effects of eötvös number and dimensionless liquid volumetric flux on lateral motion of a bubble in a laminar duct flow. In Akimi Serizawa, Tohru Fukano, and Jean Bataille, editors, *Multiphase Flow 1995*, pages 3–15. Elsevier, Amsterdam, **1995**. ISBN 978-0-444-81811-9. doi:<https://doi.org/10.1016/B978-0-444-81811-9.50005-6>.
- [40] Shigeo Hosokawa, Akio Tomiyama, Shinji Misaki, and Tomoyuki Hamada. Lateral migration of single bubbles due to the presence of wall. In *Fluids Engineering Division Summer Meeting*, volume 36150, pages 855–860. **2002**.
- [41] Eckhard Krepper, Dirk Lucas, and Horst-Michael Prasser. On the modelling of bubbly flow in vertical pipes. *Nuclear Engineering and Design*, 235(5):597–611, **2005**. ISSN 0029-5493. doi:<https://doi.org/10.1016/j.nucengdes.2004.09.006>.
- [42] Thomas Frank. Advances in computational fluid dynamics (cfd) of 3-dimensional gas-liquid multiphase flows. In *NAFEMS Seminar: Simulation of Complex Flows (CFD)–Applications and Trends, Wiesbaden, Germany, Citeseer*, pages 1–18. **2005**.
- [43] Th. Frank, P.J. Zwart, E. Krepper, H.-M. Prasser, and D. Lucas. Validation of cfd models for mono- and polydisperse air-water two-phase flows in pipes. *Nuclear Engineering and Design*, 238(3):647 – 659, **2008**. ISSN 0029-5493. doi:<https://doi.org/10.1016/j.nucengdes.2007.02.056>. Benchmarking of CFD Codes for Application to Nuclear Reactor Safety.
- [44] Roland Rzehak, Eckhard Krepper, and Conxita Lifante. Comparative study of wall-force models for the simulation of bubbly flows. *Nuclear Engineering*

and Design, 253:41–49, **2012**. ISSN 0029-5493. doi:<https://doi.org/10.1016/j.nucengdes.2012.07.009>. SI : CFD4NRS-3.

- [45] Nazar Lubchenko, Ben Magolan, Rosie Sugrue, and Emilio Baglietto. A more fundamental wall lubrication force from turbulent dispersion regularization for multiphase cfd applications. *International Journal of Multiphase Flow*, 98:36 – 44, **2018**. ISSN 0301-9322. doi:<https://doi.org/10.1016/j.ijmultiphaseflow.2017.09.003>.
- [46] L Prandtl. A report on testing for built-up turbulence. *Z. Angew. Math. Mech*, 5:136–139, **1925**.
- [47] Edward R Van Driest. On turbulent flow near a wall. *Journal of the aeronautical sciences*, 23(11):1007–1011, **1956**.
- [48] B.E. Launder and D.B. Spalding. The numerical computation of turbulent flows. *Computer Methods in Applied Mechanics and Engineering*, 3(2):269–289, **1974**. ISSN 0045-7825. doi:[https://doi.org/10.1016/0045-7825\(74\)90029-2](https://doi.org/10.1016/0045-7825(74)90029-2).
- [49] Philip Geoffrey Saffman. A model for inhomogeneous turbulent flow. *Proceedings of the Royal Society of London. A. Mathematical and Physical Sciences*, 317(1530):417–433, **1970**.
- [50] Florian R Menter. Two-equation eddy-viscosity turbulence models for engineering applications. *AIAA journal*, 32(8):1598–1605, **1994**.
- [51] W Rodi. A new algebraic relation for calculating the reynolds stresses. In *Gesellschaft Angewandte Mathematik und Mechanik Workshop Paris France*, volume 56, page 219. **1976**.
- [52] Stephen B Pope. A more general effective-viscosity hypothesis. *Journal of Fluid Mechanics*, 72(2):331–340, **1975**.

- [53] Brian Edward Launder, G Jr Reece, and W Rodi. Progress in the development of a reynolds-stress turbulence closure. *Journal of fluid mechanics*, 68(3):537–566, **1975**.
- [54] Y Sato and K Sekoguchi. Liquid velocity distribution in two-phase bubble flow. *International Journal of Multiphase Flow*, 2(1):79–95, **1975**.
- [55] Y. Sato, M. Sadatomi, and K. Sekoguchi. Momentum and heat transfer in two-phase bubble flow—i. theory. *International Journal of Multiphase Flow*, 7(2):167–177, **1981**. ISSN 0301-9322. doi:[https://doi.org/10.1016/0301-9322\(81\)90003-3](https://doi.org/10.1016/0301-9322(81)90003-3).
- [56] Itaru Michiyoshi and Akimi Serizawa. Turbulence in two-phase bubbly flow. *Nuclear Engineering and design*, 95:253–267, **1986**.
- [57] Isao Kataoka, Akimi Serizawa, and D.C. Besnard. Prediction of turbulence suppression and turbulence modeling in bubbly two-phase flow. *Nuclear Engineering and Design*, 141(1):145–158, **1993**. ISSN 0029-5493. doi:[https://doi.org/10.1016/0029-5493\(93\)90099-U](https://doi.org/10.1016/0029-5493(93)90099-U).
- [58] I Kataoka. Modeling and prediction of turbulence in bubbly two-phase flow. In *2nd International Conference on Multiphase Flow'95, Kyoto, Japan, vol 2, April 3-7, 1995*, volume 2. **1995**.
- [59] SE Elghobashi and TW Abou-Arab. A two-equation turbulence model for two-phase flows. *The Physics of Fluids*, 26(4):931–938, **1983**.
- [60] I Kataoka and A Serizawa. Basic equations of turbulence in gas-liquid two-phase flow. *International Journal of Multiphase Flow*, 15(5):843–855, **1989**.
- [61] M. Lopez de Bertodano, Jr. Lahey, R. T., and O. C. Jones. Development of a k- Model for Bubbly Two-Phase Flow. *Journal of Fluids Engineering*, 116(1):128–134, **1994**. ISSN 0098-2202. doi:10.1115/1.2910220.

- [62] A.A. Troshko and Y.A. Hassan. A two-equation turbulence model of turbulent bubbly flows. *International Journal of Multiphase Flow*, 27(11):1965–2000, **2001**. ISSN 0301-9322. doi:[https://doi.org/10.1016/S0301-9322\(01\)00043-X](https://doi.org/10.1016/S0301-9322(01)00043-X).
- [63] MS Politano, PM Carrica, and J Converti. A model for turbulent polydisperse two-phase flow in vertical channels. *International Journal of Multiphase Flow*, 29(7):1153–1182, **2003**.
- [64] SL Lee, RT Lahey, and OC Jones. The prediction of two-phase turbulence and phase distribution phenomena using a k - κ model. , 3(4):335–368, **1989**.
- [65] R Kumar. An algebraic stress/flux model for two-phase turbulent flow. **1995**.
- [66] M. Lopez de Bertodano, S.-J. Lee, Jr. Lahey, R. T., and D. A. Drew. The Prediction of Two-Phase Turbulence and Phase Distribution Phenomena Using a Reynolds Stress Model. *Journal of Fluids Engineering*, 112(1):107–113, **1990**. ISSN 0098-2202. doi:10.1115/1.2909357.
- [67] Salih Sarı, Şule Ergün, Muhammet Barık, Cemil Kocar, and Cemal Niyazi Sökmen. Modeling of isothermal bubbly flow with interfacial area transport equation and bubble number density approach. *Annals of Nuclear Energy*, 36(2):222–232, **2009**.
- [68] Akimi Serizawa, Isao Kataoka, and Itaru Michiyoshi. Turbulence structure of air-water bubbly flow—ii. local properties. *International Journal of Multiphase Flow*, 2(3):235–246, **1975**.
- [69] T.J. Liu and S.G. Bankoff. Structure of air-water bubbly flow in a vertical pipe i. liquid mean velocity and turbulence measurements. *International Journal of Heat and Mass Transfer*, 36(4):1049 – 1060, **1993**. ISSN 0017-9310. doi:[https://doi.org/10.1016/S0017-9310\(05\)80289-3](https://doi.org/10.1016/S0017-9310(05)80289-3).
- [70] Takashi Hibiki and Mamoru Ishii. Experimental study on interfacial area transport in bubbly two-phase flows. *International Journal of Heat and Mass Transfer*, 42(16):3019–3035, **1999**.

- [71] Takashi Hibiki, Mamoru Ishii, and Zheng Xiao. Axial interfacial area transport of vertical bubbly flows. *International Journal of Heat and Mass Transfer*, 44(10):1869 – 1888, **2001**. ISSN 0017-9310. doi:[https://doi.org/10.1016/S0017-9310\(00\)00232-5](https://doi.org/10.1016/S0017-9310(00)00232-5).
- [72] Shigeo Hosokawa and Akio Tomiyama. Multi-fluid simulation of turbulent bubbly pipe flows. *Chemical Engineering Science*, 64(24):5308–5318, **2009**.
- [73] ME Shawkat, CY Ching, and M Shoukri. Bubble and liquid turbulence characteristics of bubbly flow in a large diameter vertical pipe. *International Journal of Multiphase Flow*, 34(8):767–785, **2008**.
- [74] D Lucas, E Krepper, and H-M Prasser. Development of co-current air–water flow in a vertical pipe. *International Journal of Multiphase Flow*, 31(12):1304–1328, **2005**.
- [75] M. Simonnet, C. Gentric, E. Olmos, and N. Midoux. Experimental determination of the drag coefficient in a swarm of bubbles. *Chemical Engineering Science*, 62(3):858 – 866, **2007**. ISSN 0009-2509. doi:<https://doi.org/10.1016/j.ces.2006.10.012>.
- [76] Akimi Serizawa, Isao Kataoka, and Itaru Michiyoshi. Turbulence structure of air-water bubbly flow i. measuring techniques. *International Journal of Multiphase Flow*, 2(3):221 – 233, **1975**. ISSN 0301-9322. doi:[https://doi.org/10.1016/0301-9322\(75\)90011-7](https://doi.org/10.1016/0301-9322(75)90011-7).
- [77] Akimi Serizawa, Isao Kataoka, and Itaru Michiyoshi. Turbulence structure of air-water bubbly flow ii. local properties. *International Journal of Multiphase Flow*, 2(3):235 – 246, **1975**. ISSN 0301-9322. doi:[https://doi.org/10.1016/0301-9322\(75\)90012-9](https://doi.org/10.1016/0301-9322(75)90012-9).
- [78] Akimi Serizawa, Isao Kataoka, and Itaru Michiyoshi. Turbulence structure of air-water bubbly flow iii. transport properties. *International Journal of*

Multiphase Flow, 2(3):247 – 259, **1975**. ISSN 0301-9322. doi:[https://doi.org/10.1016/0301-9322\(75\)90013-0](https://doi.org/10.1016/0301-9322(75)90013-0).

- [79] T.J. Liu and S.G. Bankoff. Structure of air-water bubbly flow in a vertical pipe ii. void fraction, bubble velocity and bubble size distribution. *International Journal of Heat and Mass Transfer*, 36(4):1061 – 1072, **1993**. ISSN 0017-9310. doi:[https://doi.org/10.1016/S0017-9310\(05\)80290-X](https://doi.org/10.1016/S0017-9310(05)80290-X).
- [80] TJ Liu. The role of bubble size on liquid phase turbulent structure in two-phase bubbly flow. In *Proc. Third International Congress on Multiphase Flow ICMF*, volume 98, pages 8–12. **1998**.

CURRICULUM VITAE

Credentials

Name,Surname : İzzet Özgün Güler
Place of Birth : Ankara / TURKEY
Marital Status : Single
E-mail : iog@hacettepe.edu.tr
Address : Nuclear Engineering Department, Hacettepe University
Ankara / TURKEY

Education

B.Sc. : Nuclear Engineering, Hacettepe University, Ankara / TURKEY
M.Sc. : Nuclear Engineering, Hacettepe University, Ankara / TURKEY

Foreign Languages : English

Work Experience : Director, iog Mühendislik Ltd.
Director, iog Enerji Ltd.

Areas of Experiences : CFD
Optimization